A MULTISCALE APPROACH FOR TAILORING THE MACRO-PROPERTIES OF POLYCRYSTALLINE MATERIALS

A Dissertation

Presented to the Faculty of the Graduate School

of Cornell University

in Partial Fulfillment of the Requirements for the Degree of

Doctor of Philosophy

by

Babak Kouchmeshky

February 2010

A MULTISCALE APPROACH FOR TAILORING THE MACRO-PROPERTIES OF POLYCRYSTALLINE MATERIALS

Babak Kouchmeshky, Ph.D.

Cornell University 2010

The first half of this thesis provides a continuum approach for predicting the constitutive response of HCP polycrystals using a simple non-hardening constitutive model incorporating both slip and twinning. This has been achieved by considering a physical based methodology for restricting the amount of the twinning activity. A continuum approach is used in modeling the texture evolution that eliminates the need for increasing the number of discrete crystal orientations to account for new orientations created by twinning during deformation. The polycrystal is represented by an orientation distribution function using the Rodrigues parameterization. A total Lagrangian framework is used to model the evolution of microstructure. Numerical examples are used to show the application of the methodology for modeling deformation processes.

In the second half, the quantification and propagation of uncertainty in process conditions and initial microstructure on the final product properties in a deformation process is presented. The stochastic deformation problem is modeled using a sparse grid collocation approach that allows the utilization of a deterministic simulator to build interpolants of the main solution variables in the stochastic support space. The ability of the method in estimating the statistics of the macro-scale microstructure-sensitive properties and constructing the convex hull of these properties is shown through examples featuring randomness in initial texture and process parameters. A data-driven model reduction method-

ology together with a maximum entropy approach are used for representing randomness in initial texture in Rodrigues space. Comparisons are made with the results obtained from the Monte-Carlo method.

BIOGRAPHICAL SKETCH

The author was born in Tehran, Iran. He obtained his Bachelor and Master's degree in Civil Engineering from University of Tehran in 2000 and 2002 respectively. In August, 2004, the author entered the doctoral program at Cornell University, College of Engineering.

This document is dedicated to my parents Lili Hazari and Alireza Kouchmeshky and my sister Azita for their constant support and inspiration throughout my life. It is also dedicated to Aileen; my true love for her patience and constant encouragement.

ACKNOWLEDGEMENTS

I would like to thank Professor Nicholas Zabaras for serving as the chair of my special committee. I would also like to thank Professors Subrata Mukherjee and Derek Warner for serving on my special committee.

I would like to thank Cornell University for supporting me through teaching assistantship.

TABLE OF CONTENTS

LIST OF TABLES

LIST OF FIGURES

CHAPTER 1

MODELING THE RESPONSE OF HCP POLYCRYSTALS DEFORMING BY SLIP AND TWINNING USING A FINITE ELEMENT REPRESENTATION OF THE ORIENTATION SPACE

1.1 Introduction

There have been significant developments in the field of crystal plasticity modeling and evolution of microstructure. For deformation of FCC and BCC metals which deform predominantly by crystallographic slip there is already a well developed mathematical theory [1, 2, 3, 4, 5]. Plastic deformation of hexagonal closed packed crystalline (HCP) materials due to slip and twinning is less developed. HCP materials are characterized by highly anisotropic mechanical behavior. Twinning and slip have shown to be important deformation modes for these materials at low temperature. Hence, realistic modeling of HCP crystalline materials requires modeling of the deformation twinning in the constitutive equations.

The closed packed directions for crystallographic slip on HCP materials are $< 11\bar{2}0 >$ family of directions. Since these are perpendicular to the c-axis of the HCP crystals they lack the ability to cause deformation along that axis. Twinning is considered to be the mechanism that provides the inelastic deformation along the c-axis.

The problem of incorporating the twinning mechanism into crystal plasticity has been addressed in [6, 7, 8, 9, 10]. In these works, twinning is treated as pseudo-slip and it is assumed that there exists a critical resolved shear stress for

twinning systems. Since twinning consists of a sudden change in crystal orientation, texture evolution due to twinning is different from that of slip. Various models have been used to model texture evolution due to twinning. One of the major difficulties in addressing the texturing due to twinning has been to account for the new crystal orientation generated by the twinning. In [7, 11] a probabilistic approach is used to avoid the difficulties associated with increasing number of discrete crystal orientations. In these models, the orientations of grains are updated only if the twinned volume fraction has reached a certain value.

Theoretical investigations of texture development are typically based on discrete aggregate models. In these models, the polycrystal response is modeled through a representative volume of material with discrete aggregates. An alternative method for texture evolution is to use a continuous representation of orientation through the orientation distribution function (ODF) [6]. In this method, the distribution of crystal orientations is modeled over a three-dimensional orientation space. Finite element schemes for the ODF were proposed in [4, 5, 6, 42, 13]. These are based on a finite element representation of the ODF using piecewise polynomial interpolating functions. This approach avoids using discrete orientations and problems associated with increasing the number of elements to account for new orientations created by twinning during the process. However, it lacks the ability to capture grain boundary accommodation and interaction between grains.

Further, in contrast to existing works, based almost entirely on Euler angle spaces, the analysis of HCP polycrystals that follows is based on Rodrigues' space. Using this representation one can use the crystal symmetries to reduce

the space to a geometrically simple region [6]. This will allow the texture evolution equations to be solved over a reduced region of the space called fundamental region. Moreover, due to symmetry of the space, textures have a particularly simple structure over Rodrigues' space. On this representation, a conservation equation for the ODF evolution for material deforming by combinations of multiple slip and twinning is introduced similar to [6] which takes into account sudden jumps in orientations as a consequence of twinning.

The orientation distribution function is updated in Rodrigues space by solving this conservation type equation using the finite element method. In addition to modelling texture evolution, this also provides the means to predict the response of HCP polycrystals. In [6], a constitutive model was employed for HCP polycrystals but no effort was made in modeling the material stress-strain response.

In this chapter, a rate-independent constitutive model is used for predicting the response of HCP polycrystals due to slip and twinning. Grain boundary effects are incorporated in the simulation using the approach suggested in [7]. A new probabilistic criterion for arresting twinning is proposed which is capable of predicting different strain hardening stages reported in the literature. A total Lagrangian approach is used to model the texture evolution. The continuum representation of texture, used in this chapter, enables one to model the texture evolution independent of the choice of an aggregate and to avoid the difficulties associated with increasing the number of discrete crystal orientations due to twinning. The model is validated for tension, shear and compression modes.

The plan for this chapter is as follows. In Section 2, the mathematical model for twinning is discussed and it is shown that twinning can be considered as a

pseudo-slip. In Section 3, a continuum description of polycrystals is represented along the necessary equations for texture evolution. In Section 4 the constitutive model for polycrystalls undergoing slip and twinning is represented. Section 5 discusses the reorientation of crystals. Section 6 presents some numerical applications of the methodology. Section 7 contains the discussion.

1.2 Twinning model

In modeling the twin as a pseudo-slip, the approach in [6] is adopted here. Consider a single crystal consisting of untwinned and twinned parts with volume fraction of the twinned part equal to λ. Let $\boldsymbol{n}^{tw}$ be a unit normal vector to the twinning plane and $\boldsymbol{b}^{tw}$ be the twinning plane direction (Fig. 1.1). Let $\boldsymbol{x}$ be the original position of a lattice point and $\boldsymbol{x}'$ be its twinned position. The displacement under twinning is proportional to $\boldsymbol{x} \cdot \boldsymbol{n}^{tw}$ [6]:

$$\begin{aligned} \boldsymbol{x}' &= \boldsymbol{x} + \gamma_0 \boldsymbol{b}^{tw}(\boldsymbol{x} \cdot \boldsymbol{n}^{tw}) \\ &= (I + \gamma_0(\boldsymbol{b}^{tw} \otimes \boldsymbol{n}^{tw}))\boldsymbol{x} = \boldsymbol{F}^{tw}\boldsymbol{x} \end{aligned} \tag{1.1}$$

where γ_0 is a constant of proportionality and $\boldsymbol{F}^{tw}$ is the deformation gradient for the twinned part. The deformation gradient for the untwinned part is the identity tensor ($\boldsymbol{F}^{ntw} = \boldsymbol{I}$). The average deformation gradient for the grain is calculated as follows:

$$\boldsymbol{F} = \lambda \boldsymbol{F}^{tw} + (1 - \lambda)\boldsymbol{F}^{ntw} = \boldsymbol{I} + \lambda \gamma_0 \boldsymbol{b}^{tw} \otimes \boldsymbol{n}^{tw} \tag{1.2}$$

Since in this model twinning occurs continuously, $\dot{\lambda}$ exists and is finite.

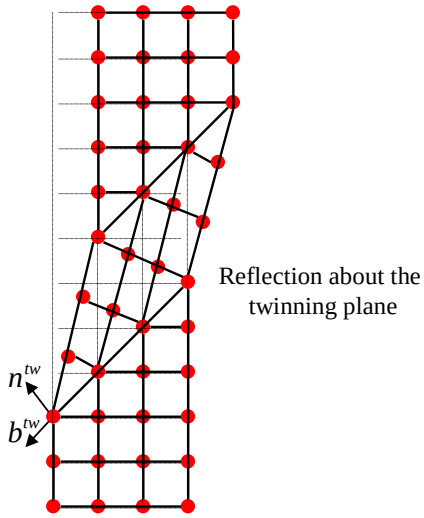

Figure 1.1: The lattice in the twinned region has a special orientation in relation to the untwinned crystal, defined by a reflection across the twinning plane.

Hence, the average macroscopic velocity gradient for the entire grain can be written as [6]:

$$\boldsymbol{L} = \dot{\boldsymbol{F}}\boldsymbol{F}^{-1} = \dot{\lambda}\gamma_0 \boldsymbol{b}^{tw} \otimes \boldsymbol{n}^{tw} = \dot{\gamma}\boldsymbol{S}^{tw} \tag{1.3}$$

From this we see that twinning on a single twin system could be considered as a pseudo-slip with the shear rate $\dot{\gamma}$ and Schmid tensor $\boldsymbol{S}^{tw} = \boldsymbol{b}^{tw} \otimes \boldsymbol{n}^{tw}$.

1.3 Overview of representation of HCP polycrystals

To set forward the necessary background for later developments, a very brief description of microstructure associated with polycrystalline plasticity is pro-

vided. Consider a macroscopic material point and let it be associated with the underlying microstructure $\mathcal{M}$. Using the Taylor hypothesis, response of any crystal of the polycrystal is determined only by its orientation and does not depend on attributes of neighboring crystals. The rotation $\boldsymbol{R}$ relates the crystal lattice frame, $\hat{\boldsymbol{e}}_i$, to a sample reference frame $\boldsymbol{e}_i$ as $\boldsymbol{e}_i = \boldsymbol{R}\,\hat{\boldsymbol{e}}_i$. The orientation $\boldsymbol{R}$ is not unique because of crystal symmetries. This non-uniqueness has traditionally been resolved by restricting the choice of orientation to a fundamental region.

The ODF (orientation distribution function), represented as $\mathcal{A}(\boldsymbol{r})$, is used to represent the crystal density over the fundamental region. In this chapter, the representation of the ODF given by $\mathcal{A}(\boldsymbol{r}, t)$ is Eulerian and $\hat{\mathcal{A}}(\boldsymbol{s}, t)$ is Lagrangian ($\mathcal{A}(\boldsymbol{r}, t) = \mathcal{A}(\hat{\boldsymbol{r}}(s, t), t)$
$= \hat{\mathcal{A}}(\boldsymbol{s}, t)$). When texture development is modeled, a reorientation vector $\hat{\boldsymbol{r}}(s, t)$ is computed that maps the location $\boldsymbol{r}$ in the reoriented region (at time t) to the corresponding location s in the reference fundamental region (at time t = 0).

The evolution of ODF can be considered by the conservation equation which in the Lagrangian framework has the following format [14]

$$\int_{\Omega} \left(\hat{\mathcal{A}}(\boldsymbol{s}, t)\; J(\boldsymbol{s}, t) \;-\; \hat{\mathcal{A}}(\boldsymbol{s}, 0) \right) d\Omega \;=\; 0 \tag{1.4}$$

where $J(\boldsymbol{s}, t)$ is the Jacobian determinant of the re-orientation of the crystals and $\hat{\mathcal{A}}(\boldsymbol{s}, 0) \;=\; \mathcal{A}_0(\boldsymbol{s})$ is the ODF associated with the reference map and can be thought of as the initial texturing of the material. The Lagrangian version of the conservation equation is then defined as:

$$\hat{\mathcal{A}}(\boldsymbol{s}, t)\; J(\boldsymbol{s}, t) \;=\; \hat{\mathcal{A}}(\boldsymbol{s}, 0) \;=\; \mathcal{A}_0(\boldsymbol{s}) \tag{1.5}$$

The conventional Eulerian rate form of the conservation equation is obtained by considering the rate of Eq. (1.5) as

$$\begin{aligned} \frac{\partial \mathcal{A}(\boldsymbol{r},t)}{\partial t} &+ \bigtriangledown \mathcal{A}(\boldsymbol{r},t) \cdot \boldsymbol{v}(\boldsymbol{r},t) \\ &+ \mathcal{A}(\boldsymbol{r},t) \bigtriangledown \cdot \boldsymbol{v}(\boldsymbol{r},t) \; = \; 0 \end{aligned} \tag{1.6}$$

where $\boldsymbol{v}(\boldsymbol{r},t)$ is the Eulerian re-orientation velocity. Such an Eulerian representation of the ODF is useful in cases where elastic effects are negligible. In a Lagrangian framework, the reorientation $\hat{\boldsymbol{r}}$ has to be calculated from the reorientation velocity using the following relation:

$$\frac{d\hat{\boldsymbol{r}}}{dt} = \hat{\boldsymbol{v}}(\boldsymbol{r},t) \tag{1.7}$$

The Jacobian determinant of the reorientation of the crystals can then be calculated as $J(\boldsymbol{r},t) = det(\nabla(\hat{\boldsymbol{r}}))$.

1.3.1 Representing twinning in the orientation space

Twinning can be modeled as the reflection of the orientation in the twinning plane. Let **n** be the unit vector normal to the twinning plane. The mapping of the crystal through twinning can be represented as [15]:

$$\mathbf{x}' = \mathbf{x} - 2\mathbf{n}(\mathbf{n}.\mathbf{x}) = (\mathbf{I} - 2\mathbf{n} \otimes \mathbf{n})\mathbf{x} = T_1\mathbf{x} \tag{1.8}$$

where $T_1 = \mathbf{I} - 2\mathbf{n} \otimes \mathbf{n}$ and **I** is the identity matrix. Since this mapping represents a reflection, one would end up with $\mathbf{det}T_1 = -1$. To represent this mapping with rotation, we need to have $\mathbf{det}T = +1$. We can achieve this through another reflection $\mathbf{det}T_2 = -1$ that maps the lattice to itself. The resultant map would be $T = T_2T_1$. Since all the crystallographic lattices are symmetric with respect to

reflection around the origin, one can choose $T_2 = -I$. For the 3D case, $\mathbf{det}T_2 = -1$ and one will end up with [15]

$$\begin{aligned}\mathbf{Tx} &= (-\mathbf{I})(-\mathbf{I} + 2\mathbf{n} \otimes \mathbf{n})\mathbf{x} \\ &= (\mathbf{I} - 2\mathbf{n} \otimes \mathbf{n})\mathbf{x} = T_1\mathbf{x}\end{aligned} \tag{1.9}$$

The resultant operator T can be seen as rotation of crystal axis about the twin plane normal through an angle of π. Under the quaternion parametrization of rotation space, this rotation can be represented by a quaternion:

$$T^q = \pm[0, \mathbf{n}] \tag{1.10}$$

The steps required for calculating the lattice reorientation in the fundamental region due to twinning is summarized as follows:

1. Convert parametrization of crystal lattice orientation in Rodrigues space ($\mathbf{h}$) to the quaternion representation ($\mathbf{h}^q$).
2. Perform the quaternion product $\mathbf{q} = T^q\mathbf{h}^q$
3. Project $\mathbf{q}$ to an equivalent rotation $\mathbf{q}^F$ in the fundamental region based on crystal symmetries.
4. Convert $\mathbf{q}^F$ to the Rodrigues parametrization, $\mathbf{h}^{new}$.

1.3.2 Conservation of the ODF considering slip and twinning

Twinning of the crystal lattice on a particular twin system uniquely maps the orientation to another location in the fundamental region. Thus, twinning results in loss of volume fraction of a particular orientation and accumulation of

the orientation at another location in the orientation space. These can be regarded as source and sink terms in the conservation equation (Eq. 1.4). Since the material volume must be conserved, material leaving from a source must show up at a sink.

At an orientation $A(\boldsymbol{r}, t)$, the source (ϕ) at an instant t contains two terms arising from the loss of volume fraction of that orientation due to twinning and the gain of orientation from its twin images at positions $\boldsymbol{r}^k$ in the orientation space. This is shown schematically in Fig. 1.2. Thus $\phi(A, \boldsymbol{r}, t)$ is given as [6],

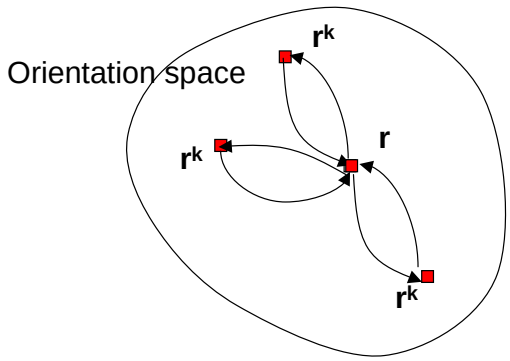

Figure 1.2: Images of **r** in the orientation space with respect to twin system k. The orientation **r** acts as a source to the images $\mathbf{r}^k$ while it gains volume fraction when it acts as a sink to the volume fraction lost by $\mathbf{r}^k$.

Here, α_{tw} is the set of images of the current crystal orientation with respect to the twin planes of the twin systems and $\dot{\lambda}^k$ refers to the rate of change in volume fraction of the orientation at time t due to twinning in the twin system

given by k. Thus, the presence of the conservation term modifies the evolution of the ODF in the form,

$$\begin{aligned} \int_{\Omega} J(\boldsymbol{s},t)(\hat{A}(\boldsymbol{s},t) &- \Phi(\boldsymbol{s},t))d\Omega \\ &= \int_{\Omega} \hat{A}(\boldsymbol{s},0)d\Omega \end{aligned} \tag{1.12}$$

where Ω is the reference fundamental region and

$$\Phi(\boldsymbol{s},t) = \int_0^t \phi(\boldsymbol{s},t)dt \tag{1.13}$$

The total volume fraction of twinned crystals can be calculated by only considering the untwinned portion ($\tilde{A}$) of the ODF as,

$$\begin{aligned} \int_{\Omega} J(\boldsymbol{s},t)(\tilde{A}(\boldsymbol{s},t) &- \tilde{\Phi}(\boldsymbol{s},t))d\Omega \\ &= \int_{\Omega} \hat{A}(\boldsymbol{s},0)d\Omega \end{aligned} \tag{1.14}$$

Here, the source term due to the presence of twinning ($\tilde{\Phi}$) is given as [6],

$$\tilde{\Phi}(\boldsymbol{s},t) = \int_0^t \tilde{\phi}(\boldsymbol{s},t)dt \tag{1.15}$$

and

$$\tilde{\phi}(\boldsymbol{s},t) = -\tilde{A}(\boldsymbol{s},t) \sum_{k \in \alpha_{tw}} \dot{\lambda}^k(\boldsymbol{s}) \tag{1.16}$$

Only the volume fraction that is lost from each orientation is calculated. The other term in $\phi(\mathbf{s},t)$ that corresponds to the orientations coming from the other twin images is not used. Since we concentrate only on the volume fraction of crystals that is lost due to twinning, the equation for ($\tilde{A}$) no longer follows ODF conservation. The volume fraction of twins is given by $\tilde{A}(\boldsymbol{s},t)$ as,

$$f = 1 - \int_{\Omega} \tilde{A}(\boldsymbol{s},t)d\Omega \tag{1.17}$$

The ODF, in the present work, is approximated with finite element polynomial functions defined over an explicit discretization of the orientation space based on Rodrigues parametrization. The parametrization of $\boldsymbol{R}$ is derived from the natural invariants of $\boldsymbol{R}$: the axis of rotation $\boldsymbol{n}$ and the angle of rotation ζ. The angle-axis parametrization ($\boldsymbol{r}$) is obtained by scaling the axis $\boldsymbol{n}$ by a function of the angle ζ as $\boldsymbol{r} = \boldsymbol{n} \tan\left(\frac{\zeta}{2}\right)$. The orientation $\boldsymbol{R}$ is related to the parametrization $\boldsymbol{r}$ as

$$\begin{aligned} \boldsymbol{R} &= \frac{1-\boldsymbol{r}\boldsymbol{\cdot}\boldsymbol{r}}{1+\boldsymbol{r}\boldsymbol{\cdot}\boldsymbol{r}}\left(\boldsymbol{I}\right) \\ &+ \frac{2}{1+\boldsymbol{r}\boldsymbol{\cdot}\boldsymbol{r}}(\boldsymbol{r}\otimes\boldsymbol{r}+\boldsymbol{I}\times\boldsymbol{r}) \end{aligned} \tag{1.18}$$

The polycrystal average of an orientation dependent property, $\boldsymbol{\Upsilon}(\boldsymbol{r},t)$, is determined as follows

$$\begin{aligned} \langle\boldsymbol{\Upsilon}\rangle &= \int_{\Omega_t} \boldsymbol{\Upsilon}(\boldsymbol{r},t)\,\mathcal{A}(\boldsymbol{r},t)\,d\Omega_t \\ &= \int_{\Omega} \boldsymbol{\Upsilon}(\hat{\boldsymbol{r}}(\boldsymbol{s},t),t)\,(\mathcal{A}_0(\boldsymbol{s}) \\ &+ \Phi(\boldsymbol{s},t)J(\boldsymbol{s},t))d\Omega \end{aligned} \tag{1.19}$$

where $d\Omega_t$ is defined as the volume element on the current fundamental region. One can conclude that if the re-orientation and initial texture are known the average property for the polycrystal can be calculated. Hence, there is no need to compute the current ODF, $\mathcal{A}(\boldsymbol{r},t)$.

1.4 Constitutive sub-problem for HCP crystals deforming through slip and twinning

During deformation process of a HCP polycrystal, the deformation is manifested in the crystal in the form of crystallographic slip, twinning and lattice re-orientation of crystals. Re-orientation of the crystals occurs in an ordered manner such that a preferential orientation or texture develops. Consider a point on the reference fundamental region corresponding to a particular crystal orientation. In an appropriate kinematic framework for large deformation inelastic analysis, the total deformation gradient is decomposed into plastic and elastic parts as follows (Fig. 1.3)

$$\boldsymbol{F}_{n+1} = \boldsymbol{F}^e \, \boldsymbol{F}^p \tag{1.20}$$

where $\boldsymbol{F}^e$ is the elastic deformation gradient and $\boldsymbol{F}^p$, the plastic deformation gradient, with $\det\boldsymbol{F}^p = 1$. This decomposition of the deformation gradient results in the following

$$\boldsymbol{F}^e = \boldsymbol{F}_{n+1} \, (\boldsymbol{F}^p)^{-1} \tag{1.21}$$

In the following scheme, all vector and tensorial quantities are expressed in the reference sample frame, i.e., the initial (macro-scale) configuration. Furthermore, crystal specific properties like the stiffness and compliance have to be transformed to the sample reference frame using the crystal orientation $\boldsymbol{r}$. At time $t = t_{n+1}$, the following steps are followed to update the texture and obtain the necessary quantities at a material point in the sample. The data that is known at time $t = t_{n+1}$ includes $\{\boldsymbol{F}_n, \boldsymbol{F}_{n+1}\}$, the deformation gradients at time $t = t_n$ and t_{n+1}, the Cauchy stress $\boldsymbol{T}_n$ and the ODF $A(\boldsymbol{r}, t_n)$ at time t_n. The task

of the constitutive sub-problem is to identify the elastic-plastic decomposition of the deformation gradient and the Cauchy stress at time t_{n+1}. Further, this information is used to calculate reorientation of the crystals which is in turn used to update the ODF.

In the constitutive equations to be defined below, the Green elastic strain measure is defined on the relaxed configuration (plastically deformed, unstressed configuration) $\bar{\mathcal{B}}$. It is represented as $\bar{\boldsymbol{E}}^e = \frac{1}{2}\left(\boldsymbol{F}^{eT}\boldsymbol{F}^e - \boldsymbol{I}\right)$. The conjugate stress measure is then defined as $\bar{\boldsymbol{T}} = \det\boldsymbol{F}^e(\boldsymbol{F}^e)^{-1}\boldsymbol{T}(\boldsymbol{F}^e)^{-T}$ where $\boldsymbol{T}$ is the Cauchy stress for the crystal in the sample reference frame. In the following analysis, crystal specific properties like the stiffness and compliance are transformed to the sample reference frame for each crystal using the position $\boldsymbol{r}$ in the orientation space. The trial elastic strain ($\bar{\boldsymbol{E}}^e_{trial}$) is first calculated as:

$$\begin{aligned} \boldsymbol{F}^e_{trial} &= \boldsymbol{F}(\boldsymbol{F}^p_n)^{-1} \\ \bar{\boldsymbol{E}}^e_{trial} &= \frac{1}{2}((\boldsymbol{F}^e_{trial})^T\boldsymbol{F}^e_{trial} - \boldsymbol{I}) \end{aligned} \tag{1.22}$$

This is followed by a calculation of a trial stress $\bar{\boldsymbol{T}}_{trial}$ and trial resolved shear stress $\boldsymbol{\tau}^\alpha_{trial}$ on each slip and twin system:

$$\begin{aligned} \bar{\boldsymbol{T}}_{trial} &= \boldsymbol{L}^e[\bar{\boldsymbol{E}}^e_{trial}] \\ \boldsymbol{\tau}^\alpha_{trial} &= \bar{\boldsymbol{T}}_{trial}\cdot\boldsymbol{S_0}^\alpha \end{aligned} \tag{1.23}$$

Here $\boldsymbol{S}^\alpha_0 = \boldsymbol{m}^\alpha \otimes \boldsymbol{n}^\alpha$ is the Schmid tensor and $\dot{\gamma}^\alpha$ is the plastic shearing rate on the α^{th} slip or twin system. $\boldsymbol{m}^\alpha$ and $\boldsymbol{n}^\alpha$ are the slip or twin direction and plane

normal, respectively. There is a critical resolved shear stress above which slip and twin systems are activated. Such a set $\mathcal{PA}$ of potentially active slip and twin systems are identified initially based on the trial resolved stress as the systems with $|\boldsymbol{\tau}^{\alpha}_{trial}| - s^{\alpha}(t) > 0$.

The evolution of plastic deformation gradient can be written as

$$\dot{\boldsymbol{F}}^{p} = \boldsymbol{L}^{p}\boldsymbol{F}^{p} \tag{1.24}$$

The flow rule should be modified to take into account the grain boundary accommodation effect. In [7], the use of an extra isotropic term is suggested for this purpose. The shearing rates on the slip and twin systems, $\dot{\gamma}^{\alpha}$ is found using the following flow rule,

$$\boldsymbol{L}^{p} = (1-\xi)\sum_{\alpha}\dot{\gamma}^{\alpha} sign(\tau^{\alpha})\boldsymbol{S}^{\alpha}_{0} + \xi\boldsymbol{M} \tag{1.25}$$

$$\boldsymbol{M} = \dot{\varepsilon}_{0}(\frac{\bar{\sigma} - s_{th}}{s})^{\frac{1}{m}}(\frac{3\boldsymbol{T}^{'}}{2\bar{\sigma}}) \tag{1.26}$$

$$\bar{\sigma} = \sqrt{\frac{3}{2}\boldsymbol{T}^{'}\cdot\boldsymbol{T}^{'}} \tag{1.27}$$

where $\dot{\varepsilon}_{0}$ is a constant, ξ is nonzero only if $\bar{\sigma} > s_{th}$ and s is an internal variable with a threshold value s_{th}. As suggested in [7], the localized non-crystallographic effects around grain boundaries can be approximated by a grain boundary layer with a very small volume fraction ($\xi \ll 1$). The layer is assumed to follow a simple isotropic flow rule. Hence, the isotropic term is added to the flow rule to account for grain boundary effects. Since the assumption of fully bounded grains leads to unrealistically high stress this term helps in bounding the stress level.

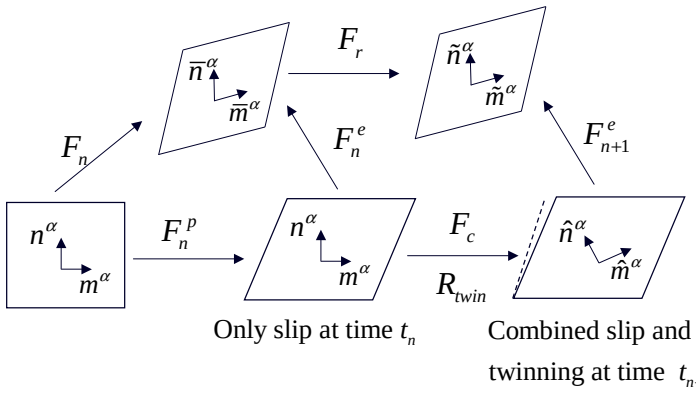

Figure 1.3: Evolution of various material configurations for a single crystal as needed in the integration of the constitutive model. Here $\boldsymbol{m}^\alpha$ denotes the slip direction and $\boldsymbol{n}^\alpha$ denotes the slip normal, which together define the slip systems. $\boldsymbol{F}_r$ is the relative deformation gradient. The mechanism at time t_n is slip alone. At time t_{n+1}, twin systems are activated which causes additional lattice reorientation (R_{twin}) and a pseudo-slip.

Using an Euler-backward time integration procedure, one can write,

$$\boldsymbol{F}_{n+1}^p = (\boldsymbol{I} + \Delta t \boldsymbol{L}^p)\boldsymbol{F}_n^p \tag{1.28}$$

Substituting Eq. (1.28) in Eq. (1.21) results in

$$\begin{aligned} \boldsymbol{F}_{n+1}^p \quad &= \quad \boldsymbol{F}_{trial}^e(\boldsymbol{I} - (1-\xi)\Delta t \times \\ &\sum_\alpha \quad \dot{\gamma}^\alpha sign(\tau^\alpha)\boldsymbol{S}_0^\alpha - \xi \boldsymbol{M}\Delta t) \end{aligned} \tag{1.29}$$

During plastic flow the active systems are assumed to follow the consistency condition: $|\boldsymbol{\tau}^\alpha| = s^\alpha$ and a simple non hardening assumption is used for the slip and twin resistances ($\dot{s}(i) = 0$). The bar stress (the conjugate to the green elastic strain;the second Piola-Kirchhoff stress) is then given by,

$$\begin{aligned} \bar{\boldsymbol{T}} \quad &= \bar{\boldsymbol{T}}_{trial} - (1-\xi)\frac{\Delta t}{2}\sum_\beta sign(\boldsymbol{\tau}_{trial}^\beta)\dot{\gamma}^\beta \boldsymbol{L}^e[\boldsymbol{B}^\beta] \\ - \quad &\xi\frac{\Delta t}{2}\boldsymbol{L}^e({\boldsymbol{F}_{trial}^e}^T\boldsymbol{F}_{trial}^e\boldsymbol{M} + (\boldsymbol{M})^T{\boldsymbol{F}_{trial}^e}^T\boldsymbol{F}_{trial}^e) \end{aligned} \tag{1.30}$$

The updated shearing rates $\dot{\gamma}^\beta$ are obtained by solving the following equation:

$$\begin{aligned} | \quad & \boldsymbol{\tau}^\alpha| = |\boldsymbol{\tau}^\alpha_{trial}| - (1-\xi)\frac{\Delta t}{2} \times \\ \sum_\beta \quad & sign(\boldsymbol{\tau}^\alpha_{trial}) sign(\boldsymbol{\tau}^\beta_{trial}) \dot{\gamma}^\beta \boldsymbol{L}^e[\boldsymbol{B}^\beta] \cdot \boldsymbol{S}^\alpha_0 \\ - \quad & \xi \frac{\Delta t}{2} sign(\boldsymbol{\tau}^\alpha_{trial}) \boldsymbol{L}^e ({\boldsymbol{F}^e_{trial}}^T \boldsymbol{F}^e_{trial} \boldsymbol{M} \\ + \quad & (\boldsymbol{M})^T {\boldsymbol{F}^e_{trial}}^T \boldsymbol{F}^e_{trial}) \cdot \boldsymbol{S}^\alpha_0 \end{aligned} \tag{1.31}$$

where, $\alpha \in \mathcal{PA}$ and,

$$\boldsymbol{B}^\beta = [(\boldsymbol{S}^\beta_0)^T (\boldsymbol{F}^e_{trial})^T \boldsymbol{F}^e_{trial} + (\boldsymbol{F}^e_{trial})^T \boldsymbol{F}^e_{trial} \boldsymbol{S}^\beta_0] \tag{1.32}$$

The system of equations for $x^\beta = \dot{\gamma}^\beta \geq 0$ takes the form:

$$\sum_{\beta \in \mathcal{PA}} A^{\alpha\beta} x^\beta = b^\alpha \tag{1.33}$$

where,

$$A^{\alpha\beta} = \frac{\Delta t}{2} sign(\boldsymbol{\tau}^\alpha_{trial}) sign(\boldsymbol{\tau}^\beta_{trial}) \boldsymbol{L}^e[\boldsymbol{B}^\beta] \cdot \boldsymbol{S}^\alpha_0 \tag{1.34}$$

$$\begin{aligned} b^\alpha \quad &= \quad |\boldsymbol{\tau}^\alpha_{trial}| - s^\alpha - \xi \frac{\Delta t}{2} sign(\boldsymbol{\tau}^\alpha_{trial}) \\ &\times \quad \boldsymbol{L}^e ({\boldsymbol{F}^e_{trial}}^T \boldsymbol{F}^e_{trial} \boldsymbol{M} \\ &+ \quad (\boldsymbol{M})^T {\boldsymbol{F}^e_{trial}}^T \boldsymbol{F}^e_{trial}) \cdot \boldsymbol{S}^\alpha_0 \end{aligned} \tag{1.35}$$

If for any slip system $\dot{\gamma}^\beta \leq 0$, then this slip system is removed from the set of potentially active systems. The system of Eqs. (1.33) is solved until for all slip systems $\dot{\gamma}^\beta > 0$.

The plastic part of the deformation gradient and the Cauchy stress are computed as follows,

$$\begin{aligned} \boldsymbol{F}^p &= (\boldsymbol{I} + \Delta t \boldsymbol{L}^p)\boldsymbol{F}^p_n \\ \boldsymbol{T} &= F^e[det(\boldsymbol{F}^e)]^{-1}\bar{\boldsymbol{T}}(F^e)^T \end{aligned} \tag{1.36}$$

The change in the volume fraction of twin systems used in Eq. (1.3) for updating the average macroscopic velocity gradient is then given as,

$$\dot{\lambda}^\alpha(t) = \frac{\dot{\gamma}^\alpha}{\gamma_0} \tag{1.37}$$

1.5 Reorientation of crystals

The reorientation velocity is given as follows:

$$\boldsymbol{v} \;=\; \frac{\partial \boldsymbol{r}}{\partial t} \;=\; \frac{1}{2}\left(\boldsymbol{\varpi} \;+\; (\boldsymbol{\varpi}\cdot\boldsymbol{r})\boldsymbol{r} \;+\; \boldsymbol{\varpi}\times\boldsymbol{r}\right) \tag{1.38}$$

where $\boldsymbol{r}$ is the orientation (Rodrigues' parametrization) and $\boldsymbol{\varpi}$ represents the spin vector defined as $\boldsymbol{\varpi} \;=\; \text{vect}\left(\dot{\boldsymbol{R}}^e\boldsymbol{R}^{eT}\right) \;=\; \text{vect}\left(\boldsymbol{\Omega}\right)$ where $\boldsymbol{R^e}$ is evaluated through the polar decomposition of the elastic deformation gradient $\boldsymbol{F}^e$ as $\boldsymbol{F}^e \;=\; \boldsymbol{R}^e\boldsymbol{U}^e$. Considering the Euler-backward time integration of $\dot{\boldsymbol{R}}^e\boldsymbol{R}^{eT} \;=\; \boldsymbol{\Omega}$, where $\boldsymbol{\Omega}$ is the spin tensor, leads to the following:

$$\boldsymbol{R}^e_{n+1} \;=\; \exp(\Delta t\boldsymbol{\Omega}_{n+1})\boldsymbol{R}^e_n \tag{1.39}$$

and

$$\boldsymbol{\Omega}_{n+1} \;=\; \frac{1}{\Delta t}\ln\left\{\boldsymbol{R}^e_{n+1}\boldsymbol{R}^{eT}_{\;n}\right\} \tag{1.40}$$

From the elastic deformation gradients, $\boldsymbol{R}^e_{n+1}$ and $\boldsymbol{R}^e_n$ are evaluated and one can evaluate the spin tensor $\boldsymbol{\Omega}_{n+1}$ using Eq. (1.40) and then the re-orientation velocity from Eq. (2.2). Further, post-processing involves computing the average Cauchy stress from

$$\langle \boldsymbol{T} \rangle \;=\; \int_{\Omega_t} \boldsymbol{T}(\boldsymbol{r},t)\; \mathcal{A}(\boldsymbol{r},t) d\Omega_t \tag{1.41}$$

1.5.1 Arresting of twin systems

Experimental results show that the volume fraction of twins for HCP materials saturates at a level significantly smaller than unity [16]. This shows that after twinning starts some restriction must be imposed on propagation of twins.

A number of different mechanisms have been proposed to determine where the deformation twinning activity should stop [6, 16]. In [6], it is assumed that twins are not likely to form if they are going to intersect existing twins. A random function was used to relate the probability of intersection of twins to their volume fraction. Then this random function is used to stop the twinning activity. The random function was constructed from geometric arguments in which a hypothetical grain is considered as an average of real grains.

As suggested in [17], only a small portion of grains show cross twinning in comparison to the total number of twins. Hence, for arresting the twin systems the following method is used. For almost all twin systems, the twinning is stopped after the saturation volume fraction is reached. However, based on a probabilistic criterion given below, some of these twin systems may get activated. This method is used to activate the primary systems that undergo twinning and deactivate the rest due to obstacles to twinning. The small probability

of cross twinning is also taken into consideration by allowing the twinning to happen after the twinning volume fraction passes the saturation volume fraction and satisfies the inequality criterion described below. The algorithm used for arresting twinning is summarized below:

$f < f_{sat}$ twinning is allowed
$f > f_{sat}$ twinning is allowed only if $f > P_f$

where P_f is a random variable. In this chapter, P_f is assumed to have a uniform random distribution between 0.3 and 1.0 [7] and f_{sat} is assumed to be 0.2 as suggested in [6].

1.6 Numerical results

1.6.1 Example 1: Validation of texture evolution for Titanium

In this example texture evolution is examined for Titanium which has a HCP structure. A plane strain compression mode is assumed with a true strain rate equal to unity. The active slip and twinning systems are shown in Table 1.1. The values used for the elastic moduli are the following [18]:

$C_{11} = 256.6\ GPa$, $C_{12} = 0.36\ GPa$, $C_{13} = 69.7\ GPa$, $C_{33} = 325.13\ GPa$, $C_{55} = 46.71\ GPa$.

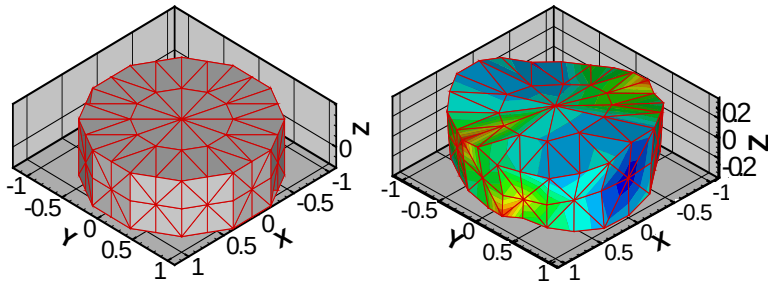

Figure 1.4: (left) - Initial random texture shown in Rodrigues fundamental space for HCP symmetries; (right) - Computed texture shown in Eulerian format.

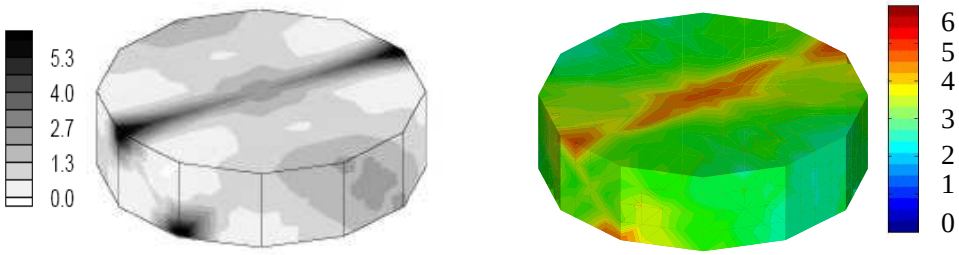

Figure 1.5: (left) - Computed texture shown in fundamental space from (Myagchilov and Dawson, 1999); (right) - Computed texture from this work.

Table 1.1: HCP slip system parameters (Staroselsky and Anand 2003)

Type	Slip plane normal	Slip direction
Basal	$\{0001\}$	$< 11\bar{2}0 >$
Prismatic	$\{10\bar{1}0\}$	$< 11\bar{2}0 >$
Pyramidal	$\{10\bar{1}1\}$	$< 11\bar{2}0 >$
Twin	$\{10\bar{1}2\}$	$< \bar{1}011 >$

No grain boundary effect is considered for this example. The following material parameters for slip and twinning systems are used for constitutive model: $s_{basal} = 8.0\ MPa$, $s_{prismatic} = 1.0\ MPa$, $s_{pyramidal} = 10.0\ MPa$ and $s_{twin} = 1.25\ MPa$.

The initial texturing of the material is assumed to be random. The orientation distribution function is represented in Rodrigues space in Fig. 1.4. The reference fundamental region is obtained from this space after applying the necessary HCP crystal symmetries. It is discretized into 111 tetrahedral elements. The total Lagrangian ODF corresponding to an effective strain of $\varepsilon = 0.5$ is shown in Fig. 1.5. It is in a very good agreement with the results of [6] shown in the same figure.

1.6.2 Example 2: Validation of constitutive model and texture evolution for Titanium

For validating the constitutive model α-titanium is used in this example. The result of stress-strain curve and final texture is compared with the experimental result reported in [19]. No grain boundary effect is considered for this example and the same slip and twinning systems as Example 1 are used with the following material parameters taken from [19]

$s_{basal} = 150\ MPa$, $s_{prismatic} = 30\ MPa$, $s_{pyramidal} = 120\ MPa$, $s_{twin} = 125\ MPa$.

It should be emphasized here that the differences between the material pa-

rameters used in [6, 19] is due to the fact that in [6] there was no attempt to match the stress-strain response with experimental results.

The initial texturing of the material is assumed to be random. The texture prediction for simple shear mode shown in Fig. 1.6 is in a good agreement with experimental results reported by Wu et al. [19]. The predicted result captures the strong textures in $\{0001\}$ and $\{10\bar{1}0\}$ pole figures. Although the work in [19] failed to completely capture the strong features seen in $\{0001\}$ pole figure obtained from experiment, the present work was able to show a good agreement with the experimental result.

Finally, the predicted stress-strain response for the simple shear mode is compared with experimental data in Fig. 1.7. The experimental data and numerical result reported in [19] are in good agreement with the computed result in this work. It should be emphasized that in [19] a strain hardening model is used. The present work is thus able to capture well the strain hardening effect.

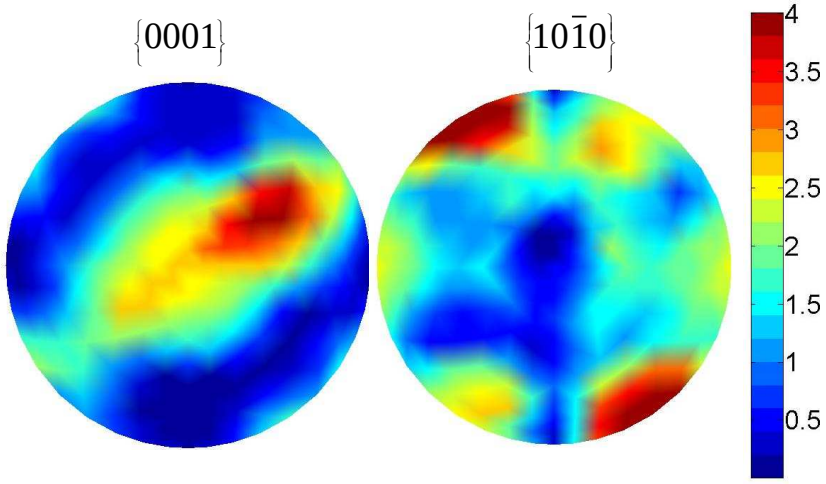

Figure 1.6: Computed crystallographic texture in simple shear for α-Ti at γ=-1.00.

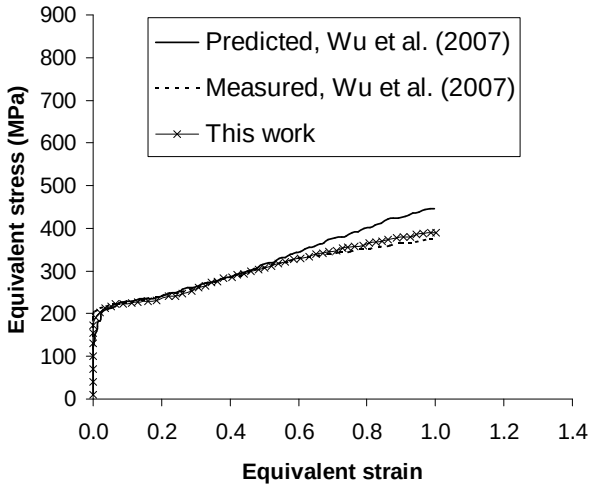

Figure 1.7: Comparison between experimentally measured and numerically simulated stress-strain curve (Wu et al., 2007) and the result from this work.

1.6.3 Example 3: Validation of constitutive model and texture evolution for magnesium alloy AZ31B

To examine the constitutive model and the algorithm for texture evolution, magnesium alloy AZ31B $(96.486\%\ Mg, 2.798\%\ Al, 0.715\%\ Zn, Balance, Mn, Fe)$ is studied. The experimental results taken from [7] are obtained from a hot-extruded rod of alloy AZ31B subjected to tension and simple compression tests. The initial texture of the specimen is shown trough $\{0001\}$ and $\{10\bar{1}0\}$ pole figures in Fig. 1.8. The material is subjected to a simple tension test with a constant true strain rate $2 \times 10^{-4}\ s^{-1}$. The following values are used for the elastic moduli [20]:

$C_{11} = 58$ GPa, $C_{12} = 25$ GPa, $C_{13} = 20.8$ GPa,

$C_{33} = 61.2$ GPa, $C_{55} = 16.6$ GPa.

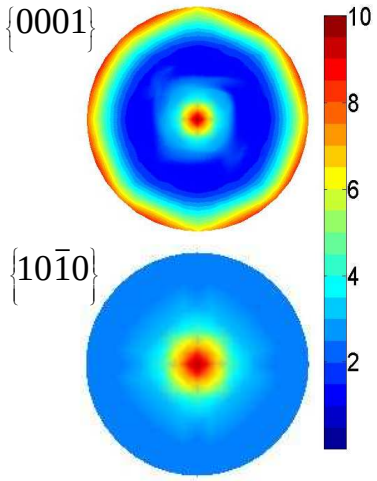

Figure 1.8: Initial texture used in this work for Mg.

The operative slip and twinning systems are assumed to be basal $(0001) < 11\bar{2}0 >$, prismatic $10\bar{1}0 < 11\bar{2}0 >$, pyramidal $10\bar{1}1 < 11\bar{2}0 >$ slip systems and pyramidal $10\bar{1}2 < \bar{1}011 >$ twinning systems. These are shown in Table 1.1. The material parameters used for constitutive model are:

$s_{basal} = 0.55\ MPa$, $s_{prismatic} = 105\ MPa$, $s_{pyramidal} = 105\ MPa$, $s_{twin} = 18\ MPa$.

for slip and twinning systems and

$s_{th} = 170\ MPa$, $s = 220\ MPa$, $\dot{\varepsilon}_0 = 0.001\ s^{-1}$, $m = 0.07$, $\xi = 0.05$

for grain boundary accommodation [7].

The calculated $\{0001\}$ and $\{10\bar{1}0\}$ pole figures after 15% strain in simple tension are shown in Figure 1.9. Comparison between the final computed texture from the current study and the experimental data from [8] shows a good agreement. We believe that the failure of the computed crystallographic texture to show a perfect symmetric pattern in the $\{10\bar{1}0\}$ polefigure is due to the fact that

the current model considers the texture as a continuous distribution and spatial configuration of crystals is neglected. Whereas, in the experiment reported by Staroselsky and Anand [8] both the initial and final textures correspond to a specific spatial configuration of crystals.

The stress-strain curve is also compared in Fig. 1.10 with the results given in [7]. In [7], the polycrystal is modeled as a discrete set of orientations, whereas in this work, ODF representation of the polycrystal is used to avoid the dependency of the final result on the initial selection of the spatial configuration of the orientations. This work provides a general approach by representing all the structures that have the same orientation distribution. Although in both cases the initial pole figures look alike, the analysis in [7] is based on a specific selection and ordering of crystal orientations in the model. They argue that they select the initial orientation of their discrete crystals such that they obtain the desired pole figures for the initial texture. In contrast, in the current method all textures with the desired pole figures are considered through the orientation distribution function. If a discrete representation of texture is used, one needs to split the finite elements to take into consideration the newly generated orientations due to twinning. In this work, however, application of a continuous representation of texture eliminates this problem.

The predictive capabilities of the model were also tested for the simple compression mode. The stress-strain curve is compared in Fig. 1.11. The computed result for texture evolution is given in Figure 1.12 and shows good agreement with the experiment data reported by Staroselsky and Anand [7].

Comparing Figs. 1.10 and 1.11, we note that the already reported [7] asymmetric behavior of tension and compression modes is apparent. This behavior

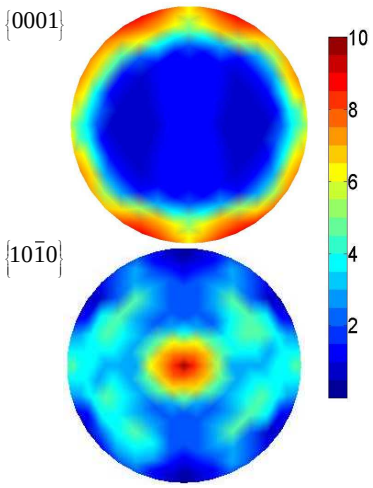

Figure 1.9: Computed crystallographic texture in simple tension for the tensile strain of 15%.

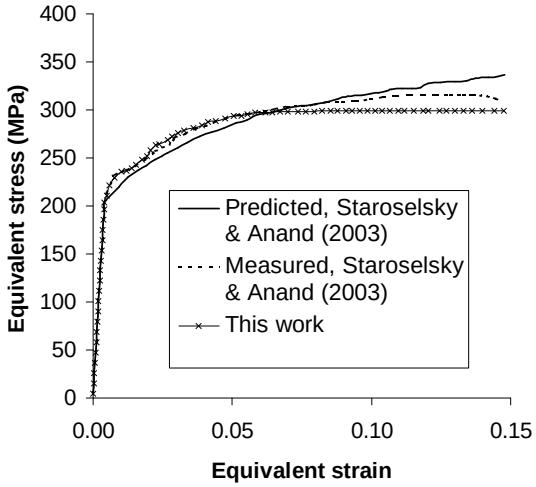

Figure 1.10: Comparison between experimentally measured and computed stress-strain response from (Staroselsky and Anand, 2003) and the result from this work.

can be explained by the evolution of the texture. The compressive mode of deformation and the initial texture makes the twinning and basal slipping to be more active. During the texture evolution the crystals align their c axis along the compression direction which makes the resolved shear stress on the basal plane to be very small and the pyramidal slip systems become active [7].

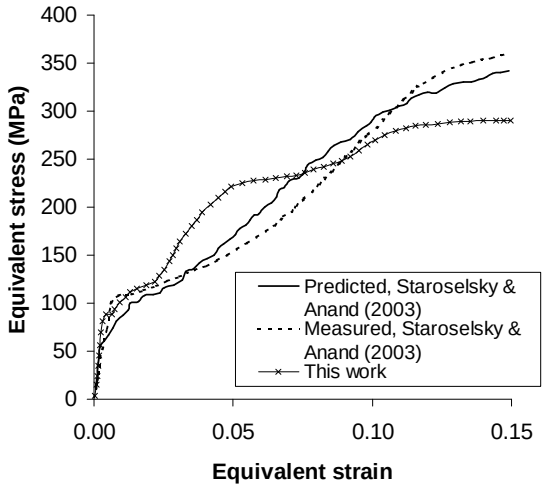

Figure 1.11: Comparison between experimentally measured and numerically simulated stress-strain curve (Staroselsky and Anand, 2003) and the result from this work for the simple compression mode.

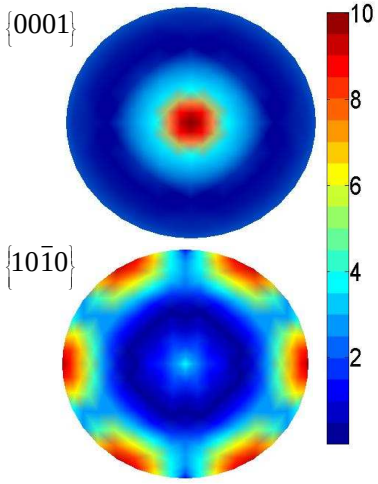

Figure 1.12: Numerically simulated crystallographic texture in simple compression for the compressive strain of 18%.

Again, the experimentally measured and numerically modeled response show a good agreement. The reader should notice that the model used by Staroselsky and Anand [7] considers the actual spatial configuration of the crystals and as they point out in their paper due to the non-hardening model used, the observed strain hardening is related to the evolution of the microstructure.

Considering the fact that the current model neglects the exact spatial configuration of microstructure and uses a 1-st order representation, the stress-strain result shows an acceptable agreement with that of experiment. Notice that although a non-hardening model is used this work is able to capture the hardening part of the stress-strain curve by restricting the twinning after the saturation limit is met. The strain hardening curve is also shown in Fig. 1.13. The same trend for strain hardening in simple compression mode is reported in [19]. It should be noticed that the f_{sat} and probability function P_f discussed earlier are responsible for the different stages seen in the figure.

Looking at Eq. (1.30) and neglecting the grain boundary effect for now (assuming $\xi = 0$) makes this more clear. It is obvious that the role of the second term on the right hand side is to reduce the amount of stress. This reduction is caused proportional to the amount of plastic strain.

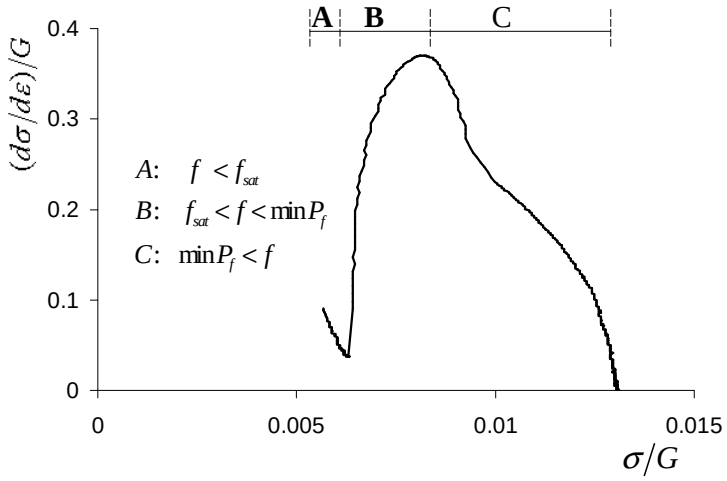

Figure 1.13: Normalized strain hardening response of magnesium alloy AZ31B in simple compression. A, B and C represent three different stages. f, f_{sat} and P_f are defined in Section 5.1.

When volume fraction of the twinned part is less than f_{sat} all systems are allowed to contribute to the flow rule which causes stage A in which strain

hardening is decreasing. After reaching f_{sat} the corresponding twin systems are taken out of the active systems which makes it harder for the plastic strain to develop, hence mimicking stage B which has an increasing strain-hardening rate. After the volume fraction of the twinned part passes the lower range of the P_f function, there will be a probability of including the twin systems in the active systems. This in turn initiates stage C which is characterized by a decreasing strain hardening rate.

From this example it is apparent that the method discussed in this work is able to reproduce the stress-strain relation and texture evolution of magnesium alloy AZ31B.

1.7 Conclusions

In this chapter, a continuum approach for representing HCP polycrystals undergoing both slip and twinning is presented using a Lagrangian framework. The proposed methodology is applied for Titanium and Magnesium alloy AZ31B and the computed texture and stress-strain response have shown to be in good agreement with experiments and results from other numerical approaches. The need for splitting existent elements to allow for newly generated orientations is eliminated by using a continuous method in the space of ODFs. This continuous method is general and can be used with any single crystal constitutive model. In addition, the probabilistic approach presented here is able to match experimental results using only a few parameters. In fact, the current non-hardening model is able to capture the macro- and micro-behavior of polycrystals without a need to search for hardening parameters. The proposed methodology is

based on reported physical phenomena of twinning like saturation of twinning and existence of different stages in the strain-hardening regime.

The continuum representation of the texture used in this chapter represents the volume fraction of crystallographic orientations but it neglects the size, topology and shape of the grains or equivalently the location of grain boundaries. The author of this chapter recognizes the fact that considering the spatial configuration of crystals provides models with greater abilities to match the experimental outputs. The merit of the current methodology lies in its simplicity and ability to handle more general spatial configurations. As all the textures that match the volume fraction of crystallographic orientations are lumped into one model, this provides a great tool for fast exploration of the process/structure/property space. In addition, the continuous representation of texture provides a natural framework for designing of texture dependent properties using a mathematically rigorous continuum sensitivity method (CSM) [4, 21]. Hence, the current model while better than continuum phenomenological models, provides a computationally affordable framework and at the same time reasonably represents the microstructural behavior.

When a viable texture distribution is obtained for desired material properties, a more accurate model can be used to investigate the effect of spatial distribution of the microstructure.

CHAPTER 2

MODELING MICROSTRUCTURAL AND PROCESS UNCERTAINTIES IN DEFORMATION PROCESSES

2.1 Introduction

The need for designing optimized components in aerospace, naval and automotive applications that lead to reduction in material utilization, process cost and fuel consumption has grown significantly in recent years. Polycrystalline alloys have many applications in these industries.

Macro-scale properties of polycrystalline alloys depend on the preferred orientation of crystals in the underlying microstructure manifested as the crystallographic texture. During forming processes, mechanisms such as crystallographic slip and lattice rotation drives the formation of texture. Variation in such processes and the initial texture of the material subjected to these processes have a significant effect on the final macro-scale properties. Obtaining the variation in material properties due to inherent randomness of the microstructure or the processing parameters is an important component in any design. Figure 2.1 shows a workpiece and the underlying microstructure of one point on macro-scale. The information on microstructure is usually provided in the form of x-ray diffraction images of the representative volume element (RVE). Having complete knowledge of the initial microstructure of workpiece enables one to obtain the evolved microstructure due to the effect of various deformation processes performed on the workpiece to obtain a specific shape. The calculation of evolved microstructure in turn enables one to obtain the macro-scale properties of the final product. The fact that the initial workpieces may have a random

initial microstructure or that the deformation process may have some uncertain parameter has significant effect on the macro-scale properties that one can expect from the final product of a deformation process (Fig. 2.1). This leads one to use stochastic methods in calculating the effect of uncertainties in initial texture and process parameters on final macro-scale properties of the workpiece.

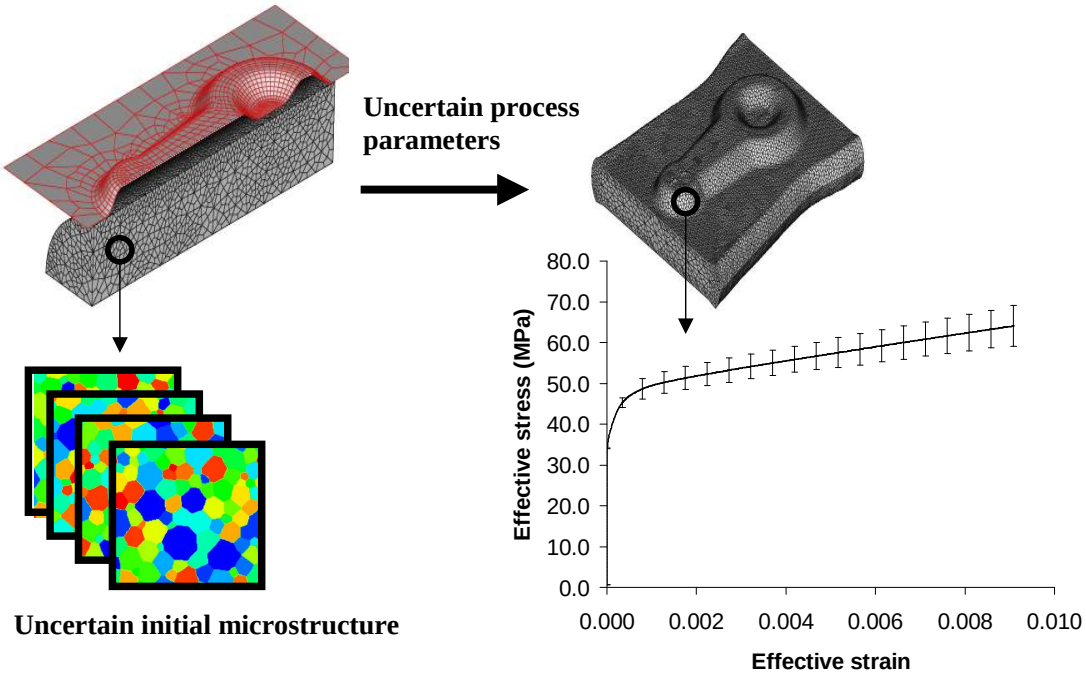

Figure 2.1: Schematic view of the effect of uncertainty in initial texture on final material properties

Recent developments in materials-by-design have focused on integrating processing, structure and property of the materials. Two such methods have been reported in [22] using a spectral framework and in [23] using local supports of finite element representation . In these methods a convex hull of properties that can be obtained from a specific process is constructed. In none of the current methods the propagation of uncertainty in different stages of processes has been studied in a mathematically rigorous framework. One of the aims of this chapter is to fill this gap.

For this purpose the evolution of texture is modeled as a stochastic partial differential equation (SPDE). There has been tremendous progress in posing and solving SPDEs. Several techniques like Generalized Polynomial Chaos expansion [24, 25, 26, 27, 28] and collocation based strategies [29, 30, 31, 32] have been developed to solve SPDEs.

In modeling the texture evolution, the random initial texture can be represented as a random field. The recent works in [33, 34] propose methods for reducing a random field to a set of random variables. The available information on initial microstructure provided as a set of x-ray diffraction images is rarely enough to completely define the aforementioned random field. In this situation one needs to resort to maximum entropy approach in which the random field is constructed such that the entropy of the information it conveys is maximized. The method used in this work is fairly general and as the information on microstructure increases it can be easily incorporated in approximating the random field.

Finally, a stochastic framework is presented for obtaining the convex hull of properties obtained from a material subjected to uncertain process parameters and initial texture. The contribution of this chapter is as follows. (1)- A data driven strategy is provided to encode the limited information on texture and represent it in a finite-dimensional framework. (2)- A stochastic collocation methodology is used to incorporate the effect of uncertainty in initial texture and process parameters on the final texture. (3) The stochastic characteristic of the final texture obtained from the previous step is used to obtain the stochastic characteristic of the macro-scale properties of the material subjected to a specific process.

The layout of this chapter is as follows. Section 2 provides the problem definition. Section 3 and 4 give details on constitutive model and texture evolution for the polycrystal plasticity respectively. Section 5 contains the algorithm for constructing a lower order model for stochastic representation of texture. Sections 6 to 8 contain details on the method used in solving the stochastic differential equations. In Section 9 a method in constructing the convex hull of material properties is presented. Sections 10 and 11 are for numerical examples and conclusion respectively.

2.2 Constitutive problem and texture evolution

During a deformation process, crystallographic slip and re-orientation of crystals (lattice rotation) can be assumed to be the primary mechanisms of plastic deformation. The slip and re-orientation occur in an ordered manner such that a preferential orientation or texture develops. We follow the rate-independent constitutive model for FCC polycrystals developed in [40].

Consider a point in the reference fundamental region that corresponds to a particular crystal orientation. In an appropriate kinematic framework, the total deformation gradient is decomposed into plastic and elastic parts, $\boldsymbol{F} = \boldsymbol{F}^e\ \boldsymbol{F}^p$, where $\boldsymbol{F}^e$ is the elastic deformation gradient and $\boldsymbol{F}^p$, the plastic deformation gradient, with $\det\boldsymbol{F}^p = 1$. The constitutive relation is given by

$$\bar{\boldsymbol{T}} = \boldsymbol{\mathcal{L}}^e \left[\bar{\boldsymbol{E}}^e\right] \tag{2.1}$$

where $\bar{\boldsymbol{T}}$ is the second Piola-Kirchhoff stress tensor, $\boldsymbol{\mathcal{L}}^e$ is the fourth-order anisotropic elasticity tensor expressed in terms of the crystal stiffness parameters and the orientation $\boldsymbol{r}$ and $\bar{\boldsymbol{E}}^e = \frac{1}{2}\left(\boldsymbol{F}^{eT}\boldsymbol{F}^e - \boldsymbol{I}\right)$. The re-orientation velocity

is found as follows:

$$\boldsymbol{v} \;=\; \frac{\partial \boldsymbol{r}}{\partial t} \;=\; \frac{1}{2}\left(\boldsymbol{\varpi} \;+\; (\boldsymbol{\varpi}\cdot\boldsymbol{r})\boldsymbol{r} \;+\; \boldsymbol{\varpi}\times\boldsymbol{r}\right) \tag{2.2}$$

where $\boldsymbol{r}$ is the orientation (Rodrigues' parameterization) and $\boldsymbol{\varpi}$ represents the spin vector defined as $\boldsymbol{\varpi} \;=\; \text{vect}\left(\dot{\boldsymbol{R}}^{e}\boldsymbol{R}^{eT}\right)$, where $\boldsymbol{R}^{e}$ is evaluated through the polar decomposition of the elastic deformation gradient $\boldsymbol{F}^{e}$ as $\boldsymbol{F}^{e} \;=\; \boldsymbol{R}^{e}\boldsymbol{U}^{e}$.

Consider a macroscopic material point and an associated underlying microstructure $\mathcal{M}$ discretized by a finite element grid. Each point on this underlying grid corresponds to a different crystal orientation $\boldsymbol{R}$. At each point on the grid, the crystal lattice frame $\hat{\boldsymbol{e}}_i$ is related to the sample reference frame $\boldsymbol{e}_i$ by $\boldsymbol{e}_i = \boldsymbol{R}\,\hat{\boldsymbol{e}}_i$. Due to crystal symmetry, the orientation $\boldsymbol{R}$ is not unique. Restricting the Rodriguez domain to a fundamental zone that reflects the crystal symmetry leads to a one to one correspondence between the points on the Rodriguez space and the crystal orientation.

The Rodrigues-Frank axis-angle parameterization is used as a convenient scheme to represent $\boldsymbol{R}$ [44]. The parameterization is derived from the natural invariants of $\boldsymbol{R}$: the axis of rotation $\boldsymbol{n}$ and the angle of rotation ζ. The angle-axis parameterization, $\boldsymbol{r}$, is obtained by scaling the axis $\boldsymbol{n}$ by a function of the angle ζ as $\boldsymbol{r} \;=\; \boldsymbol{n}\; f(\zeta)$. In the particular case of Rodrigues' parameterization, the function is defined as $f(\zeta) \;=\; \tan\left(\frac{\zeta}{2}\right)$.

To represent a particular texture, an orientation distribution function $A(\boldsymbol{r})$ is defined on a three-dimensional bounded domain $\mathcal{R}$ called Rodrigues space that describes the crystal density over the fundamental region [35, 37, 38]. Through such a description, the microstructure is treated as a continuum of crystals. The representation of the ODF in an Eulerian framework is $A(\boldsymbol{r},t)$, while in a Lagrangian framework is given as $\hat{A}(\boldsymbol{s},t)$, where $A(\boldsymbol{r},t) \;=\; A(\hat{\boldsymbol{r}}(\boldsymbol{s},t),t) \;=\; \hat{A}(\boldsymbol{s},t)$,

with $\hat{\boldsymbol{r}}$ the re-orientation vector.

For cubic symmetry, the fundamental zone is shown in Fig. 2.2a. It can be shown [42] that each symmetry rotation ζ along axis $\boldsymbol{n}$ translates to a pair of planes in Rodrigues space with normals $\pm\boldsymbol{n}$ at a distance equal to tan $\left(\frac{\zeta}{4}\right)$ from the origin. The inner envelope of the planes created due to symmetry is the fundamental zone. For example in the cubic symmetry case, the faces of the fundamental zone are due to symmetry rotations about $< 100 >$ family of axes and their distance to the origin is tan $(\pi/8)$. The corners of the fundamental zone are due to the planes created by the symmetry rotations along $< 111 >$ axes and their distance to the origin is tan $(\pi/6)$ [42].

Orientations on each parallel pair of planes that form the faces and corners of the fundamental zone are equivalent under the symmetries. In the cubic fundamental region, orientations on the parallel pairs of $\{100\}$ faces are equivalent by an offset. This offset is determined by rotation of $\pi/4$ about the corresponding $< 100 >$ axes. The same equivalence holds for $\{111\}$ faces where the offset is a rotation of $\pi/3$ about the corresponding $< 111 >$ axes [42].

The Lagrangian scheme for the ODF evolution as described in [35] is used. The evolution of the ODF is governed by the ODF conservation equation and is given in the Lagrangian form as follows

$$\frac{\partial \hat{A}(\boldsymbol{s},t)}{\partial t} + \hat{A}(\boldsymbol{s},t) \bigtriangledown \cdot \boldsymbol{v}(\boldsymbol{s},t) \ = 0 \tag{2.3}$$

where $\boldsymbol{v}(\boldsymbol{s},t)$ is the Lagrangian re-orientation velocity of the crystals and the Lagrangian form of the ODF, $\hat{A}(\boldsymbol{s})$, is subjected to $\hat{A}(\boldsymbol{s},0) = \ \hat{A}_0(\boldsymbol{s})$ as the initial condition.

Texture evolution is modeled using the above equation. The texture is repre-

sented by the ODF on a grid representing the discretized fundamental region of the Rodrigues' parameter space. For the evolution of texture, the conservation equation for the ODF is solved using the finite element method. The constitutive model is solved at each integration point of this grid which represents an orientation and is connected to the macro-scale through the Taylor hypothesis. The response of the underlying microstructure is calculated using a polycrystal plasticity model [40].

Figure 2.2 shows an example of the evolved texture for a Copper polycrystal subjected to a simple compression mode. The texture is provided in the form of orientation distribution function and is plotted over the fundamental part of Rodrigues space for FCC crystal structure. The corresponding stress-strain response is also provided in this figure.

The polycrystal average of an orientation dependent property, $X(\boldsymbol{s}, t)$, is determined as:

$$\langle X \rangle \quad = \quad \frac{\int\limits_{\mathcal{R}} X(\boldsymbol{s})\ \hat{A}(\boldsymbol{s})\ dv}{\int_{\mathcal{R}} \hat{A}(\boldsymbol{s})\ dv} \tag{2.4}$$

Here, $dv = (\det g)^{0.5} ds_1 ds_2 ds_3$. Since the orientation space is non-Euclidean, the volume element is scaled by the term $(\det g)^{0.5}$ where g is the metric for the space.

2.3 Problem definition: Process and texture uncertainty

The main focus of this work is to obtain the effect of random process parameters and initial texture on the macro-scale properties of polycrystalline materials.

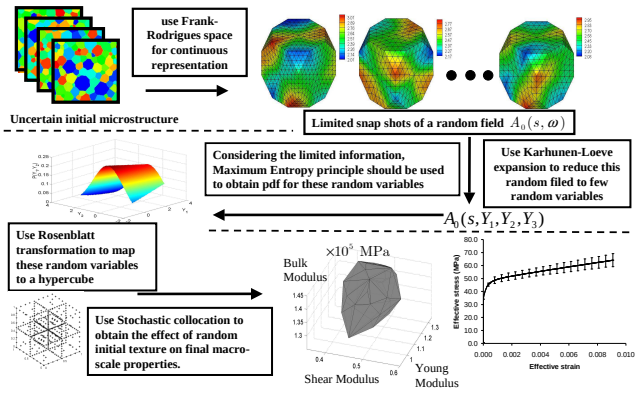

Figure 2.2: (a) Texture obtained for an FCC Copper polycrystal subjected to a simple compression mode is shown over the fundamental part of Rodrigues space. (b) Comparison of the equivalent stress-strain response with the results of [40].

For this purpose, the convex hull of the material properties obtainable in the presence of this uncertainty is computed.

Consider a complete probability space (Ω, F, P) where Ω is the event space, F the σ-algebra, and $P : F \rightarrow [0,1]$ is the probability measure. For a simple example with a discrete event space, let us consider an experiment with rolling a loaded die where one loses if the outcome is less than or equal to 3 and wins when the outcome is greater than 3. In this case, the event space is $\Omega = \{1,2,3,4,5,6\}$ and the σ-algebra (a nonempty collection of subsets of Ω that is closed under complementation and countable union of its members) is $F = \{\{1,2,3\},\{4,5,6\},0,\Omega\}$ and P is the probability associated with the members of F [43].

The uncertainty in the problem we consider comes from: (a) variation in the velocity gradient representing the variation in process parameters: $L(\omega), \omega \in \Omega$ and (b) variation in the initial texture: $\hat{A}_0(s,\omega)$; $s \in \mathcal{R}$, $\omega \in \Omega$.

The velocity gradient is written in terms of various deformation modes such

as tension/compression, plain strain compression, shear and rotation. The coefficients of these terms $\beta_1, \ldots, \beta_8$ can be assumed as random variables to represent variation in process conditions.

$$
\begin{aligned}
L &= \beta_1 \begin{pmatrix} 0 & 1 & 0 \\ 1 & 0 & 0 \\ 0 & 0 & 0 \end{pmatrix} + \beta_2 \begin{pmatrix} 0 & 0 & 0 \\ 0 & 1 & 0 \\ 0 & 0 & -1 \end{pmatrix} + \beta_3 \begin{pmatrix} -1 & 0 & 0 \\ 0 & 0.5 & 0 \\ 0 & 0 & 0.5 \end{pmatrix} \\
&+ \beta_4 \begin{pmatrix} 0 & 0 & 1 \\ 0 & 0 & 0 \\ 1 & 0 & 0 \end{pmatrix} + \beta_5 \begin{pmatrix} 0 & 0 & 0 \\ 0 & 0 & 1 \\ 0 & 1 & 0 \end{pmatrix} + \beta_6 \begin{pmatrix} 0 & -1 & 0 \\ 1 & 0 & 0 \\ 0 & 0 & 0 \end{pmatrix} \\
&+ \beta_7 \begin{pmatrix} 0 & 0 & -1 \\ 0 & 0 & 0 \\ 1 & 0 & 0 \end{pmatrix} + \beta_8 \begin{pmatrix} 0 & 0 & 0 \\ 0 & 0 & -1 \\ 0 & 1 & 0 \end{pmatrix}
\end{aligned} \tag{2.5}
$$

The incompressibility condition is assumed here and only eight components of L are independent and hence $\boldsymbol{\beta}$ consists as well of eight components.

One can use a random field, $\hat{A}_0(s, \omega)$; $s \in \mathcal{R}$, $\omega \in \Omega$ to represent the variability of the initial texture. The stochastic partial differential equation for the evolution of texture, $\hat{A}(s, t, \omega) : \mathcal{R} \times [0, T] \times \Omega \to \mathbb{R}^+ \cup \{0\}$, can be written such that for P-almost everywhere $\omega \in \Omega$

$$
\frac{\partial \hat{A}(\boldsymbol{s}, t, \omega)}{\partial t} + \hat{A}(\boldsymbol{s}, t, \omega) \bigtriangledown \cdot \boldsymbol{v}(\boldsymbol{s}, t, \omega) \ = 0 \tag{2.6}
$$

The Karhunen-Loève expansion can be used to reduce the random field $\hat{A}_0(s, \omega)$ to a set of finite number of random variables $\hat{A}_0(s, Y_1, \ldots, Y_N)$. Using the finite-dimensional noise assumption, the random field $\hat{A}(s, t, \omega)$ can be decomposed into a finite number of random variables $\hat{A}(s, t, Y_1, \ldots, Y_{N+n_L})$ where the extra number of dimensions (n_L) comes from the random variables representing uncertainty in the velocity gradient ($n_L \in \mathbb{N}, n_L \leq 8$).

In this work, we follow a data-driven approach. We assume that a few snapshots of the random field $\hat{A}_0(s,\omega)$ are known (from experiments or simulation) from which low-order statistics (mean, covariance, etc.) of the initial texture can be extracted. In reducing the order of the stochastic model representing the random initial texture using the Karhunen-Loève expansion, a random field is approximated by a set of (not necessarily independent) N random variables whose probability distribution depends on the random field under study (see Section 2.4). In absence of enough snapshots of the random field to obtain a convergent estimation for these probability distributions, one needs to resort to the Maximum entropy (MaxEnt) principle in which a joint probability density is constructed for these random variables that satisfies a set of constraints imposed on the random variables and maximizes the information entropy. The maximum entropy approach has been utilized in [39] for constructing microstructures with known stochastic moments of their grain sizes. The method relied on a pixel-based representation of microstructures and in this case the MaxEnt principle resulted in a probability distribution of grain sizes that depended implicitly on the microstructure. However, in the method used in this work, the random field representing the microstructure is first reduced to a set of random variables using the Karhunen-Loève expansion and then the MaxEnt approach is used to obtain a joint probability distribution that depends explicitly on these variables. The set of constraints imposed on MaxEnt are the result of the Karhunen-Loève expansion (see Section 2.4). After obtaining the joint probability distribution, the Rosenblatt transformation [57] can be used to transform the set of N random variables to another set of N independent identically distributed uniform random variables in a unit hypercube $[0,1]^N$. This allows us to sample in this space and seamlessly use existent collocation algorithms [31] to

obtain the probabilistic distribution of the final texture of a point on the macro-scale as a result of the random initial texture (see Section 3.4). Additional input uncertainty can also be considered to include process variability in a single or a sequence of deformation processes, $\hat{A}(s, T_{final}, Y_1, \ldots, Y_{N+n_L})$. Having full statistical description of the final texture enables us to compute the convex hull of the properties obtainable at the end of a deformation process considering uncertainty in process parameters and initial texture. This convex hull is a valuable tool for designers who want to know of the effect of input uncertainty on the properties they can expect for the material under study.

2.4 Constructing a low-order stochastic model for representation of texture

The initial texture has a significant effect on the final properties obtainable from a material. To incorporate the effect of randomness in initial texture on the final property of the microstructure, the initial texture is presented as a random field. In this section, a method is introduced for the representation of the orientation distribution function as a random process.

2.4.1 Karhunen-Loève expansion

The Karhunen-Loève expansion is a useful tool for constructing a reduced-order model of a random field with a given covariance structure. In this method, a random field can be represented by a linear combination of an infinite number of uncorrelated random variables. Assume a stochastic field $\hat{A}_0(s, \omega)$ (we drop

the subscript 0 from now on for ease of notation) defined on a probability space (Ω, F, P)

$$\hat{A}(s,\omega) : \mathcal{R} \times \Omega \to \mathbb{R}^{+} \cup \{0\} \tag{2.7}$$

where $\mathcal{R}$ is the fundamental part of Rodrigues space, Ω is the set of elementary events and $\omega \in \Omega$. One can use the Karhunen-Loève expansion to express this field by a linear combination of some orthogonal functions [48]. In this method, one uses the spectral decomposition of the covariance function $\mathbf{R}_{\hat{\boldsymbol{A}}\hat{\boldsymbol{A}}}$ of the field.

Let the following random vector represent the discretization of the texture $\hat{\boldsymbol{A}} = (\hat{A}(s_1,\omega), \ldots, \hat{A}(s_{n_m},\omega))$, where here n_m is the number of nodes on the grid discretizing the Rodrigues space. If the underlying covariance matrix of $\hat{\boldsymbol{A}}$ is $\boldsymbol{C}$, then its unbiased estimate can be written as

$$\widetilde{\boldsymbol{C}} = \frac{1}{M-1}\sum_{i=1}^{M}(\hat{\boldsymbol{A}}_i - \overline{\boldsymbol{A}})^T(\hat{\boldsymbol{A}}_i - \overline{\boldsymbol{A}}) \tag{2.8}$$

$$\overline{\boldsymbol{A}} = \frac{1}{M}\sum_{i=1}^{M}\hat{\boldsymbol{A}}_i$$

where $\hat{\boldsymbol{A}}_i$ is the ith realization of $\hat{\boldsymbol{A}}$ and M is the total number of known realizations.

The Karhunen-Loève expansion of the random vector $\hat{\boldsymbol{A}}$ can be written as

$$\hat{A}(s,\omega) = \overline{A}(s) + \sum_{i}\sqrt{\rho_i}f_i(s)Y_i(\omega) \tag{2.9}$$

where f, ρ represent the eigenfunctions and eigenvalues of $\widetilde{\boldsymbol{C}}$, respectively,

and $Y_i(\omega)$ is a set of uncorrelated random variables with the following two properties (with $E(.)$ here denoting the expectation operator)

$$\begin{aligned} E(Y_i(\omega)) &= 0 \\ E(Y_i(\omega)Y_j(\omega)) &= \delta_{ij}, \quad i,j = 1,\ldots,N \end{aligned} \tag{2.10}$$

Since the covariance function is symmetric and positive definite, all the eigenvalues are positive real numbers and the eigenvectors are mutually orthogonal and they span the space in which $\hat{A}(s,\omega)$ belongs to. The summation in Eq. (2.9) is mean square convergent and usually it can be truncated after few dominant terms. The number of terms N is usually selected in practice such that it guarantees $(1-\sum_{i=1}^{N}\rho_i/\sum\rho_i) \leq \epsilon$ where ϵ is a small number close to zero. Furthermore, realizations of the uncorrelated random variables can be obtained by

$$Y_i^j = \frac{1}{\sqrt{\rho_i}} < \hat{\boldsymbol{A}}_j - \overline{\boldsymbol{A}}, \boldsymbol{f}_i >_{l_2}; \;\; j = 1,\ldots,M, \;\; i = 1,\ldots,N \tag{2.11}$$

where Y_i^j is the jth realization of the random variable Y_i, $\hat{\boldsymbol{A}}_j$ is the jth realization of the random field and $<,>_{l_2}$ is the scalar product in $\mathbb{R}^{n_m}$. Hence, the spatial randomness of the process is decomposed to a set of deterministic functions (that represent the fluctuation of the process in the spatial domain) multiplied by some uncorrelated random variables whose distribution depends on the nature of the process [48]. Using the random process to represent material properties that vary smoothly allows one to use only few terms of the expansion to obtain a good approximation. In this case, the eigenvalues corresponding to the neglected terms drop quickly to negligible values and the presence of $\sqrt{\rho}$ in Eq. (2.9) guarantees that they do not have a significant effect.

If $\hat{A}(s,\omega)$ is a Gaussian random field, the random variables $Y_i(\omega)$ are independent Gaussian random variables with mean zero and variance one. In practice $\hat{A}(s,\omega)$ is usually non-Gaussian. In the presence of sufficient data, Eq. (2.11)

can be used for obtaining the probability distribution of these random variables [49, 50]. In most cases, the number of realizations of the random process is not enough to construct a converging probability distribution (with respect to the number of realizations). In such cases, one can use the Maximum Entropy (MaxEnt) principle [51] in constructing the probability distribution $(p_{\boldsymbol{Y}})$ of these random variables. The MaxEnt principle provides the probability distribution satisfying the information we have about $\boldsymbol{Y}$ and maximizes the information entropy for part of the information we do not possess.

Furthermore, the ODF representing the texture takes nonnegative values. Hence, the Karhunen-Loève approximation should provide us with nonnegative values. Since the orientation distribution function can take values very close to zero for certain orientations, the selection of A_{min} becomes very ad hoc and the resulting random field may have unbounded second moments.

The nonnegative property of $\hat{A}(s,\omega)$ is enforced by a set of inequalities obtained from Eq. (2.9) as

$$\overline{A}(s) + \sum_i \sqrt{\rho_i} f_i(s) Y_i(\omega) \geq 0, \quad \forall s \in \mathcal{R} \tag{2.12}$$

Solving a vertex enumeration problem in linear programming, this convex set of inequalities can be converted into a convex hull whose vertices consist of the intersections of these inequalities.

$$\boldsymbol{a} + \boldsymbol{b}\boldsymbol{Y} \geq 0 \quad a.s. \tag{2.13}$$

where a.s. indicates that the inequality almost surely (with probability one) holds. This convex hull acts as the support of the joint probability distribution

sought for in the MaxEnt methodology (see next subsection).

2.4.2 Probability distribution of the random variables using the maximum entropy (MaxEnt) principle

Let $\boldsymbol{Y} = (Y_1, \ldots, Y_N)$ be the set of random variables for which the probability density function $p_{\boldsymbol{Y}}$ is unknown. This probability density function is assumed as a map from $\boldsymbol{D} \subset \mathbb{R}^N$ to $\mathbb{R}^+ = [0, +\infty[$ where $\boldsymbol{D}$ is the support of $p_{\boldsymbol{Y}}$ and is defined previously as the convex hull ($D = \{\boldsymbol{Y} : \boldsymbol{Y} \in convexhull\ Y_1, \ldots, Y_N \subset \mathbb{R}\}$) of all admissible values of $Y_1, \ldots, Y_N$. Any probability function should satisfy the following constraints in order to be acceptable for this problem.

$$E(\boldsymbol{f}(\boldsymbol{Y})) = \boldsymbol{M} \tag{2.14}$$

where $\boldsymbol{M} = (M_1, \ldots, M_h)$ is a given vector in $\mathbb{R}^h$ with h being the number of constraints defined in Eq. (2.10), E is the expectation and $\boldsymbol{Y} \to f(\boldsymbol{Y})$ is a given measurable mapping from $\mathbb{R}^N$ to $\mathbb{R}^h$. These conditions are the result of specific properties of the Karhunen-Loève expansion discussed in the previous section, see Eq. (2.10). Hence they can be written as

$$\begin{aligned} f(\boldsymbol{Y}) &= (\boldsymbol{Y}, \boldsymbol{e}(\boldsymbol{Y})) \\ \boldsymbol{M} &= (0_N, e) \end{aligned} \tag{2.15}$$

where $h = N + N(N+1)/2$,$0_N = (0, ..., 0) \in \mathbb{R}^N$, $\boldsymbol{e}(\boldsymbol{Y})$ is a vector in $\mathbb{R}^{N(N+1)/2}$

formed from the diagonal and upper triangular part of the matrix $\boldsymbol{Y}\boldsymbol{Y}^T$ and e is a vector in $\mathbb{R}^{N(N+1)/2}$ that has 0 and 1's as its elements.

Let us define the information entropy $S(p)$ of the probability density function p as

$$S(p) = -\int_D p(\boldsymbol{Y}) log(p(\boldsymbol{Y}))d\boldsymbol{Y} \tag{2.16}$$

If Ξ is the convex collection of all probability density functions defined on D which satisfy the above constraints and $\Xi \cap \{p : S(p) > -\infty\}$ is nonempty, then the Maximum Entropy principle consists of finding the probability distribution p that maximizes the information entropy:

$$p_{\boldsymbol{Y}} = arg \max_{p \in \Xi} S(p) \tag{2.17}$$

The MaxEnt problem can be posed as an unconstrained optimization problem using Lagrange multipliers. In this method the constraints are incorporated into the cost function as

$$C = S(p) + < \boldsymbol{\lambda}, (E(\boldsymbol{f}(\boldsymbol{Y})) - \boldsymbol{M}) >_h \tag{2.18}$$

where $\boldsymbol{\lambda} = (\lambda_1, \ldots, \lambda_h)$ represents the Lagrange multipliers. Maximizing this cost function is equivalent to maximizing the entropy and satisfying the constraints. Since $S(p)$ is a concave functional [53] the set $\{P : S(p) > -\infty\}$ is

convex and the uniqueness of $p_{\boldsymbol{Y}}$ as the solution of Eq. (2.17) is guaranteed [54]. It can be shown that the solution of the above problem can be represented as [33]

$$p(\boldsymbol{Y}) = Zexp(- < \boldsymbol{\lambda}, \boldsymbol{f}(\boldsymbol{Y}) >_h)\mathbb{I}_D(\boldsymbol{Y}) \quad \forall \boldsymbol{Y} \in D \tag{2.19}$$

where Z is a normalization constant and $\mathbb{I}_D(\boldsymbol{Y})$ the indicator function; $\mathbb{I}_D(\boldsymbol{Y}) = 1$ if $\boldsymbol{Y} \in D$ and $\mathbb{I}_D(\boldsymbol{Y}) = 0$, otherwise. The Lagrange multipliers are chosen such that they satisfy the constraints given in Eq. (2.14). When the number of constraints is small, the Lagrange parameters can be obtained by a simple gradient method but as the number of constraints becomes significant a dual approach [39, 55] can be used in which the problem is posed as an optimization problem in terms of the Lagrangian parameters. The dual optimization problem can be written as

$$\begin{aligned} \boldsymbol{\lambda}^* &= argmin \ \ (\boldsymbol{\lambda}) \\ (\boldsymbol{\lambda}) &= log(Z) + \sum_n \lambda_n M_n \end{aligned} \tag{2.20}$$

where $Z = \int_D exp(- < \boldsymbol{\lambda}, \boldsymbol{f}(\boldsymbol{Y}) >_h) d\boldsymbol{Y}$. The function $(\boldsymbol{\lambda})$ satisfies the following properties

$$\frac{\partial}{\partial \lambda_i} = -\boldsymbol{E}(f_i) + M_i, \ \ i = 1, \ldots, h \tag{2.21}$$

where M_i is defined in Eq. (2.15). From these equations, it is clear that the solution of Eq. (2.20) satisfies the constraints posed in Eq. (2.14). The solution

of the constrained optimization problem posed by the Maximum Entropy approach has the parametric form shown by Eq. (2.19) where $\boldsymbol{\lambda}$ can be inferred by minimizing the dual function $(\boldsymbol{\lambda})$. This means that the solution of the dual problem ($\boldsymbol{\lambda}^*$) corresponds to the $p(\boldsymbol{\alpha})$ that maximizes the entropy [39, 55, 56]. Furthermore, $(\boldsymbol{\lambda})$ is smooth and convex in $\boldsymbol{\lambda}$.

A gradient based optimization algorithm is used to solve the dual problem. This gradient method is briefly described in here.

Step 1. Assume an initial guess for the Lagrange multipliers $\boldsymbol{\lambda}^0$

Step 2. Set $\boldsymbol{u}_0 = v_0 = -\nabla \ (\boldsymbol{\lambda}^0)$

Step 3. Update the value of $\boldsymbol{\lambda}^{i+1}$ by minimizing along the direction v^i as follows:

$$\boldsymbol{\lambda}^{i+1} = \boldsymbol{\lambda}^i + argmin_d \ (\boldsymbol{\lambda}^i + \boldsymbol{v}^i d) \tag{2.22}$$

Step 4. Find $\boldsymbol{u}^{i+1} = -\nabla \ (\boldsymbol{\lambda}^{i+1})$

Step 5. Find the new conjugate direction (using a stabilized version of conjugate gradients [**?**]) as

$$\boldsymbol{v}^{i+1} = \boldsymbol{u}^{i+1} + \gamma \boldsymbol{v}^i \tag{2.23}$$

where $\gamma = \frac{(\boldsymbol{u}^{i+1} - \boldsymbol{u}^i) \cdot \boldsymbol{u}^i}{\boldsymbol{u}^i \cdot \boldsymbol{u}^i + \left| \boldsymbol{u}^{i+1} \cdot \boldsymbol{v}^i \right|}$.

Step 6. If $\nabla \ (\boldsymbol{\lambda})$ is less than a specified tolerance, stop. Otherwise put i=i+1 and return to step 3.

Brent's method of line searching is used for Step 3 by first bracketing the minima along the line between the end points. In Step 3, a maximum step size

d should be chosen depending on the specific problem that is solved. Since a stabilized version of the conjugate gradient method is used in Step 5, the subsequent conjugate directions depend on the previous directions.

2.4.3 Transforming the random variables

As discussed previously, a collocation method is used for solving the stochastic partial differential equation representing the evolution of texture (see also Section 3.4). In this method, a unit hypercube $[0,1]^{n_d}$ represents the stochastic space where $n_d = N + n_L$ is the dimension of the stochastic domain, N is the number of random variables in Karhunen-Loève expansion approximating the initial texture and n_L is the number of additional input uncertainties representing the process variability. This space is sampled using an adaptive sparse grid to compute the stochastic interpolant of the ODF. Each point in this sparse grid corresponds to a specific realization of the random variables under study and the corresponding ODF is computed using the deterministic analysis of Section 3.2. However, the support of our random variables as discussed in the previous section defines a convex set that needs to be mapped to this hypercube $[0,1]^{n_d}$. Thus, a transformation is needed to obtain the actual random variables from the coordinates of the sparse grid points from the hypercube. This subsection provides one such transformation.

Since the joint probability density obtained from this method is absolutely continuous on the domain of definition, the Rosenblatt [57] transformation can be used to relate the n_d variate distribution function $P_{\boldsymbol{Y}}$ to that of $\xi_1, \ldots, \xi_{n_d}$ which are independent identically distributed (iid) uniform random variables

on the hypercube $[0,1]^{n_d}$.

$$\begin{aligned} Y_1 &= {P_1}^{-1}(P_{\xi_1}(\xi_1)), \\ Y_2 &= {P_{2|1}}^{-1}(P_{\xi_2}(\xi_2)), \\ &\vdots \\ Y_{n_d} &= {P_{n_d|1:(n_d-1)}}^{-1}(P_{\xi_{n_d}}(\xi_{n_d})) \end{aligned} \tag{2.24}$$

where $P_{i|1:(i-1)}, i = 1, \ldots, n_d$, is the distribution function of Y_i conditioned on $\boldsymbol{Y}_1 = Y_1, \boldsymbol{Y}_2 = Y_2, \ldots, \boldsymbol{Y}_{i-1} = Y_{i-1}$ obtained from $P_{\boldsymbol{Y}}$. It can be shown that the random variables obtained by Eq. (3.14) are statistically independent [57]. This would help in seamlessly incorporating the collocation strategy described in the next section to solve the stochastic partial differential equation for the evolution of the random texture.

2.5 Sparse grid interpolation: Modeling the effects of random processing and initial texture

For obtaining the macro-scale properties one needs the underlying texture. This section provides a summary of the algorithm used in obtaining the effect of uncertainty on texture evolution. An adaptive sparse grid collocation strategy for constructing the stochastic solution is used. A summary of the adaptive sparse grid collocation strategy is described here. The interested reader is referred to [31, 32, 58].

The basic idea of the stochastic collocation method is to approximate the

stochastic space using multi-dimensional interpolating functions. The method uses realizations of the function (i.e. the solution $\hat{A}_f(s,t,\boldsymbol{\xi}_i)$ of the SPDE Eq. (2.6), at a finite set of collocation points $\{\boldsymbol{\xi}_i\}_{i=1}^{n_m}$, where the evolved texture is shown by $\hat{A}_f$ and n_m is the number of collocation points). These finite number of deterministic solutions are used in constructing an interpolant of the ODF using hierarchical linear interpolating basis functions [31]. The two key issues to be resolved are (a) Find the optimal points to sample this multi-dimensional space, and (b) The mathematical framework to construct the adaptive multi-dimensional interpolation once the sampling is performed. The choice of the optimal interpolating sampling is a well studied problem [59]. To have a general framework the collocation points (ξ_j^i) are selected from the hypercube $\Gamma = [0,1]^{n_d}$ where n_d is the number of stochastic dimensions. Here the superscript i stands for stochastic dimensions and the subscript j indexes the collocation points. These collocation points need to be mapped to the space of random variables before constructing the interpolants (Eq. 3.14). For a one-dimensional function, Clenshaw-Curtis points at the non-equidistant extrema of the Chebyshev polynomials [29, 60] as well as the Newton-Cotes formulae using equidistant support nodes have been shown to be optimal [31]. It is usually advantageous to choose the collocation points in a nested fashion to obtain many recurring points with increasing order of interpolation [31]. Having chosen the optimal set of points in one dimension, one can construct the interpolant approximation to a one-dimensional function f as:

$$A^i(f) = \sum_{j=1}^{m_i} f(\xi_j^i).a_j^i \tag{2.25}$$

with the set of support nodes $X^i = \{\xi_j^i | \xi_j^i \in [0,1] \quad for \quad j = 1,2,...,m_i\}$, where

$i \in \mathbb{N}$,$a_j^i \equiv a_j(\xi_j^i) \in C([0,1])$ are the interpolation nodal basis functions, and m_i is the number of elements of the set X^i. The nodal basis functions are usually Lagrange polynomials [30, 32]. The multi-dimensional interpolation function can then be constructed by using full-tensor product of the corresponding 1D interpolation rule.

$$(A^{i_1} \otimes ... \otimes A^{i_N})(f) = \sum_{j_1=1}^{m_1} ... \sum_{j_N=1}^{m_N} f(\xi_{j_1}^{i_1}, ..., \xi_{j_N}^{i_N}).(a_{j_1}^{i_1} \otimes ... \otimes a_{j_N}^{i_N}). \tag{2.26}$$

The number of support points grows very quickly as the number of stochastic dimensions increases in the full tensor product case. This led to the development of the sparse grid interpolation method which is based on the Smolyak algorithm [61].

2.6 Sparse grid interpolation

Using the Smolyak algorithm [61], univariate interpolation formulae are extended to the multivariate case by using tensor products in a special way providing an interpolation strategy with potentially orders of magnitude reduction in the number of support nodes required. The Smolyak algorithm uses products of 1D functions to construct the sparse interpolant $L_{q,N}$, where N is the number of stochastic dimensions and $q - N$ is the order of interpolation.

Consider the incremental interpolant, Δ^{i_1} given by [31, 32]

$$A^0 = 0; \quad \Delta^{i_1} = {A_1}^i - {A_1}^{i-1} \tag{2.27}$$

The Smolyak interpolation $L_{q,N}$ is then given by

$$\begin{aligned} L_{q,N}(f) &= \sum_{|i|\leq q}(\Delta^{i_1}\otimes ...\otimes \Delta^{i_N})(f) = L_{q-1,N}(f) \\ &+ \sum_{|i|=q}(\Delta^{i_1}\otimes ...\otimes \Delta^{i_N})(f) = L_{q-1,N}(f) + \Delta L_{q,N}(f) \end{aligned} \tag{2.28}$$

with $q \geq N, L_{N-1,N} = 0$ and where the multi-index $\boldsymbol{i} = (i_1, ..., i_N) \in \mathbb{N}^N$ and $|\boldsymbol{i}| = i_1 + ... + i_N$. Here $i_k, k = 1, ..., N$, can be thought of as the level of interpolation along the $k - th$ direction. The Smolyak algorithm essentially builds the interpolation function by adding a combination of 1D functions of order i_k with the constraint that the sum total ($|\boldsymbol{i}| = i_1 + ... + i_N$) across all dimensions is less than q. The construction of the algorithm allows one to utilize all the previous results generated to improve the interpolation (this is immediately obvious from Eq. (2.29). By choosing appropriate points for interpolating the 1D function, one can ensure that the sets of points X^i are nested ($X^i \subset X^{i+1}$).

Newton-Cotes grid using equidistant support nodes has been used for implementing the adaptivity [31]. By using equidistant nodes, it is easy to refine the grid locally. Furthermore, by using the linear hat function as the univariate nodal basis function [62] one ensures a local support in contrast to the global support of using Lagrange polynomial (Eq. 2.25). This ensures that discontinuities in the stochastic space can be resolved.

2.7 From nodal basis to hierarchical basis

In order to benefit from adaptivity in refining the sparse grid collocation points one needs to move from a nodal basis definition of the interpolation formulae to

a hierarchical basis definition of the interpolation functions [31]. For deriving the hierarchical basis functions from that of the nodal basis as explained in the previous section, one can use Eq. (2.27) to write $\Delta^{i_1}(f) = {A_1}^i(f) - {A_1}^{i-1}(f)$, with ${A_1}^i(f) = \sum_{\xi_j^i \in X^i} a_j^i \ . \ f(\xi_j^i)$, and ${A_1}^{i-1}(f) = {A_1}^i({A_1}^{i-1}(f))$, which can be written as [31]

$$\begin{aligned} \Delta^{i_1}(f) &= \sum_{\xi_j^i \in X^i} a_j^i.f(\xi_j^i) - \sum_{\xi_j^i \in X^i} a_j^i.{A_1}^{i-1}(f)(\xi_j^i) \\ &= \sum_{\xi_j^i \in X^i} a_j^i.(f(\xi_j^i) - {A_1}^{i-1}(f)(\xi_j^i) \end{aligned} \tag{2.29}$$

and, since $f(\xi_j^i) - {A_1}^{i-1}(f)(\xi_j^i) = 0, \forall \xi_j^i \in X^{i-1}$, one can write

$$\Delta^i(f) = \sum_{\xi_j^i \in X_\Delta^i} a_j^i.(f(\xi_j^i) - {A_1}^{i-1}(f)(\xi_j^i) \tag{2.30}$$

where $X_\Delta^i = X^i \ X^{i-1}$. Clearly, X_Δ^i has $m_\Delta^i = m_i - m_{i-1}$ points, since $X_{i-1} \subset X_i$. The above equation is written as [31]

$$\Delta^{i_1}(f) = \sum_{j=1}^{m_\Delta^i} a_j^i.(f(\xi_j^i) - {A_1}^{i-1}(f)(\xi_j^i) = \sum_{j=1}^{m_\Delta^i} a_j^i.\theta_j^i \tag{2.31}$$

where θ_j^i is the 1D hierarchical surplus, which is just the difference between the function value at the current level and the previous level and a_j^i is the set of functions defined as the hierarchical basis functions. Having the 1D formula in Eq. (2.31) one can obtain the sparse grid interpolation formula for the multivariate case. This formula is written in a hierarchical form as:

$$\begin{aligned}\Delta L_{q,N}(f) &= \sum_{|i|=q}\sum_{j\in B_i}(a_{j_1}^{i_1}\otimes ...\otimes a_{j_N}^{i_N} \\ &\cdot \quad (f(\xi_{j_1}^{i_1},...,\xi_{j_N}^{i_N}) - L_{q-1,N}(f)(\xi_{j_1}^{i_1},...,\xi_{j_N}^{i_N}))\end{aligned} \tag{2.32}$$

where the multi-index set $B_i := \{j \in \mathbb{N}^N : \xi_{j_k}^{i_k} \in X_\Delta^{i_k} \quad for \quad j_k = 1,...,m_\Delta^{i_k}, k = 1,...,N\}$ and one can define

$$\theta_j^i = f(\xi_{j_1}^{i_1},...,\xi_{j_N}^{i_N}) - L_{|i|-1,N}(f)(\xi_{j_1}^{i_1},...,\xi_{j_N}^{i_N}) \tag{2.33}$$

as the hierarchical surplus, which is just the difference between the function value at the current point and interpolation value from the coarser grid. As described in [31], one can work either in the nodal basis functional space or the hierarchical basis space. For smooth functions, the hierarchical surpluses tend to zero as the interpolation level tends to infinity. On the other hand, for non-smooth functions, steep gradients/finite discontinuities are indicated by the magnitude of the hierarchical surplus. The bigger the magnitude is, the stronger the underlying discontinuity is. Therefore, the hierarchical surplus is a natural candidate for error control and implementation of adaptivity.

2.7.1 Adaptive sparse grid interpolation

More details on constructing the sparse grid interpolation is provided in this section [31]. The 1D equidistant points of the sparse grid can be considered as a tree-like data structure. One can consider the interpolation level of a grid point $\boldsymbol{\xi}$ as the depth of the tree $D(\boldsymbol{\xi})$. Denote the father of a grid point as $F(\boldsymbol{\xi})$, where

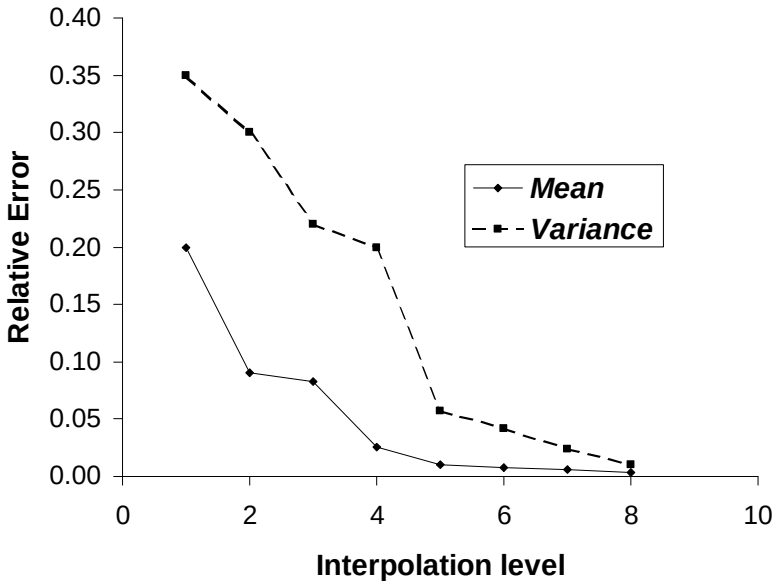

Figure 2.3: Convergence of mean and variance of young modulus with respect to the interpolation level for the sparse grid method. The relative error is calculated with respect to the result of MC simulation.

the father of the root 0.5 is itself, i.e., F(0.5) = 0.5. The conventional sparse grid in the N-dimensional space can be reconsidered as

$$H_{q,N} = \{\boldsymbol{\xi} = \xi_1, ..., \xi_N | \sum_{i=1}^{N} D(\xi_i) \leq q\} \tag{2.34}$$

where the sons of a grid point $\boldsymbol{\xi} = (\xi_1, ..., \xi_N)$ are denoted by

$$Sons(\boldsymbol{\xi}) = \{\boldsymbol{S} = (S_1, S_2, ..., S_N) | (F(S_1), S_2, ..., S_N) = \boldsymbol{\xi}\} \tag{2.35}$$

From this definition, it is noted that, in general, for each grid point there are two sons in each dimension, therefore, for a grid point in a N-dimensional stochastic space, there are 2N sons. It is also noted that, the sons are also the

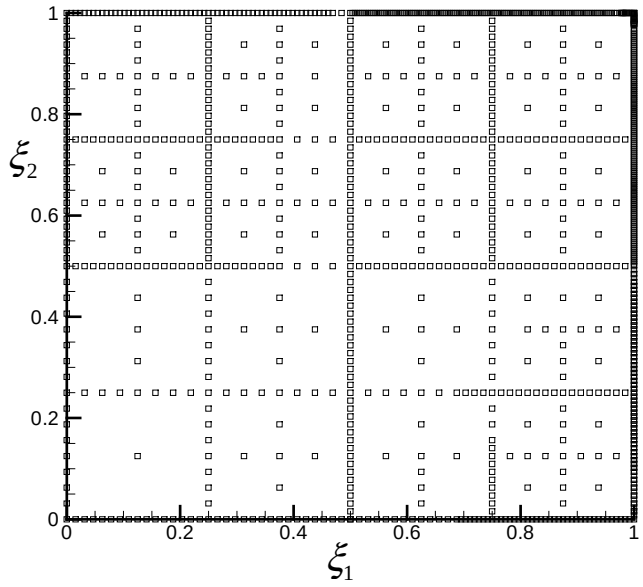

Figure 2.4: Collocation points for the adaptive sparse grid method.

neighbor points of the father. The neighbor points are just the support nodes of the hierarchical basis functions in the next interpolation level [31]. By adding the neighbor points, one actually adds the support nodes from the next interpolation level, i.e., one performs interpolation from level $|i|$ to level $|i| + 1$. Therefore, in this way, the grid is locally refined while not violating the developments of the Smolyak algorithm (Eq. 2.32).

The basic idea here is to use hierarchical surpluses as an error indicator to detect the smoothness of the solution and refine the hierarchical basis functions a_j^i whose magnitude of the hierarchical surplus satisfies $|\theta_j^i| \geq \varepsilon$. If this criterion is satisfied, one simply adds the 2N neighbor points of the current point from Eq. 2.35 to the sparse grid. It is noted that the growth of the points scales linearly with increasing dimensionality rather than the $O(2^N)$ tree-like scaling of the standard h-type adaptive refinement as in a random element-based framework, e.g. ME-gPC. Let $\varepsilon > 0$ be the parameter for the adaptive refinement threshold. The following iterative refinement algorithm can be used beginning with

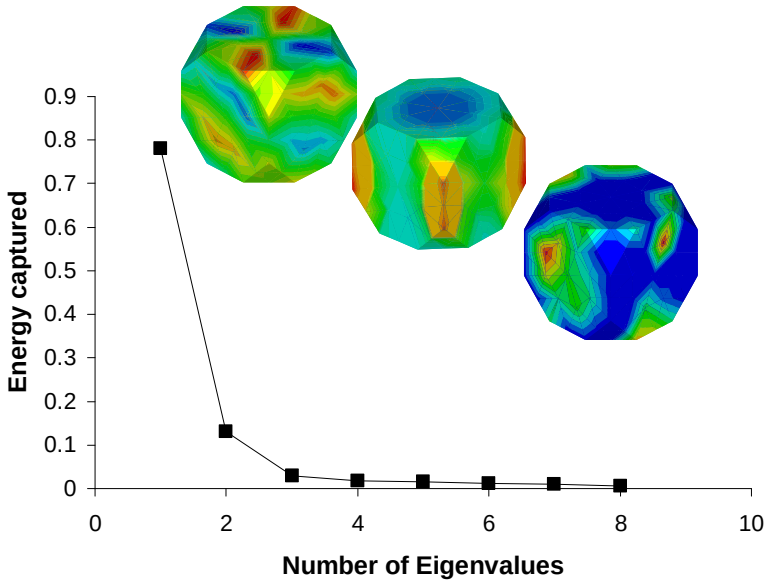

Figure 2.5: The most significant eigenvalues for the snapshots of the initial texture and the corresponding eigenvectors for the first three significant eigenvalues.

a coarsest adaptive sparse grid $G_{N,N}$, i.e., one begins with the N-dimensional multi-index $\boldsymbol{i} = (1, ..., 1)$, which is just a point (0.5, ... , 0.5).

(1) Set level of Smolyak construction $k = 0$.

(2) Construct the first level adaptive sparse grid $G_{N,N}$.

- Calculate the function value at the point (0.5, . . . , 0.5);

- Generate the 2N neighbor points and add them to the active index set;

- Set k = k + 1.

(3) While $k \leq k_{max}$ and the active index set is not empty:

- Copy the points in the active index set to an old index set and clear the active index set.

- Calculate in parallel the hierarchical surplus of each point in the old index set according to

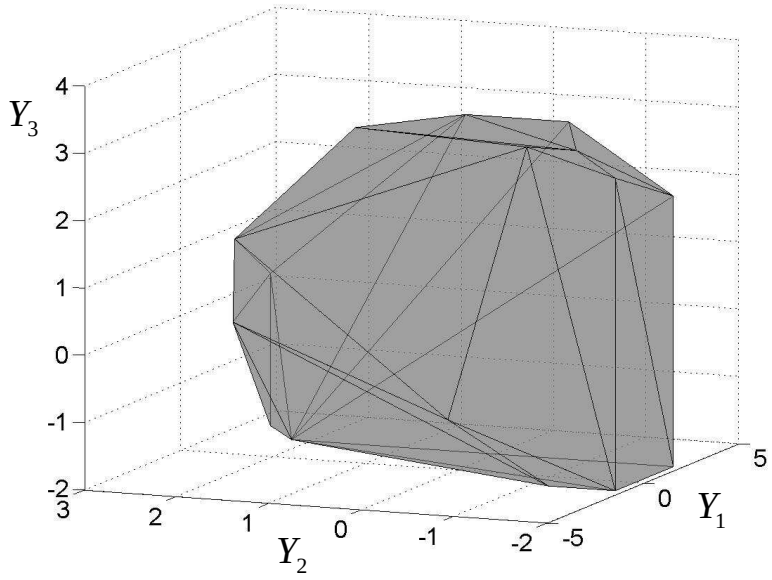

Figure 2.6: Convex hull of the random variables Y_1, Y_2, Y_3 obtained by enforcing the positiveness of the ODF.

$$\theta_j^i = f(\xi_{j_1}^{i_1}, ..., \xi_{j_N}^{i_N}) - G_{N+k-1,N}(f)(\xi_{j_1}^{i_1}, ..., \xi_{j_N}^{i_N}) \tag{2.36}$$

Here, all of the existing collocation points are used in the current adaptive sparse grid $G_{N+k-1,N}$. This allows one to evaluate the surplus for each point from the old index set in parallel.

- For each point in the old index set, if $|\theta_j^i \geq \varepsilon|$

. Generate 2N neighbor points of the current active point according to Eq. 2.35;

. Add them to the active index set.

- Add the points in the old index set to the existing adaptive sparse grid $G_{N+k-1,N}$. Now the adaptive sparse grid becomes $G_{N+k,N}$.

- $k = k + 1$

(4) Calculate the mean and the variance, the PDF and if needed realizations of

the solution.

So, The function $\hat{A}_f(s,t,\boldsymbol{\xi})$ can for example be approximated by the following:

$$\hat{A}_f(s,t,\boldsymbol{\xi}_i) = \sum_{|i|\leq q} \sum_{j} \theta_j^i(s).a_j^i(\boldsymbol{\xi}) \tag{2.37}$$

$$\hat{A}_f{}^2(s,t,\boldsymbol{\xi}_i) = \sum_{|i|\leq q} \sum_{j} \grave{\theta}_j^i(s).a_j^i(\boldsymbol{\xi}) \tag{2.38}$$

This is just a simple weighted sum of the value of the basis functions for all collocation points in the current sparse grid where $a_j^i \equiv a_j(\xi_j^i)$ are the n_d dimensional multilinear basis functions constructed from their corresponding 1-dimensional ones using tensor products, θ_j^i are the difference between the value of interpolant in current and previous interpolation level, $\grave{\theta}_j^i$ are as θ_j^i but for the second power of the interpolant, $q - n_d$ is the order of interpolation, n_d is the number of stochastic dimensions and the summation is over the collocation points selected in a hierarchical framework [31].

After obtaining the expression in Eq. (3.15), it is also easy to extract statistics [31]. The mean of the random solution can be evaluated as follows:

$$E[\hat{A}_f(s,t,\boldsymbol{\xi})] = \sum_{|i|\leq q} \sum_{j} \theta_j^i(s). \int_{\Gamma} a_j^i(\boldsymbol{\xi}) d\boldsymbol{\xi} \tag{2.39}$$

where the probability density function $p(\boldsymbol{\xi})$ is 1 since the stochastic space is a unit hypercube $[0,1]^{n_d}$. As shown in [31], the multi-dimensional integral

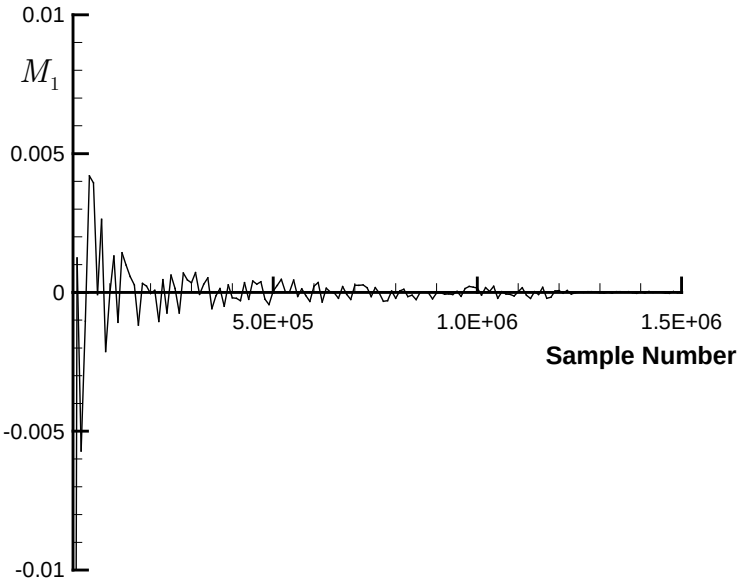

Figure 2.7: The value of the integral M_1 used as a constraint ($M_1 \equiv E(Y_1) = 0.0$) evaluated by MC for the final step of MaxEnt problem.

is simply the product of the 1D integrals which can be computed analytically. Denoting $\int_\Gamma a_j^i(\boldsymbol{\xi})d\boldsymbol{\xi} = I_j^i$ one can rewrite Eq. (3.17) as

$$E[\hat{A}_f(s,t,\boldsymbol{\xi})] = \sum_{|i|\leq q}\sum_j \theta_j^i(s).I_j^i \tag{2.40}$$

The second order moment can be calculated from

$$E[\hat{A_f}^2(s,t,\boldsymbol{\xi})] = \sum_{|i|\leq q}\sum_j \hat{\theta_j^i}(s).I_j^i \tag{2.41}$$

Similarly, higher-order statistics can be calculated. As mentioned before,in constructing the interpolant that approximates the texture $\hat{A}_f(s,t,\boldsymbol{\xi})$ in the stochastic domain, one ends up with the realizations of $\hat{A}_f(s,t,\boldsymbol{\xi})$. These realizations are calculated at some collocation points representing specific realizations of the random variables. The realizations of the evolved (final) texture

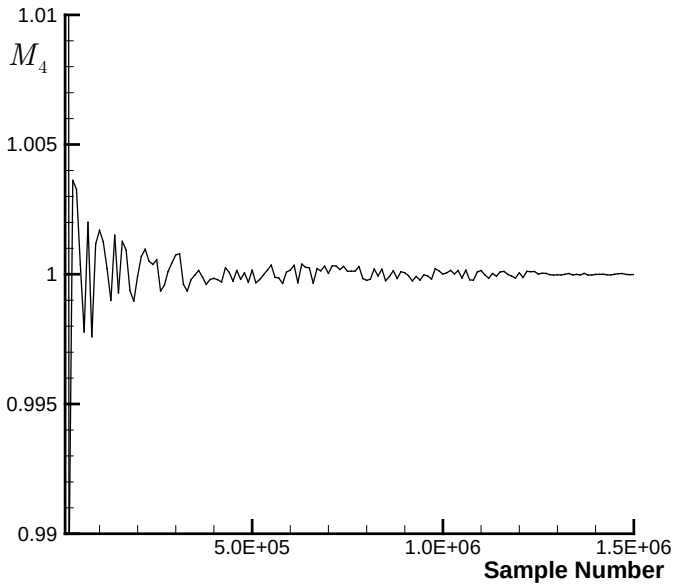

Figure 2.8: The value of the integral M_4 used as a constraint ($M_4 \equiv E(Y_1^2) = 1.0$) evaluated by MC for the final step of MaxEnt problem.

$\hat{A}_f(s,t,\boldsymbol{\xi})$ are from an underlying random field representing the final texture $\hat{\boldsymbol{A}}_f$. It should be noticed that since the initial texture has been evolved using the Eq. (2.6) the random field representing the final texture $\hat{\boldsymbol{A}}_f$ is different from that of initial texture. The realizations of $\hat{\boldsymbol{A}}_f$ can be obtained from the collection of the realizations obtained at collocation points and the ones obtained from the constructed interpolant using Eq. (3.15). In order to obtain the convex hull of material properties (see next section) the reduced order model of $\hat{\boldsymbol{A}}_f$ is constructed using Karhunen-Loève expansion. This would in turn translate into another eigenvalue problem (Eq. (2.9)). It should be noticed that the interpolant is constructed using hierarchical linear interpolating basis functions with local support. These interpolation functions with their local support construct the interpolation from the space of initial random variables but due to their local support they are unable of providing a reduced order model for the final texture ($\hat{A}_f(s,t,\boldsymbol{\xi})$). The realizations of the uncorrelated random variables used in

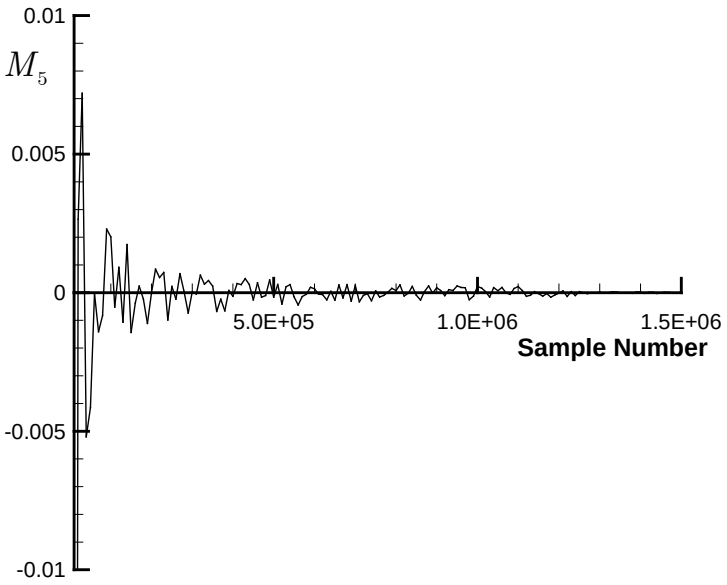

Figure 2.9: The value of the integral M_5 used as a constraint ($M_5 \equiv E(Y_1 Y_2) = 0.0$) evaluated by MC for the final step of MaxEnt problem.

KLE can be obtained using Eq. (2.11). This leads to a convex hull for these random variables Y_{f_i} that is different from that obtained for the initial texture. The subscript f is used here to differentiate these from the random variables representing the initial texture. The following section discusses an algorithm that computes the convex hull of material properties from all viable values of Y_f.

2.8 Convex hull of material properties

Property closures represent complete range of properties obtainable from the space of ODFs. These are approximated by the space between upper and lower bounds of the given property. The problem of obtaining the maximal properties from the space of ODFs can be posed as an optimization problem.

Let $v_1, \ldots, v_k$ be the set of properties for which the closure is required.

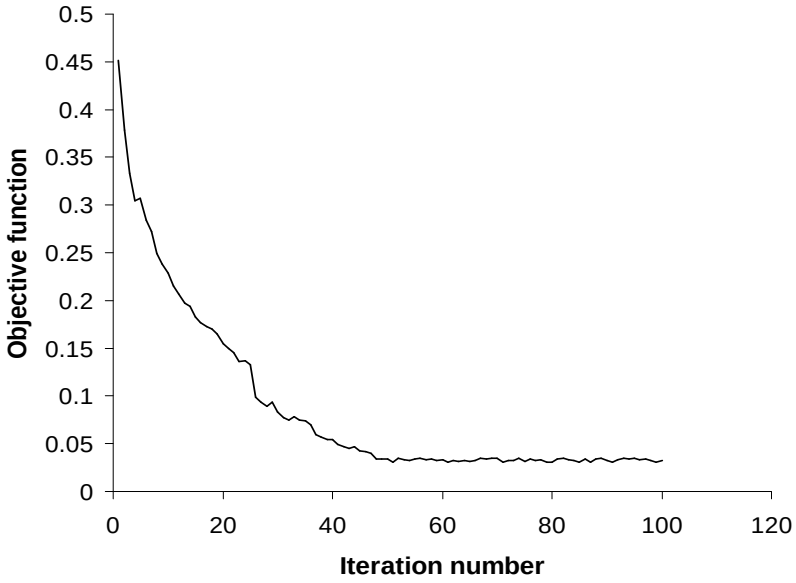

Figure 2.10: Objective function with respect to iteration number for the constrained optimization problem posed by the MaxEnt principle.

The closure for property v_1 is first found by obtaining the extremal values (v_{1max}, v_{1min}). Then, property v_1 is discretized into m values $v_1^i, i = 1, \ldots, m$ between v_{1max} and v_{1min}. The property closure of the combined set of properties (v_1, v_2) is found by executing a similar extremum problem at each point v_1^i with the additional constraint that $p_1^T \hat{\boldsymbol{A}}_f = v_1^i$ where p is defined in the following lines. In general, the closure for a combined set of k properties $(v_1, v_2, \ldots, v_k)$ is a k-dimensional volume found by applying this algorithm on v_k at a set of discrete points $(v_1^i, v_2^j, .., v_{k-1}^l)$ in the closure area of $(v_1, v_2, \ldots, v_{k-1})$. The corresponding problem for minimizing v_k is written in the discretized format as:

$$\begin{aligned} \min_{\hat{\boldsymbol{A}}_f} v_k &= \frac{\boldsymbol{p}_k^T . \hat{\boldsymbol{A}}_f}{\boldsymbol{q}^T . \hat{\boldsymbol{A}}_f} \\ \hat{\boldsymbol{A}}_f &\geq 0 \end{aligned} \tag{2.42}$$

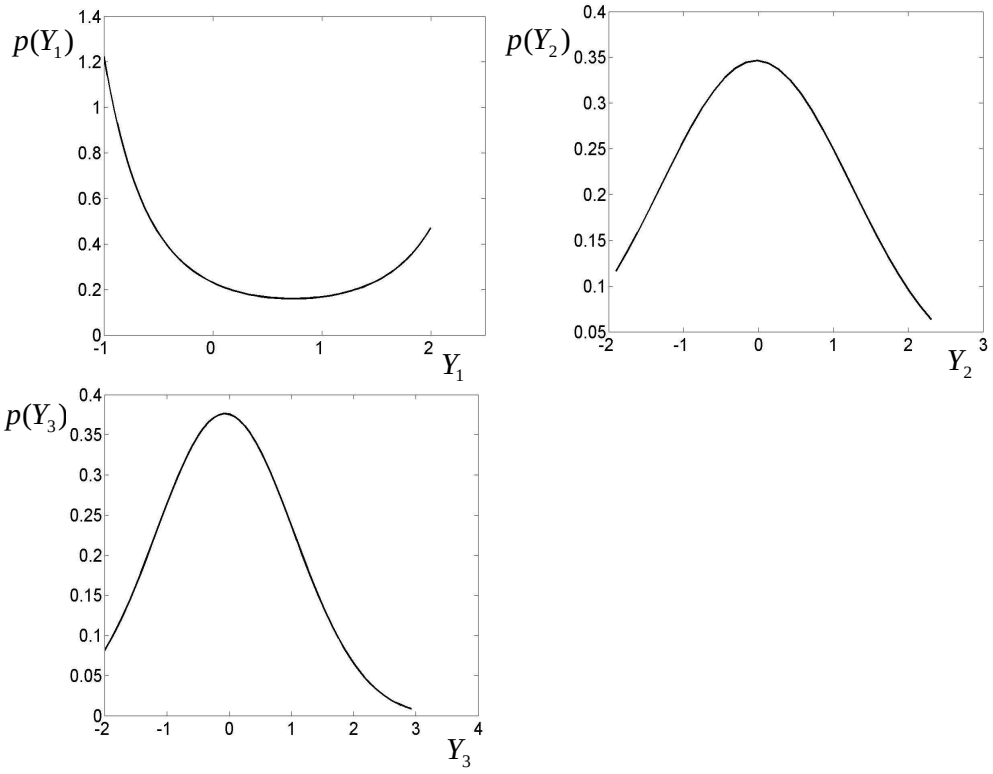

Figure 2.11: Marginal probability distribution for the random variables Y_1, Y_2, Y_3

$$\frac{\boldsymbol{p}_m^T.\hat{\boldsymbol{A}}_f}{\boldsymbol{q}^T.\hat{\boldsymbol{A}}_f} = v_m^i, \quad m = 1 : k-1$$

where $\boldsymbol{p}_k$ and $\boldsymbol{q}$ are vectors defined in the following lines. To maximize v_k another similar problem is executed where the objective is changed as $\min_{\hat{\boldsymbol{A}}_f} v_k = -\frac{\boldsymbol{p}_k^T.\hat{\boldsymbol{A}}_f}{\boldsymbol{q}^T.\hat{\boldsymbol{A}}_f}$. The positiveness of $\hat{\boldsymbol{A}}_f$ is enforced as a constraint in Eq. (2.42). $\boldsymbol{p}$ and $\boldsymbol{q}$ are defined as follows. Rewriting Eq. (2.4) in discretized format, one obtains [23]

$$\begin{aligned} \langle X_j \rangle &= (\sum_{n=1}^{nel}\sum_{m=1}^{nint} X_j(s_m)\hat{A}_f(s_m)\hat{\eta}_m|J_n|\frac{1}{(1+s_m.s_m)^2}) \\ &/ \quad (\sum_{n=1}^{nel}\sum_{m=1}^{nint} \hat{A}_f(s_m)\hat{\eta}_m|J_n|\frac{1}{(1+s_m.s_m)^2}) = \frac{\boldsymbol{p}_j^T.\hat{\boldsymbol{A}}_f}{\boldsymbol{q}^T.\hat{\boldsymbol{A}}_f} \end{aligned} \tag{2.43}$$

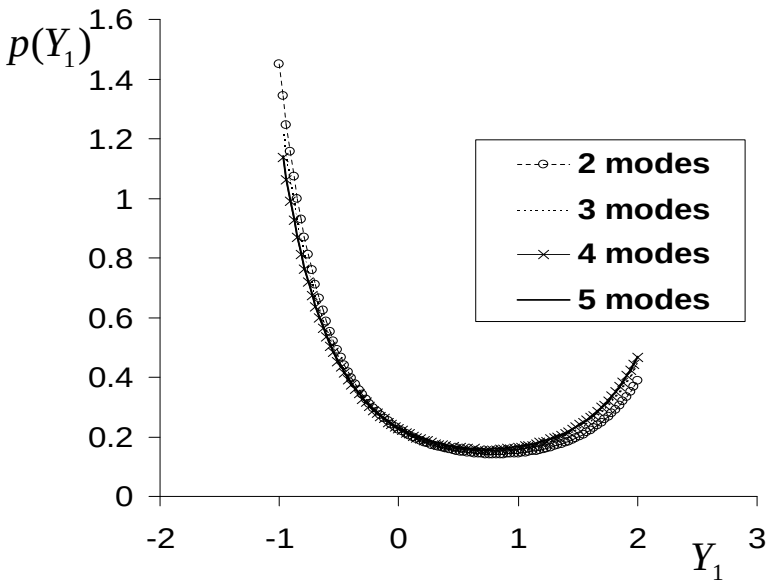

Figure 2.12: Convergence of the marginal probability distribution of Y_1 with respect to the number of modes in KLE expansion.

where $p_j^i = X_j(s_i)\hat{\eta}_i|J_i|\frac{1}{(1+s_i.s_i)^2}$ and $q^i = \hat{\eta}_i|J_i|\frac{1}{(1+s_i.s_i)^2}$ in which index i represents each integration point on the finite element mesh of the fundamental region, $|J_i|$ is the jacobian determinant of the element that the integration point belongs to, $\hat{\eta}_i$ is the integration weight associated with the integration point and s_m is the global coordinate of the integration point. $X_j(s_m)$ corresponds to a property related to a specific crystal orientation defined by point s_m in Rodrigues space and X_i is the property under study. In this work, we select $X_1(s_m) := B(s_m), X_2(s_m) := G(s_m), X_3(s_m) := E(s_m)$, where B, G and E are the bulk modulus, shear modulus and Young's modulus, respectively.

To find the effect of a deformation process on macro-scale properties, the reduced-order representation (Karhunen-Loève expansion) of the texture obtained at the end of the process is used. Once this expansion is constructed, its output is a realization of what can be obtained as the final texture at the end of the deformation process. Hence, replacing $\hat{\boldsymbol{A}}_f$ in the optimization prob-

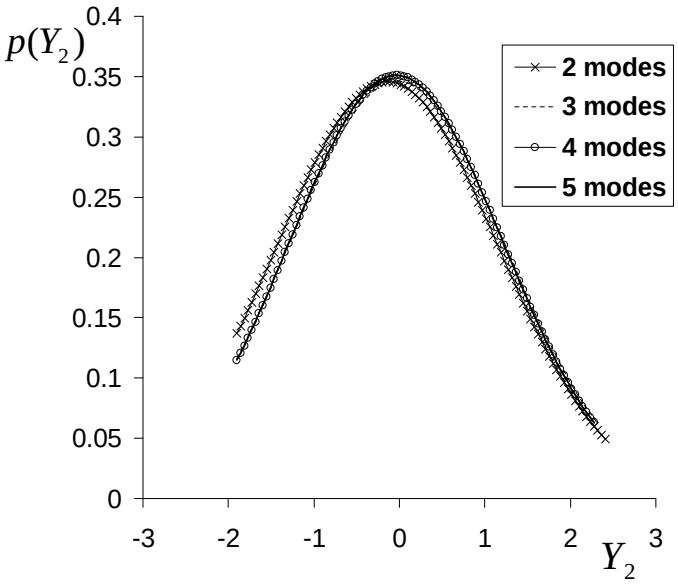

Figure 2.13: Convergence of the marginal probability distribution of Y_2 with respect to the number of modes in KLE expansion.

lem posed in Eq. (2.42) by its reduced representation $\hat{\boldsymbol{A}}_f(\boldsymbol{Y_f})$ (where Y_{f_i} are the coefficients used in the reduced-order representation), guarantees the resultant solution to be a texture obtainable from the processes under study.

Writing Eq. (2.9) as: $\hat{\boldsymbol{A}}_f = \overline{\boldsymbol{A}}_f + \boldsymbol{B}\boldsymbol{Y}_f$, one can rewrite Eq. (2.42) as

$$\begin{aligned} \min_{\boldsymbol{Y}_f \in D'} \; & \frac{\boldsymbol{p}_k^T.\overline{\boldsymbol{A}}_f + \widetilde{\boldsymbol{p}}_k^T.\boldsymbol{Y}_f}{\boldsymbol{q}^T.\overline{\boldsymbol{A}}_f + \widetilde{\boldsymbol{q}}^T.\boldsymbol{Y}_f} \\ & \frac{\boldsymbol{p}_m^T.\overline{\boldsymbol{A}}_f + \widetilde{\boldsymbol{p}}_m^T.\boldsymbol{Y}_f}{\boldsymbol{q}^T.\overline{\boldsymbol{A}}_f + \widetilde{\boldsymbol{q}}^T.\boldsymbol{Y}_f} \;\; = \;\; v_m^i, \quad m = 1:k-1 \end{aligned} \tag{2.44}$$

where $\widetilde{\boldsymbol{p}}_k^T = \boldsymbol{p}_k^T.\boldsymbol{B}$, $\widetilde{\boldsymbol{q}}^T = \boldsymbol{q}^T.\boldsymbol{B}$ and D' is the convex hull of $\boldsymbol{Y}_f$ which guarantees the positiveness of $\hat{\boldsymbol{A}}_f$.

In [23], the denominators presented in Eq. (2.44) are replaced by a constraint of the format $\boldsymbol{q}^T.\hat{\boldsymbol{A}}_f(\boldsymbol{Y}_f) = 1$. This simplification is avoided in here. Including

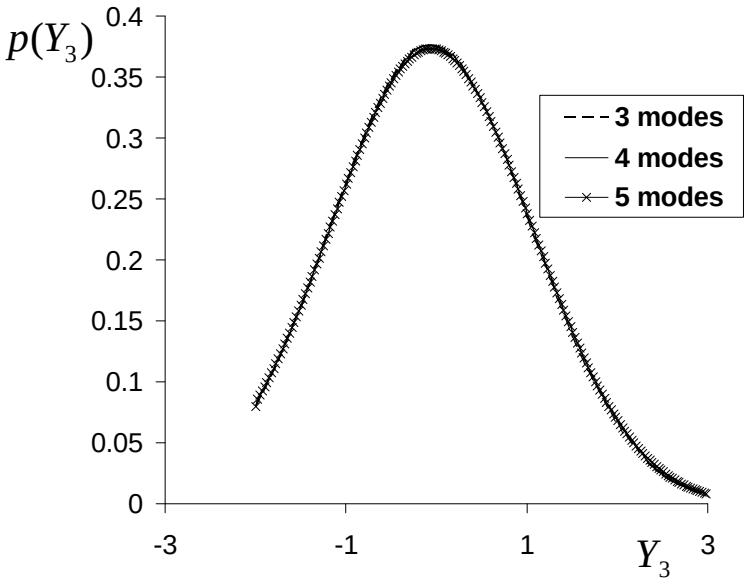

Figure 2.14: Convergence of the marginal probability distribution of Y_3 with respect to the number of modes in KLE expansion.

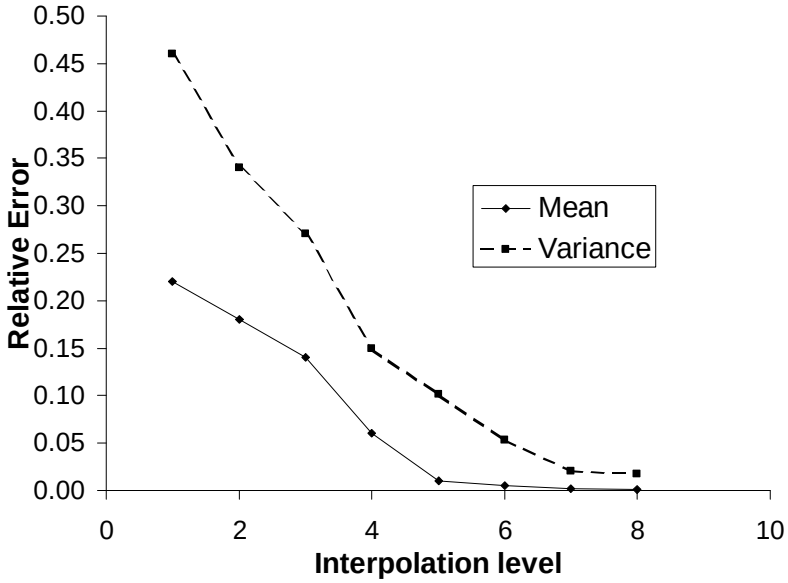

Figure 2.15: Convergence of mean and variance of young modulus with respect to the interpolation level for the sparse grid method. The relative error is calculated with respect to the result of MC simulation.

this assumption as a constraint in Eq. (2.44) would have forced the random variables $Y_{f_1}, \ldots, Y_{f_n}$ to be on a specific hyperplane in the convex hull. This method

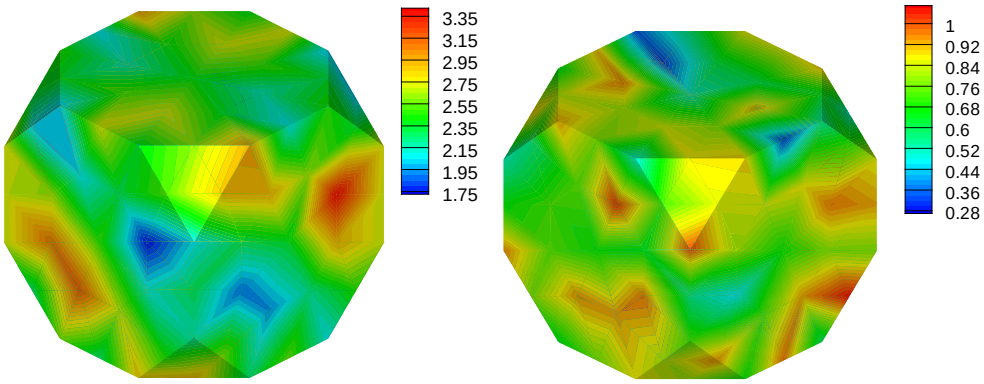

Figure 2.16: Mean (left) and variance (right) of the final texture.

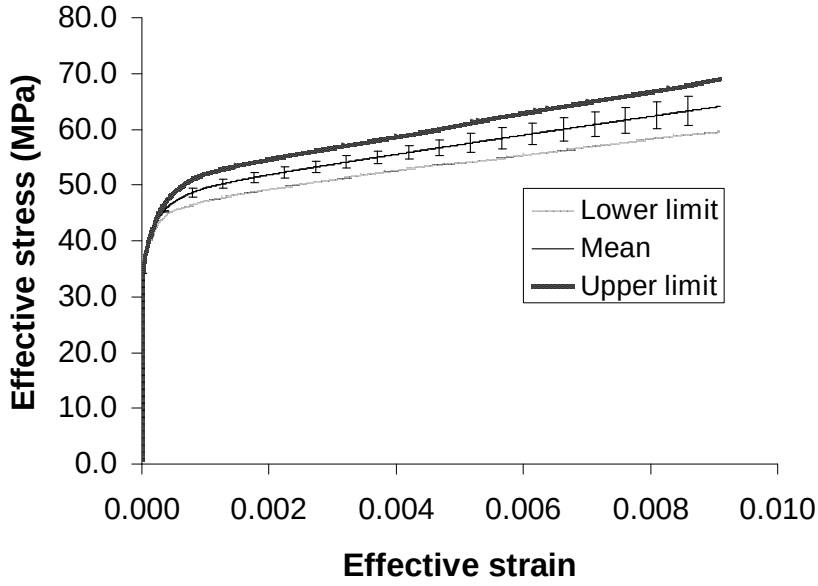

Figure 2.17: Variation in stress-strain response due to the effect of uncertainty in initial texture.

would not only ignore the convex hull but also violate the assumption in the KLE method that the random variables be uncorrelated.

Eq. (2.44) in its current format is not amenable to linear programming since neither the objective function nor the constraints are linear functions of $\boldsymbol{Y}_f$. In order to use the properties of a linear optimization problem, Eq. (2.44) can be transformed to a set of linear optimization problems as follows

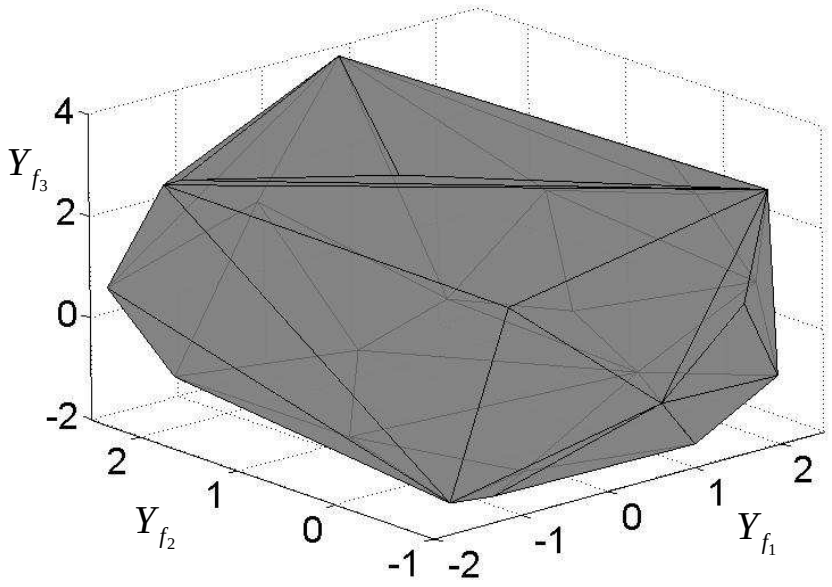

Figure 2.18: Convex hull of Y_{f1}, Y_{f2}, Y_{f3} obtained as a set of $Y_{fi}; i = 1 : 3$ that guarantees the positiveness of the result of KL expansion representing the final texture.

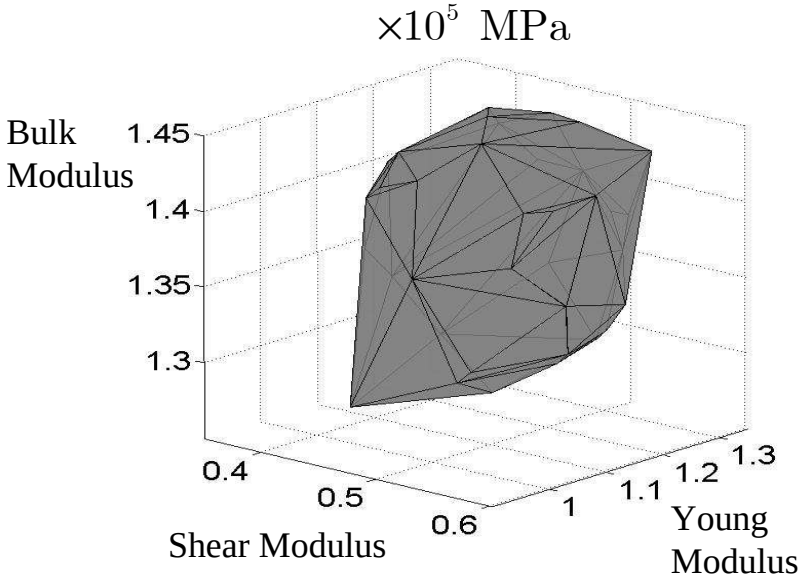

Figure 2.19: Convex hull of macro-scale properties.

$$\min_{\boldsymbol{Y}_f \in D'} \widetilde{\boldsymbol{p}}_k^T . \boldsymbol{Y}_f \tag{2.45}$$

$$
\begin{aligned}
\boldsymbol{q}^T.\overline{\boldsymbol{A}}_f + \widetilde{\boldsymbol{q}}^T.\boldsymbol{Y}_f &= c_i \\
\boldsymbol{p}_m^T.\overline{\boldsymbol{A}}_f + \widetilde{\boldsymbol{p}}_m^T.\boldsymbol{Y}_f &= v_m^i, \quad m = 1 : min(k-1, n_d - 1)
\end{aligned}
$$

where the extra bound on the range of m is due to geometric constraints. The closure for a combined set of k properties is a k dimensional volume. The coordinates of this k dimensional volume depend linearly on the coordinates of an n_d dimensional volume. If $k > n_d$, only n_d coordinates of the k dimensional volume are independent. For each optimization problem (i), the intersection of the convex hull of parameters Y_{f_i} and the hypersurface $\boldsymbol{q}^T.\overline{\boldsymbol{A}}_f + \widetilde{\boldsymbol{q}}^T.\boldsymbol{Y}_f - c_i = 0.0$ is used to minimize the property $\widetilde{\boldsymbol{p}}_k^T.\boldsymbol{Y}_f$. The values c_i are selected such that the resulting parallel hypersurfaces span the convex hull of variables $\boldsymbol{Y}_f$ (instead of only assuming $c_i = 1$ which would only span a subset of the convex hull). In order to obtain the range of c_i, the extremum values of $\boldsymbol{q}^T.\overline{\boldsymbol{A}}_f + \widetilde{\boldsymbol{q}}^T.\boldsymbol{Y}_f$ are evaluated. To find the minimum value for c_i, the following problem is solved $min_{\boldsymbol{Y}_f \in D'}\ (\widetilde{\boldsymbol{q}}^T.\boldsymbol{Y}_f)$. For maximizing c_i, the problem is changed to $min_{\boldsymbol{Y}_f \in D'}\ (-\widetilde{\boldsymbol{q}}^T.\boldsymbol{Y}_f)$. Since in Eq. (2.45) the objective function and the constraints are all linear functions of $\boldsymbol{Y}_f$, linear programming can be used to obtain the optimum value. In linear programming all local optima are global optima and the optimal solution occurs at a boundary point of the convex hull.

2.9 Numerical examples

2.9.1 Example1: Propagation of uncertainty on process conditions

A point simulator is examined in this problem to investigate the effects of uncertainty on the process parameters on the macro-scale properties. The goal is to find the mean and variance of the macro-scale properties at the end of a sequence of processes (higher-order statistics can be extracted as well). The material considered here is FCC copper with the following material properties.

$$c_{11} = 170.0GPa, c_{12} = 124.0GPa, c_{44} = 75.0GPa, \tag{2.46}$$

The fundamental part of the Rodrigues space is as shown in Fig. 2.2. The microstructure is considered to be subjected to a sequence of two deformation modes, namely a shear mode followed by a plain strain compression. In the first process, the microstructure is subjected to a velocity gradient given by the first term in Eq. (2.5) (parameter β_1)

$$\beta_1 \begin{pmatrix} 0 & 1 & 0 \\ 1 & 0 & 0 \\ 0 & 0 & 0 \end{pmatrix} \tag{2.47}$$

This process is followed by a second process. The final texture and the plastic part of the deformation gradient at the end of the first process are considered as

the initial conditions of the second process. The velocity gradient for the second process has the form given by the second term in Eq. (2.5) (parameter β_2).

$$\beta_2 \begin{pmatrix} 0 & 0 & 0 \\ 0 & 1 & 0 \\ 0 & 0 & -1 \end{pmatrix} \tag{2.48}$$

The parameters β_1, β_2 are considered to be two independent identically distributed uniform random variables between 0.2 and 0.5 $\frac{1}{sec}$. A level 8 interpolating adaptive sparse grid corresponding to 1008 collocation points for this particular stochastic problem has been used. The mean and variance of Young's modulus calculated at the end of the 8th level of interpolation are $1.22e05$ (MPa) and $2.64e07$ $(MPa)^2$ respectively. The same problem has been solved using Monte-Carlo (MC) method with 10000 runs. The mean and variance of Young's modulus obtained from MC are $1.22e05$ (MPa) and $2.59e07$ $(MPa)^2$ respectively. Figure 2.3 shows the convergence of mean and variance for Young's modulus for different levels of adaptive interpolation. In this figure the relative error refers to the relative error between result obtained from adaptive sparse grid and MC methods. Figure 2.4 shows the collocation points in the adaptive sparse grid method for this specific problem. The variables ξ_1 and ξ_2 shown are independent uniform random variables between 0 and 1 and are mapped to the β parameters using $\beta_i = 0.2 + 0.3\xi_i$.

2.9.2 Example 2: Quantification and propagation of uncertainty in initial texture

In this example the variation of macro-scale properties due to the uncertainty in initial texture has been investigated. We concentrate on the shear modulus and bulk modulus. The shear modulus G is a good representation of mechanical hardness of alloys in the annealed state [63, 64], whereas the bulk modulus B is a good representation of the resistance of the material to bond rupture [65].

The 1008 realizations of the final texture obtained from the collocation points in the previous example have been used to construct the unbiased estimate of the covariance matrix of the random initial texture. The numerically calculated eigenvalues of the correlation matrix are shown in Fig. 2.5. The first 3 eigenvalues correspond to $99\ \%$ of the spectrum. Hence the random process representing the initial texture for our problem can be adequately approximated by 3 random variables Y_1, Y_2, Y_3.

The convex hull of the random variables Y_1, Y_2, Y_3 that guarantees positiveness of the texture obtained from the Karhunen-Loève approximation is obtained using Eq. 2.12 and is shown in Figure 2.6.

The joint probability distribution of the uncorrelated random variables Y_1, Y_2, Y_3 from the Karhunen-Loève expansion has been obtained using the Maximum entropy (MaxEnt) principle. Figures 2.7, 2.8 and 2.9 show the values for some of the constraints (Eq.2.15) posed in the MaxEnt problem. These constraints correspond to the higher dimensional integrals (over domain D) that were defined in the MaxEnt problem. For any set of values of $\lambda_1, ..., \lambda_9$ obtained at each optimization step, these integrals need to be evaluated using MC

method. The convergence of MC method in evaluating these integrals for the optimum values of lagrange parameters obtained from the final step of the optimization problem is shown in Figures 2.7, 2.8 and 2.9. These figures also show the converged values of these integrals for the optimum values of lagrange parameters. These converged values satisfy the constraints posed in MaxEnt problem. The objective function versus iteration number for the constraint optimization problem posed by the MaxEnt principle is shown in Fig. 2.10.

The marginal probability distribution of random variables Y_1, Y_2, Y_3 is shown in Figure 2.11. Next two more significant modes (Modes 4 and 5) in Karhunen-Loève expansion are added to study the convergence of the algorithm. Convergence of the marginal probability distributions of random variables Y_1, Y_2, Y_3 with respect to the number of modes used in Karhunen-Loève expansion is shown in Figures 2.12, 2.13 and 2.14 respectively.

The Change in the support of the random variables has been more significant when increasing the number of modes from 2 to 3. Since including mode 3 will increase the energy captured by modes from 92 to 99 % its presence is essential in convergence of the probability distribution. This has been seen in the noticeable change in the marginal distributions of Y_1 and Y_2 computed for a KLE expansion truncated after two terms compared with the ones computed for a KLE expansion truncated after three terms. In case of solving the MaxEnt problem for obtaining the marginal probability distribution of $Y_1, ..., Y_5$ that corresponds to truncating the Karhunen-Loève expansion after 5 terms the number of Lagrange parameters in MaxEnt problem equals to 20. The Lagrange parameters corresponding to the added terms that incorporates the dependency of the random variables has been negligible for modes 4 and 5 (i.e. the Lagrange pa-

rameters corresponding to $Y_1Y_4, Y_1Y_5, Y_2Y_4, Y_2Y_5, Y_3Y_4, Y_3Y_5, Y_4Y_5$ have been an order of magnitude smaller than the other ones). This implies that random variables 4 and 5 are almost independent of the rest.

Next, Eq.3.14 is used to obtain the Rosenblatt transformation relating these random variables to ξ_1, ξ_2, ξ_3 which are independent identically distributed random variables on the hypercube $[0, 1]^3$.

The microstructure has been subjected to a simple compression process with coefficients of velocity gradient equal to $\beta_3 = 0.35, \beta_i = 0.0, i \neq 3$.

An adaptive sparse grid with interpolation level 8 corresponding to 3527 collocation points has been used for this particular stochastic problem. The mean and variance of young modulus calculated at the end of the 8th level of interpolation are $1.18e05$ (MPa) and $8.61e07$ $(MPa)^2$ respectively. The same problem has been solved using Monte-Carlo (MC) method with 10000 runs. The mean and variance of young modulus obtained from MC are $1.18e05$ (MPa) and $8.52e07$ $(MPa)^2$ respectively.The convergence of the mean and the variance of the Young modulus is shown in Fig. 2.15 for different levels of adaptive interpolation. The mean and the variance of the final texture at the end of the simple compression process with random initial texture are calculated using Eqs. 3.18 and 3.19 and are shown in Fig. 2.16. The variation in the stress-strain response due to the randomness in initial texture is shown in Fig. 2.17 where the bars represent the standard deviation of the effective stress for the corresponding effective strain. This result has been compared with that of (MC) method. The maximum of relative differences between standard deviation of stress at specific strain obtained from these two methods has been $4\ \%$. As observed from Fig. 2.17 the variation in stress-strain response increases as the deformation de-

velops. This is due to increase in variance of evolved texture as the deformation develops (Eq. 2.6).

As mentioned before, in order to obtain the complete statistical characteristics of the random variables Y_{f1}, Y_{f2}, Y_{f3} in the Karhunen-Loève expansion (Eq. (2.11)) one needs many realizations of the final texture $\hat{\boldsymbol{A}}_f$. A set of 10000 realizations of the final texture obtained from the interpolant obtained in the collocation method (Eq. (3.15)) have been used to construct the unbiased estimate of the underlying covariance matrix. This covariance matrix is for the random vector representing the final texture obtained as the result of the simple compression process subjected to the random initial texture.

The first 3 eigenvalues correspond to 95 $\%$ of the spectrum. Hence the random process representing the final texture can be approximated by a 3-dimensional stochastic space. The 3 random variables used for the Karhunen-Loève approximation of the final texture are here defined as Y_{f1}, Y_{f2}, Y_{f3}. The convex hull of Y_{f1}, Y_{f2}, Y_{f3} is shown in Fig. 2.18. Next the closure of the properties obtainable from the random field representing the final texture is obtained. For doing so the optimization problem posed in Eq. (2.44) is solved in the convex hull of Y_{f1}, Y_{f2}, Y_{f3}. The closure of macro-scale properties is shown in Fig. 2.19.

2.10 Conclusion

In this chapter the effect of multiple sources of uncertainties in different scales on macro-scale properties is studied. For this purpose the convex hull of macro-scale properties obtainable from metal forming processes subjected to random processes or random initial texture is calculated. In order to reduce the dimen-

sion of the stochastic domain that the initial texture belongs to, Karhunen-Loève expansion is used to approximate the random field representing the uncertainty in microstructure by a set of random variables. The complete stochastic properties of these random variables can only be obtained if enough information on the microstructure is available. The aforementioned information is available through X-ray scattering techniques. In the absence of sufficient information, Maximum Entropy (MaxEnt) is used to obtain the joint probability of these random variables. Having a well-defined random initial texture and process parameters the resulting stochastic partial differential equation representing the evolution of texture can be solved by adaptive sparse grid collocation method. The propagation of uncertainty in microstructure evolution enables one to provide the bounds on macro-scale properties.

CHAPTER 3

A MODEL REDUCTION OF THE UNCERTAIN INPUT FOR QUANTIFYING THE EFFECT OF UNCERTAINTY IN A MULTI-SCALE STOCHASTIC PROBLEM

3.1 Introduction

Macro-scale properties of polycrystalline alloys depend on the preferred orientation of crystals in the underlying microstructure manifested as the crystallographic texture. During deformation processes, mechanisms such as crystallographic slip and lattice rotation drive the formation of texture. Variability in such processes and uncertainty in the initial texture of the material subjected to these processes have a significant effect on the final macro-scale properties. Obtaining the variation in material properties due to the inherent randomness of the microstructure is an important component in any materials design. Consider a closed die forging problem, having complete knowledge of the initial microstructure of the workpiece enables one to obtain the evolved microstructure due to the effect of the various deformation processes performed on the workpiece to obtain a specific final shape. The calculation of the evolved microstructure in turn enables one to obtain the macro-scale properties of the final product. In this work, Finite element dicretization is used to model the deformation process. Each point on the work-piece corresponds to an underlying texture. The texture is represented by an axis-angle representation in Rodrigues space and it evolves due to the effect of deformation process. In order to model this evolution, the Rodrigues space representing the texture corresponding to each integration point on macro-scale is also dicretized using Finite element

method. Hence, each integration point on macro-scale corresponds to an underlying mesh representing the corresponding texture. The fact that the initial workpieces may have a random initial geometry or microstructure has significant effect on the obtained macro-scale properties of the final product. This leads one to use stochastic methods in calculating the effect of uncertainties in initial texture and geometry on the final macro-scale properties of the workpiece.

The multi-scale phenomena of crystal reorientation in a deformation process using Finite element discretization have been the topic of previous works [4, 66, 67]. In the latest work a multi-scale sensitivity framework for the control of macro-scale properties in deformation processing has been studied [66]. Acharjee and Zabaras [68] have studied the effect of uncertain initial geometry for a deformation processing problem using a phenomenological constitutive model and hence neglecting the evolution of the underlying microstructure.

On the propagation of uncertainty there has been tremendous progress in posing and solving the stochastic partial differential equations governing various phenomena with uncertain components [24, 29, 31]. Venturi et al. [71] have studied a stochastic reduced order modeling of the random flow field where global polynomial chaos expansion (GPCE) framework was used to solve the stochastic partial differential equations governing the stochastic fluid flow problem. In their work the random field under study was decomposed into temporal and spatial modes using a bi-orthogonal framework. The effect of uncertain initial texture and processing parameters on the convex hull of macro-scale properties have been studied in [69]. There a point simulator have been considered and no multi-scale study has been provided. Quantifying the effect of uncertainty

in a multi-scale problem is not a trivial task. For example the effect of uncertain material properties in a multi-scale diffusion problem is presented in [70]. In that work for modeling the random heterogeneous media the reduced order modeling considered was only implemented on the fine scale. The method presented in [70] is viable for cases where the correlation length of material properties is much smaller than the shortest distance between the integration points. For the problems where there is a much higher correlation length for material properties if one uses the method presented in [70] the lack of a framework that could provide a reduced order model in multi-scale results in a problem with some random variables for each integration point on macro-scale. This in turn leaves no choice but to use Monte-Carlo to analyze the problem.

It should be noticed that the work-piece is subjected to a complicated deformation process with varying deformation gradients from one integration point to another. Hence, the inclusion of the underlying micro-structure and its evolution for every integration point on macro-scale is essential in quantifying the effect of deformation process on macro-scale properties.

The propagation of uncertainty in a multi-scale deformation process is a problem that to our best knowledge has not been tackled before due to the significant computational effort needed. This chapter provides a methodology for solving this problem. It should be noticed that while in [71] the stochastic field was decomposed into temporal and spatial modes in this work the random field is decomposed into modes in Rodrigues and spatial domain. As already mentioned, in [71] the GPCE framework is used to solve the stochastic partial differential equations governing the evolution of the stochastic field under study. Using this framework would require significant changes in the formulation of

the corresponding deterministic problem. In the method presented here a bi-orthogonal framework is used to approximate the initial random field. Hence the coefficients of the polynomial chaos terms are obtained using projections of the random modes on the chaos polynomials and for propagating the uncertainty a sparse grid collocation strategy is used which eliminates the need to significantly change the framework used in the corresponding deterministic problem.

As the number of random variables increases the computational effort needed to solve a stochastic multi-scale problem rapidly becomes a burden. This problem becomes more acute especially when the multi-scale problem itself is computationally expensive (like the multi-scale deformation process considered in here). One of the aims of this chapter is to represent a framework that enables one to approximate a random process in multi-scale with a reduced order model. This framework is meant to eliminate the need for redundant correlated random variables that would be needed in case of using methods as in [70]. Hencem it can be used to quantify the effect of uncertainty in the problem under study.

The plan of this chapter is as follows. Section 3.2 provides some background on the constitutive polycrystal plasticity model, texture evolution and kinematics in the multi-scale deformation problem under study. Section 3.3 provides the problem definition. Section 3.4 briefly reviews the sparse grid collocation method used in solving the stochastic differential equations. The reduced order model is presented in Section 3.5 while Polynomial chaos expansion used in the reduced order model is reviewed in in Section 3.6. Finally, Sections 3.7 and 3.8 present numerical examples and conclusions, respectively.

3.2 Constitutive problem and texture evolution

During a deformation process, crystallographic slip and re-orientation of crystals (lattice rotation) can be assumed to be the primary mechanisms of plastic deformation. The slip and re-orientation occur in an ordered manner such that a preferential orientation or texture develops. We follow the rate-independent constitutive model developed in [40].

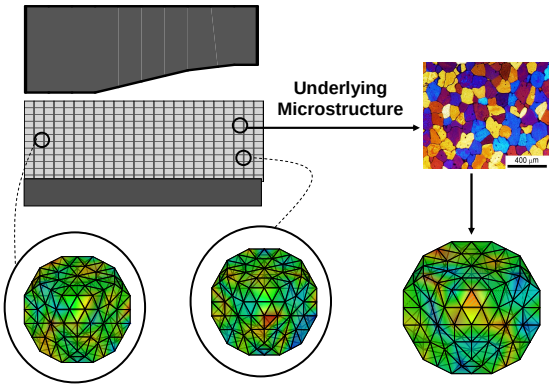

Figure 3.1: Schematic view of the multi-scale problem.

Consider a macroscopic material point and an associated underlying microstructure $\mathcal{M}$ discretized by a grid (Figure 3.1). Each point on this underlying grid corresponds to a different crystal orientation $\boldsymbol{R}$. At each point on the grid, the crystal lattice frame $\hat{e}_i$ is related to the sample reference frame $\boldsymbol{e}_i$ by $\boldsymbol{e}_i = \boldsymbol{R}\,\hat{e}_i$.

The Rodrigues-Frank axis-angle parameterization is used as a convenient scheme to represent $\boldsymbol{R}$ [44]. The parameterization is derived from the natural invariants of $\boldsymbol{R}$: the axis of rotation $\boldsymbol{n}$ and the angle of rotation $\hat{\zeta}$. The angle-axis parameterization, $\boldsymbol{r}$, is obtained by scaling the axis $\boldsymbol{n}$ by a function of the angle $\hat{\zeta}$ as $\boldsymbol{r} = \boldsymbol{n}\, f(\hat{\zeta})$. In the particular case of Rodrigues' parameterization, the

function is defined as $f(\hat{\zeta}) = \tan\left(\frac{\hat{\zeta}}{2}\right)$. Due to crystal symmetry, the Rodriguez parameterization of orientation is not unique. Restricting the Rodriguez domain to a fundamental zone that reflects the crystal symmetry leads to a one to one correspondence between the points on the Rodriguez space and the crystal orientation. For details on the constitutive model and texture evolution refer to the section 2.3.

3.2.1 Kinematics

Consider a closed form forging problem, this deterministic multi-scale problem consists of the following: The time history of the deformation including the elastic and plastic part, material state and texture are calculated incrementally as the result of external forces and the effect of contact between the workpiece and the die. For this purpose the deformation problem is divided into kinematics, contact, constitutive and texture evolution. An updated lagrangian framework in which the configuration at the previous step B_n is considered as the reference configuration for calculating the material configuration B_{n+1} is used to solve the deformation problem.

Let $\boldsymbol{X}$ be a material particle in $\boldsymbol{B}_0$ and let $\boldsymbol{x} = \tilde{\boldsymbol{x}}(\boldsymbol{X}, t_{n+1})$ be its location at time t_{n+1}. The total deformation gradient can be defined as

$$\boldsymbol{F}(\boldsymbol{X}, t_{n+1}) = \nabla_0 \tilde{\boldsymbol{x}}(\boldsymbol{X}, t_{n+1}) = \frac{\partial \tilde{\boldsymbol{x}}(\boldsymbol{X}, t_{n+1})}{\partial \boldsymbol{X}} \tag{3.1}$$

Using an updated Lagrangian framework, the total deformation gradient $\boldsymbol{F}$ at time $t = t_{n+1}$ can be expressed in terms of $\boldsymbol{F}_n$ at time $t = t_n$ as follows:

$$\boldsymbol{F} = \boldsymbol{F}_r \boldsymbol{F}_n \tag{3.2}$$

where $\boldsymbol{F}_r$ is the relative deformation gradient. The equilibrium equation at $t = t_{n+1}$ can be expressed in the reference configuration $\boldsymbol{B}_n$ as,

$$\nabla_{n\bullet} \langle \boldsymbol{P}_r \rangle + \boldsymbol{f}_r = 0 \tag{3.3}$$

where ∇_n denotes the divergence in $\boldsymbol{B}_n$. $\boldsymbol{f}_r$ can be represented as

$$\boldsymbol{f}_r = det\boldsymbol{F}_r \boldsymbol{b} \tag{3.4}$$

where $\boldsymbol{b}$ is the body force defined on the current configuration $\boldsymbol{B}_{n+1}$. The homogenized Piola-Kirchhoff I stress $\langle \boldsymbol{P}_r \rangle$ is expressed per unit area of $\boldsymbol{B}_n$ and given as follows:

$$\begin{aligned} \langle \boldsymbol{P}_r \rangle &= \langle det\boldsymbol{F}_r \boldsymbol{T} \boldsymbol{F}_r^{-T} \rangle \\ &= det\boldsymbol{F}_r \langle \boldsymbol{T} \rangle \boldsymbol{F}_r^{-T} \end{aligned} \tag{3.5}$$

where $\boldsymbol{T}$ is the Cauchy stress. The Taylor hypothesis for the macro-micro linking is assumed. An incremental quasi-static problem should be solved to determine the displacement field that satisfies Equation (3.3). The solution of the deformation problem proceeds incrementally in time starting from the initial configuration $\boldsymbol{B}_0$.

Equation (3.3)describes the equilibrium of the body at time t_{n+1} expressed in the updated reference configuration B_n. The incremental quasi-static boundary value problem at time $t = t_{n+1}$ is to find the incremental (with respect to the configuration B_n) displacement field $\boldsymbol{u}(\boldsymbol{x}_n, t_{n+1}) = \boldsymbol{u}_{n+1}$ that will satisfy equation (3.3). The weak form of this equation can be presented as $\tilde{G}(\boldsymbol{u}_{n+1}, \tilde{\boldsymbol{\eta}}) = 0$ where $\tilde{\boldsymbol{\eta}}$ is a test vector field compatible with the kinematic boundary conditions. The reader can refer to Ref. [72] for complete derivation of the weak form.

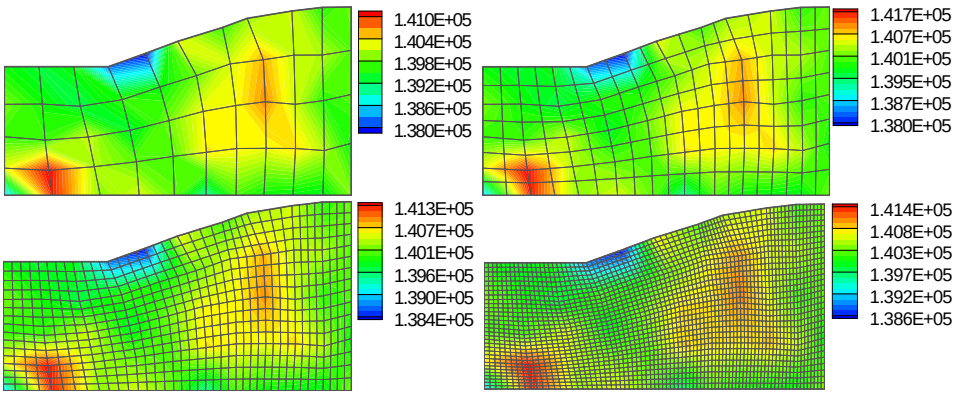

Figure 3.2: Convergence of Bulk modulus (MPa) with respect to the mesh refinement in the macro-scale

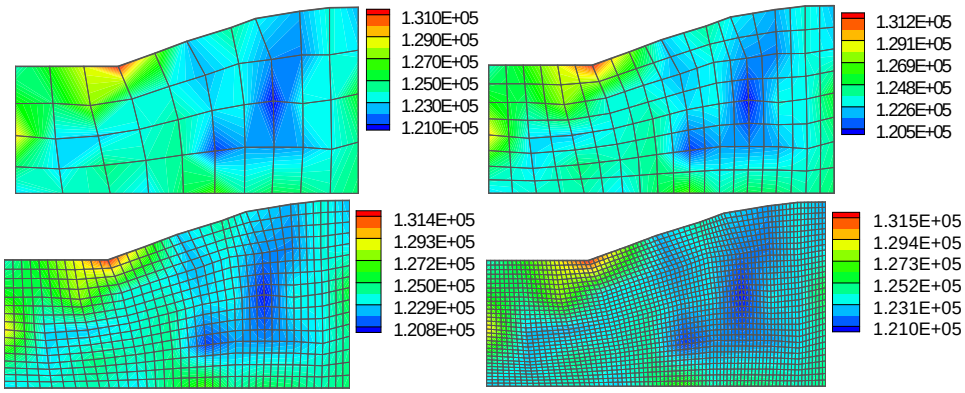

Figure 3.3: Convergence of Young modulus (MPa) with respect to the mesh refinement in the macro-scale

To solve this non-linear equation for $\boldsymbol{u}(\boldsymbol{x}_n; t_{n+1})$, a Newton Raphson iterative scheme along with a line search method is used [72]. Let $\boldsymbol{u}_{n+1}^{k+1}$ and $\boldsymbol{u}_{n+1}^{k}$ be the displacement fields at the end of the $(k+1)th$ step and the kth step, respectively, during the Newton Raphson iterative process. Then, the linearized form of the equation is as follows:

$$\tilde{G}(\boldsymbol{u}_{n+1}^{k}, \tilde{\boldsymbol{\eta}}) + \frac{\partial \tilde{G}}{\partial \boldsymbol{u}_{n+1}^{k}}(\boldsymbol{u}_{n+1}^{k+1} - \boldsymbol{u}_{n+1}^{k}) = 0 \tag{3.6}$$

The linearization of the part of $\tilde{G}$ which corresponds to the internal work is

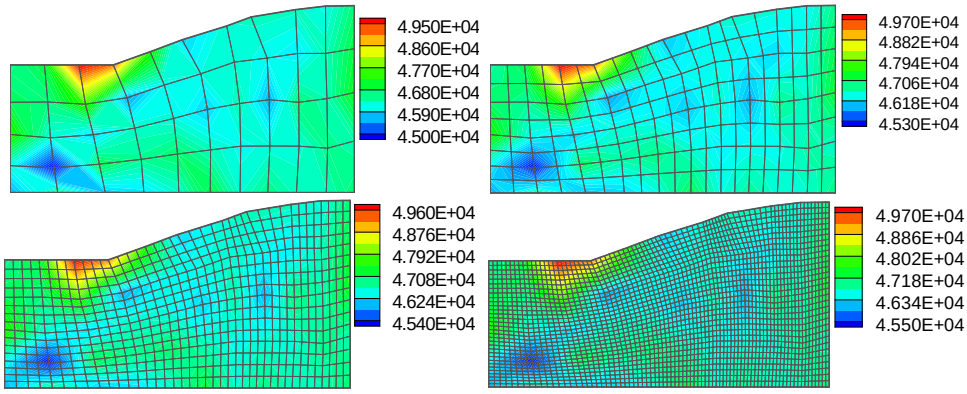

Figure 3.4: Convergence of Shear modulus (MPa) with respect to the mesh refinement in the macro-scale

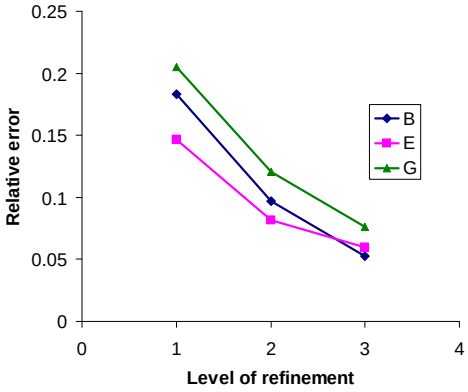

Figure 3.5: Convergence of macro-scale properties with respect to the level of mesh refinement

provided as [72]

$$d\tilde{G}_{internal} = \int_{\boldsymbol{B}_n} d\langle \boldsymbol{P}_r \rangle \bullet \frac{\partial \tilde{\boldsymbol{\eta}}}{\partial \boldsymbol{x}_n} dV \tag{3.7}$$

where the test displacement $\tilde{\boldsymbol{\eta}}$ is expressed over the initial configuration $\boldsymbol{B}_n$.

The linearization process of the micro-averaged (homogenized) PK-I stress is given as:

$$d\langle \boldsymbol{P}_r \rangle \;=\; \det \boldsymbol{F}_r \left(\text{tr}(d\boldsymbol{F}_r \boldsymbol{F}_r^{-1}) \langle \boldsymbol{T} \rangle - \langle \boldsymbol{T} \rangle \left(d\boldsymbol{F}_r \boldsymbol{F}_r^{-1} \right)^T + \langle d\boldsymbol{T} \rangle \right) \boldsymbol{F}_r^{-T} \tag{3.8}$$

where $d\boldsymbol{T} \;=\; d(\frac{1}{\det \boldsymbol{F}_r} \boldsymbol{F}_r \bar{\boldsymbol{T}} (\boldsymbol{F}_r)^T)$ requires the evaluation of $d\boldsymbol{F}_r$ and $d\bar{\boldsymbol{T}}$

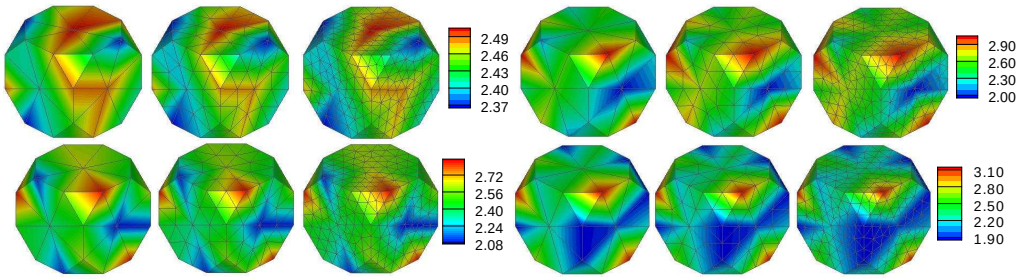

Figure 3.6: Convergence of texture evolution with respect to the element number in the micro-scale

using the constitutive model [66, 73].

For details on the linearization of the external work done by body and surface forces including the contact work at the die/workpiece surface refer to [72, **?**, 74]. The contact problem is solved using an augmented Lagrangian framework presented for 2D deformation in [72, 74] and 3D deformation in [**?**]. It is assumed that the contact problem is independent of the nature of the underlying microstructure, and that texture plays a role only through the stress response.

Note that as mentioned before each point on macro-scale corresponds to an underlying microstructure represented by another grid in discretized Rodrigues space. Hence the material state (including texture) is updated in the sub-grid related to micro-scale at each point on macro-scale. Figures 3.2, 3.3 and 3.4 show the convergence study of Bulk, Young and Shear modulus as macro-scale properties with respect to the mesh refinement. For all cases the underlying texture has been modeled by discretizing the Rodrigues space using 448 elements. The relative error for these macro-scale properties can be written as

$$\check{E}_l := \| \frac{X_l - X_0}{X_0} \|_{L_2(D)} \tag{3.9}$$

where D is the spatial domain, $\check{E}_l$ is the relative error of level $l(l = 1 : 3)$ mesh refinement with respect to level 4 mesh refinement (bottom right picture in Figures 3.2, 3.3 and 3.4), X_l is the value of the macro-scale property for level l refinement and X_0 is the corresponding value at level 4. Figure 3.5 shows this relative error with respect to the level of mesh refinement. Next, selecting level 2 mesh refinement in macro-scale the convergence of texture evolution for 4 points on macro-scale is shown in Figure 3.6.

3.3 Problem definition

The main focus of this chapter is to provide a framework for quantifying the effect of random initial geometry and texture on macro-scale properties of the product of a multiscale deformation process. For this purpose polycrystalline materials are considered.

Consider a complete probability space (Ω, F, P) where Ω is the event space, F the σ-algebra, and $P : F \to [0, 1]$ is the probability measure. The uncertainty in the problem we consider comes from:

(a) The variation in the surface of the initial work-piece represented by a degree 6 Bézier curve $R_\beta(\alpha, \omega), \omega \in \Omega$ as

$$R_\beta(\alpha, \omega) = 0.01 \times (5 + \sum_{i=1}^{6} \beta_i(\omega)\varphi_i(\alpha)) \tag{3.10}$$

where $\alpha = \frac{z}{H}$ represents the z-coordinate normalized with respect to the hight of the work-piece, β_i are the Bézier coefficients and φ_i are the basis func-

tions defined as

$$\begin{aligned}
\varphi_1(\alpha) &= (1.0-\alpha)^6 + 6\alpha(1-\alpha)^5 \\
\varphi_2(\alpha) &= 15.0(1.0-\alpha)^4\alpha^2 \\
\varphi_3(\alpha) &= 20.0(1.0-\alpha)^3\alpha^3 \\
\varphi_4(\alpha) &= 15.0(1.0-\alpha)^2\alpha^4 \\
\varphi_5(\alpha) &= 6.0(1.0-\alpha)\alpha^5 \\
\varphi_6(\alpha) &= \alpha^6
\end{aligned} \tag{3.11}$$

(b) Variation in the initial texture $\hat{A}_0(x, s, \omega)$; $x \in D$, $s \in \mathcal{R}$, $\omega \in \Omega$ where D is the spatial domain and $\mathcal{R}$ is the fundamental zone of the Rodrigues space. The random field $\hat{A}_0(x, s, \omega)$ represent the variability of the initial texture.

The kinematic problem in macro-scale can be represented in the stochastic framework as

$$\tilde{G}(\boldsymbol{u}^k_{n+1}, \tilde{\boldsymbol{\eta}}, \omega) = 0 \tag{3.12}$$

and the evolution of the underlying texture can be written as

$$\frac{\partial \hat{A}(x, s, t, \omega)}{\partial t} + \hat{A}(x, s, t, \omega) \bigtriangledown \cdot \boldsymbol{v}(s, t, \omega) \ = 0 \tag{3.13}$$

As mentioned before, Finite element discretization has been used for modeling the deformation process in macro-scale. Also, each integration point on macro-scale correspond to an underlying texture represented in the fundamental part of Rodrigues space by finite element discretization. So, the texture is

a field value at each point in macro-scale. Using a data-driven approach, the Karhunen-Loève expansion defined in the subsequent sections (Eq. 3.22) can be used to reduce the random field $\hat{A}_0(x, s, \omega)$ representing the initial texture to few modes in spatial domain and Rodrigues space. Using the finite dimensional noise assumption, the random field $\hat{A}_0(x, s, \omega)$ can be represented by a finite number of random variables $\hat{A}_0(x, s, \breve{\zeta}_1, \breve{\zeta}_2, ..., \breve{\zeta}_{n_d})$. In this data-driven approach, we assume that realizations of the random field $\hat{A}_0(x, s, \omega)$ are known (from experiments or simulation) from which a reduced order model converging in the second order moment sense [71] to the full order texture can be constructed. It should be noticed that the aforementioned reduced order model is used to reconstruct the random field representing the initial texture. The reconstructed initial texture is then used to solve for the multi-scale problem and the associated subproblem of texture evolution. No, model reduction is assumed in the latter stage. The reduced order model depends on n_d random variables $\breve{\zeta}_1, \breve{\zeta}_2, ..., \breve{\zeta}_{n_d}$. Rosenblatt transformation [57] can be used to transform these set of n_d random variables $\breve{\zeta}_1, \breve{\zeta}_2, ..., \breve{\zeta}_{n_d}$ to another set of n_d independent identically distributed uniform random variables $\xi_1, \xi_2, ..., \xi_{n_d}$ in a unit hypercube $[0, 1]^{n_d}$. This allows us to sample in this space and seamlessly use existent collocation algorithms [31] to obtain the probabilistic distribution of the final texture which in turn is used to obtain the distribution of macro-scale properties.

3.3.1 Transforming the random variables

As discussed previously, a collocation method is used for solving the stochastic partial differential equation representing the multi-scale deformation problem (see also Section 3.4). In this method, a unit hypercube $[0, 1]^{n_d}$ represents the

stochastic space where n_d is the dimension of the stochastic domain. This space is sampled using an adaptive sparse grid to compute the stochastic interpolant of the ODF. Each point in this sparse grid corresponds to a specific realization of the random variables used in constructing the reduced order representation (described in the following sections) of the initial texture. A transformation is needed to obtain the actual random variables from the coordinates of the sparse grid points from the hypercube. This subsection provides one such transformation.

Since the joint probability density of $\breve{\boldsymbol{\zeta}}$ is absolutely continuous on the domain of definition, the Rosenblatt [57] transformation can be used to relate the n_d variate distribution function $P_{\breve{\boldsymbol{\zeta}}}$ to that of $\xi_1, \ldots, \xi_{n_d}$ which are independent identically distributed (iid) uniform random variables on the hypercube $[0,1]^{n_d}$.

$$\begin{aligned}
\breve{\zeta}_1 &= {P_1}^{-1}(P_{\xi_1}(\xi_1)), \\
\breve{\zeta}_2 &= {P_{2|1}}^{-1}(P_{\xi_2}(\xi_2)), \\
&\vdots \\
\breve{\zeta}_{n_d} &= {P_{n_d|1:(n_d-1)}}^{-1}(P_{\xi_{n_d}}(\xi_{n_d}))
\end{aligned} \tag{3.14}$$

where $P_{i|1:(i-1)}, i = 1, \ldots, n_d$, is the distribution function of $\breve{\zeta}_i$ conditioned on $\breve{\boldsymbol{\zeta}}_1 = \breve{\zeta}_1, \breve{\boldsymbol{\zeta}}_2 = \breve{\zeta}_2, \ldots, \breve{\boldsymbol{\zeta}}_{i-1} = \breve{\zeta}_{i-1}$ obtained from $P_{\breve{\boldsymbol{\zeta}}}$. This would help in seamlessly incorporating the collocation strategy described in the next section to solve the stochastic partial differential equation under study.

3.4 Sparse grid interpolation: Modeling the effect of uncertainty

For obtaining the macro-scale properties one needs the underlying texture. This section provides a summary of the algorithm used in obtaining the effect of uncertainty on texture evolution. An adaptive sparse grid collocation strategy for constructing the stochastic solution for the evolution of the ODF is used. For details, the interested reader is referred to [31, 58].

The basic idea of the stochastic collocation method is to approximate the stochastic space using multi-dimensional interpolating functions. The method uses realizations of the function (i.e. the solution $\hat{A}_f(x, s, \boldsymbol{\xi}_i)$ of the SPDE Eq. (3.13), at a finite set of collocation points $\{\boldsymbol{\xi}_i\}_{i=1}^{n_n}$, where the evolved texture is shown by $\hat{A}_f$ and n_n is the number of collocation points). These finite number of deterministic solutions are used in constructing an interpolant of the ODF using hierarchical linear interpolating basis functions [31]. The sparse grid is based on the Newton-Cotes formulae using equidistant support nodes [31]. The sampling points on the hypercube ($\Gamma = [0, 1]^{n_d}$, where n_d is the number of stochastic dimensions) are defined using tensor products and following the Smolyak construction [61]. It is advantageous to choose the collocation points in a nested fashion to obtain many recurring points with increasing order of interpolation [31]. The texture is a function of x and s which represent the macro-scale and Rodrigues space and can be approximated using the sparse grid interpolants. The function $\hat{A}_f(x, s, \boldsymbol{\xi})$ can for example be approximated by the following:

$$\hat{A}_f(x, s, \boldsymbol{\xi}_i) = \sum_{|i| \leq q} \sum_j \theta_j^i(x, s).a_j^i(\boldsymbol{\xi}) \tag{3.15}$$

$$\hat{A}_f^{\,2}(x, s, \boldsymbol{\xi}_i) = \sum_{|i| \leq q} \sum_j \grave{\theta}_j^i(x, s).a_j^i(\boldsymbol{\xi}) \tag{3.16}$$

where for each point on macro-scale there is a sparse grid interpolant which represents the random texture at each discretized point in Rodrigues space. This is just a simple weighted sum of the value of the basis functions for all collocation points in the current sparse grid where $a_j^i \equiv a_j(\xi_j^i)$ are the n_d dimensional multilinear basis functions constructed from their corresponding 1-dimensional ones using tensor products, θ_j^i are the difference between the value of interpolant in current and previous interpolation level, $\grave{\theta}_j^i$ are as θ_j^i but for the second power of the interpolant, $q - n_d$ is the order of interpolation, n_d is the number of stochastic dimensions and the summation is over the collocation points selected in a hierarchical framework [31].

After obtaining the expression in Eq. (3.15), it is also easy to extract statistics [31]. The mean of the random solution can be evaluated as follows:

$$E[\hat{A}_f(x, s, \boldsymbol{\xi})] = \sum_{|i| \leq q} \sum_j \theta_j^i(x, s). \int_\Gamma a_j^i(\boldsymbol{\xi}) d\boldsymbol{\xi} \tag{3.17}$$

where the probability density function $p(\boldsymbol{\xi})$ is 1 since the stochastic space is a unit hypercube $[0, 1]^{n_d}$. As shown in [31], the multi-dimensional integral is simply the product of the 1D integrals which can be computed analytically. Denoting $\int_\Gamma a_j^i(\boldsymbol{\xi}) d\boldsymbol{\xi} = I_j^i$ one can rewrite Eq. (3.17) as

$$E[\hat{A}_f(x,s,\boldsymbol{\xi})] = \sum_{|i|\leq q}\sum_{j}\theta_j^i(x,s).I_j^i \tag{3.18}$$

The second order moment can be calculated from

$$E[\hat{A_f}^2(x,s,\boldsymbol{\xi})] = \sum_{|i|\leq q}\sum_{j}\grave{\theta}_j^i(x,s).I_j^i \tag{3.19}$$

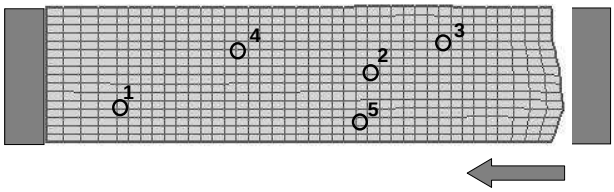

Figure 3.7: A sample of workpiece. The numbered points are investigated in subsequent figures.

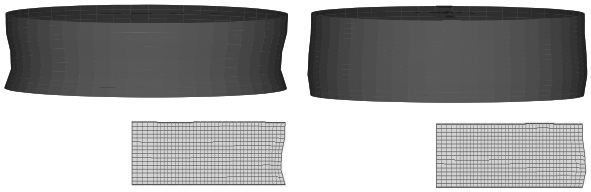

Figure 3.8: Two samples of the perturbed initial geometry.

Similarly, higher-order statistics can be calculated. As mentioned before, in constructing the interpolant that approximates the texture $\hat{A}_f(x,s,\boldsymbol{\xi})$ in the stochastic domain, one ends up with the realizations of $\hat{A}_f(x,s,\boldsymbol{\xi})$. These realizations are calculated at some collocation points representing specific realizations of the random variables. The realizations of the evolved (final) texture $\hat{A}_f(x,s,\boldsymbol{\xi})$ are from an underlying random field representing the final texture $\hat{\boldsymbol{A}}_f$. It should be noticed that since the initial texture has been evolved using the Eq. (3.13) the random field representing the final texture $\hat{\boldsymbol{A}}_f$ is different from that of initial texture. The realizations of $\hat{\boldsymbol{A}}_f$ can be obtained from the collection

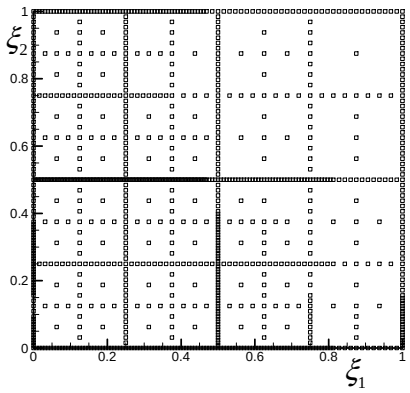

Figure 3.9: Sparse grid collocation points spanning the stochastic space of random Bezier parameters

of the realizations obtained at collocation points and the ones obtained from the constructed interpolant using Eq. (3.15).

3.5 Reduced order modeling

In practice, one has not access to the multi-dimensional interpolants in the stochastic space. The information usually comes as a set of realizations from the underlying random field. This section provides a framework to obtain a reduced order model for the underlying random field. Assume an L^2 random field $\breve{a}(x, s, \omega)$ defined on a probability space (Ω, F, p)

$$\breve{a}(x, s, \omega) : D \times \mathcal{R} \times \Omega \rightarrow \mathbb{R} \tag{3.20}$$

where D is the spatial domain, $\mathcal{R}$ is the fundamental part of Rodrigues space, Ω is the set of elementary events and $\omega \in \Omega$ is the vector of random inputs. One can use the Karhunen-Loève expansion to express this field by a biorthogonal

representation in the form

$$\begin{aligned} \check{a}(x,s,\omega) &= \bar{a}(x,s) + \hat{a}(x,s,\omega) \\ &= \bar{a}(x,s) + \sum_{i=1}^{\infty} \sqrt{\rho_i} \ \ {}_i(s)\Phi_i(x,\omega) \end{aligned} \tag{3.21}$$

where $\bar{a}$ is defined as $\bar{a}(x,s) = \langle \check{a}(x,s,\omega) \rangle$ and $\langle . \rangle$ is the averaging operation defined below, ρ_i are eigenvalues of the eigenvalue problem defined later on, the ${}_i$ are modes strongly orthogonal in Rodrigues space, Φ_i are spatial modes weakly orthogonal in space with respect to an inner product defined as

$$(f,g) := \int_D \langle f,g \rangle dx \tag{3.22}$$

$$\langle f,g \rangle = \int f(\omega)g(\omega)p(\omega)d\omega \tag{3.23}$$

where $p(\omega)$ is the probability distribution. The strong orthogonality of ${}_i$ modes in Rodrigues space can be written as

$$(\ {}_i, \ {}_j)_{\mathcal{R}} = \int_{\mathcal{R}} \ {}_i(s) \ \ {}_j(s)ds = \delta_{ij} \tag{3.24}$$

and the weak orthogonality of spatial modes can be written as

$$(\Phi_i, \Phi_j) = \delta_{ij} \tag{3.25}$$

By minimizing the distance (based on the norm defined in Eq. 3.22) between the Karhunen-Loève expansion and the random field one ends up with [71]

$$ {}_i(s) = \frac{1}{\sqrt{\rho_i}}(\hat{a}, \Phi_i) \tag{3.26} $$

and from the orthogonality condition

$$ \Phi_i(x,\omega) = \frac{1}{\sqrt{\rho_i}} \int_{\mathcal{R}} \hat{a}(x,s,\omega) \ \ {}_i(s) ds \tag{3.27} $$

Eqs. 3.26 and 3.27 lead to the following eigenvalue problem

$$ \rho_i \ \ {}_i(s) = \int_{\mathcal{R}} C(s,\acute{s}) \ \ {}_i(\acute{s}) d\acute{s} \tag{3.28} $$

where the covariance C is defined as

$$ C(s,\acute{s}) = (\hat{a}(x,s,\omega), \hat{a}(x,\acute{s},\omega)) \tag{3.29} $$

In discrete case the covariance can be written as

$$ \boldsymbol{C} = \frac{1}{n_r} \sum_{j=1}^{n_r} \sum_{i_n=1}^{n_{el}} \sum_{i_m=1}^{n_{int}} \hat{\boldsymbol{a}}_j(x_{i_m}) \hat{\boldsymbol{a}}_j^T(x_{i_m}) \hat{\eta}_{i_m} |J_{i_n}| \tag{3.30} $$

where $|J_{i_n}|$ is the jacobian determinant of the element i_n, $\hat{\eta}_{i_m}$ is the integration weight associated with the integration point i_m, n_{int} is the number of integration

points in each element, n_r is the number of realizations, n_{el} is the number of elements in macro-scale and $\hat{\boldsymbol{a}}$ is a column vector with elements corresponding to integration points in Rodrigues space and x_{i_m} represents global coordinate of the integration point i_m in macro-scale.

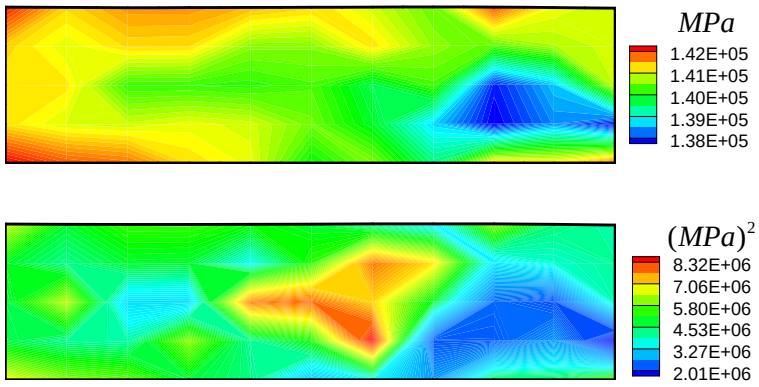

Figure 3.10: Mean and variance of the Bulk modulus

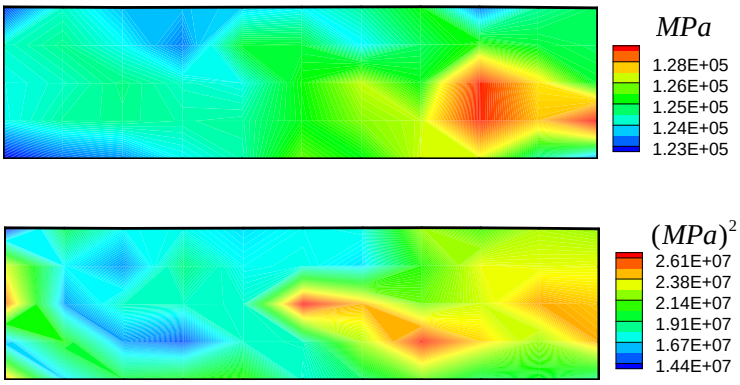

Figure 3.11: Mean and variance of the Young modulus

It should be noticed that the choice of inner product defined in Eq. 3.22 is not unique. In [71] three different inner products were explored out of which the one minimizing the second order moment of the error (the distance between the Karhunen-Loève expansion and the random field) is adopted in here.

The odf representing the texture takes positive values. Hence, the Karhunen-Loève expansion should provide us with positive values. To obtain a positive

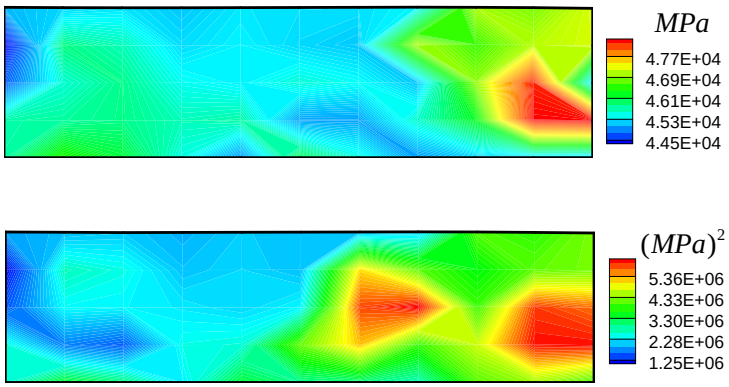

Figure 3.12: Mean and variance of the Shear modulus

random field, one can use the Karhunen-Loève expansion for the $\breve{a}(x,s,\omega) = log(\hat{A}(x,s,\omega) - A_{min})$ assuming that $\hat{A}(x,s,\omega) > A_{min} > 0$ almost surely [52]. The process $\hat{A}$ can be reconstructed as

$$A_{min} + exp(\breve{a}(x,s,\omega)) = A_{min} + exp(\overline{a}(x,s) + \sum_i \sqrt{\rho_i}\ \ _i(s)\Phi_i(x,\omega)) \qquad (3.31)$$

It should be noticed that as shown in Eq. 2.4 the significance of the values for each component of the texture $\hat{A}$ can be determined relative to its other components. In cases that the texture is constructed such that it approximates the distribution of orientations from a realistic picture of microstructure (schematically shown in Figure 3.1) some elements of $\hat{A}$ can be zero due to absence of the specific orientation in the picture. In this case a small number compared to other components of $\hat{A}$ should be provided instead of zero to avoid the unbounded $\hat{\boldsymbol{a}}$. Although a more robust method to tackle this problem is presented in [69], more development is still needed to apply it to the multi-scale case.

In practice $\breve{a}(x,s,\omega) := \breve{a}(x,s,\xi_1(\omega),...,\xi_{n_d}(\omega)$ where $\xi_1,...,\xi_{n_d}$ are a set of finite number of random variables and n_d refers to the number of random vari-

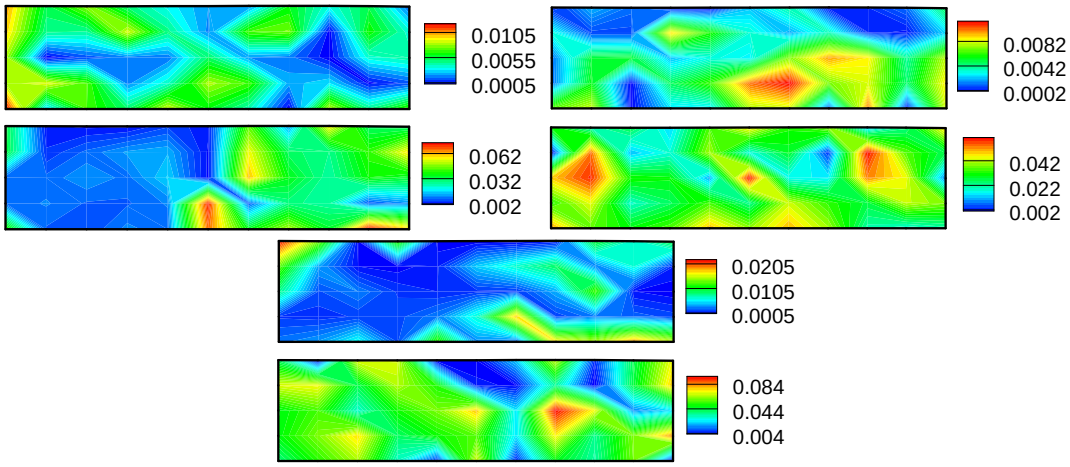

Figure 3.13: Comparison of Mean and variance of the macro-scale properties with MC, Top left: Bulk modulus, Top right: Young modulus, Bottom: Shear modulus

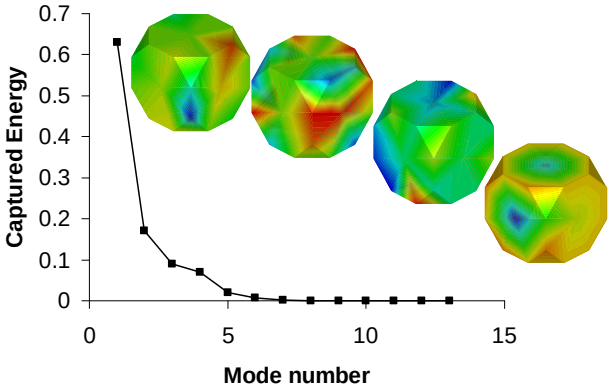

Figure 3.14: Eigenvalues and Eigenvectors

ables considered in the problem.

Next, the polynomial chaos decomposition of $\Phi_i(x,\omega)$ can be written as

$$\Phi_i(x,\omega) := \Phi_i(x,\zeta_1(\omega),...,\zeta_{n_d}(\omega)) = \sum_j \phi_{ij}(x)\eta_j(\omega) \tag{3.32}$$

where the $\eta_i(\omega) = \eta_i(\boldsymbol{\zeta}(\omega))$ are in a one to one correspondent to the Hermite polynomials in Gaussian variables presented in section 3.6 , $\boldsymbol{\zeta}(\omega)$ is the vector

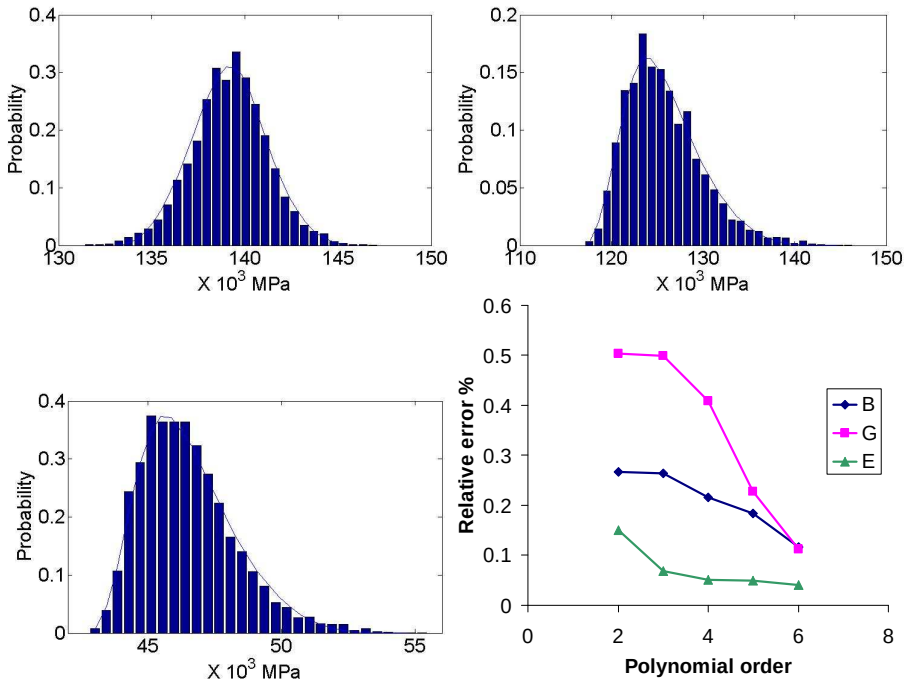

Figure 3.15: Top left: Distribution of Bulk modulus, Top right: Distribution of Young modulus, Bottom left: Distribution of Shear modulus, Bottom right: The relative error of macro scale properties with respect to the order of polynomial chaos used in the approximation. (For Point 1 on macro-scale)

consisting of n_d independent Gaussian random variables $(\zeta_1, ...\zeta_{n_d})$ and the coefficients $\phi_{ij}(x)$ can be obtained from

$$\phi_{ij}(x) = \frac{\langle \Phi_i(x, \boldsymbol{\zeta}) \eta_j \rangle}{\langle \eta_j^2 \rangle} \tag{3.33}$$

It should be noticed that in order to calculate the right hand side of above equation, Φ_i and η should be expressed in the same probability space. But Φ_i obtained from Eq. 3.27 is expressed with respect to $\boldsymbol{\xi}$ (Eq. 3.15) i.e. each realization of Φ_i is with respect to a set of n_d independent uniformly distributed random variable. A simple transformation as Eq. 3.14 can transform these random variables to a set of n_d independent Gaussian random variables with mean zero and

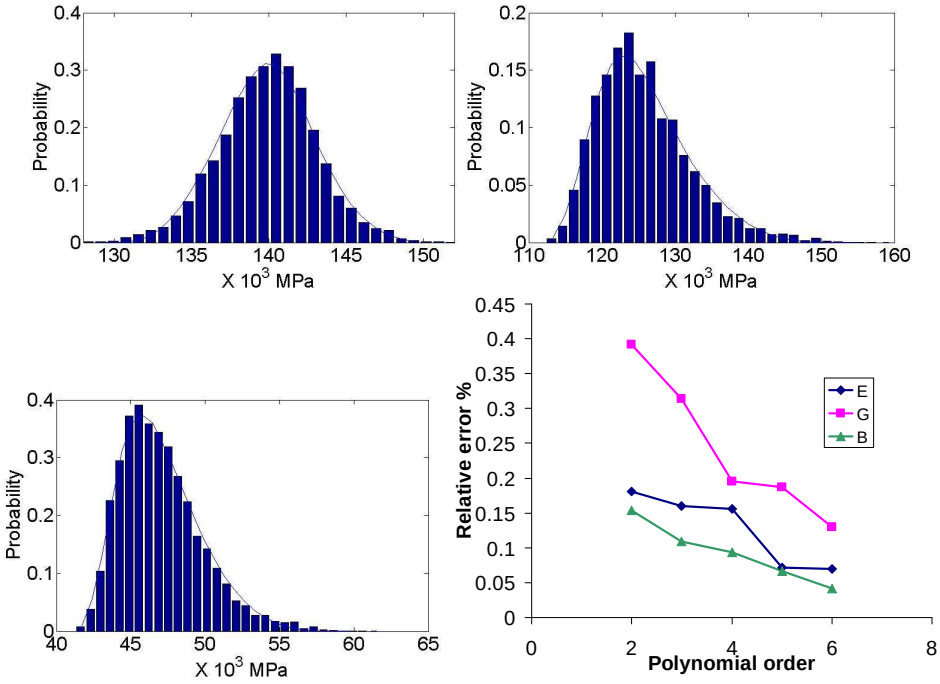

Figure 3.16: Top left: Distribution of Bulk modulus, Top right: Distribution of Young modulus, Bottom left: Distribution of Shear modulus, Bottom right: The relative error with respect to the order of polynomial chaos. (For Point 2 on macro-scale)

variance one $(\zeta_1, ..., \zeta_{n_d})$ as shown in Eq. 3.33.

3.6 Polynomial Chaos Expansion

A second order process can be approximated by a series of terms of Hermite polynomials in Gaussian variables (Cameron and Martin theorem [75]). This approximation is mean-square convergent. If $\Phi_i(x, \omega)$ is a second order random process ,$\langle \Phi_i(x, \omega), \Phi_i(x, \omega) \rangle < \infty$, it can be approximated as

$$\Phi_i(x, \omega) = Y_{i0}(x) H_0 + \sum_{i_1=1}^{\infty} Y_{ii_1}(x) H_1(\zeta_{i_1}(\omega)) \quad + \tag{3.34}$$

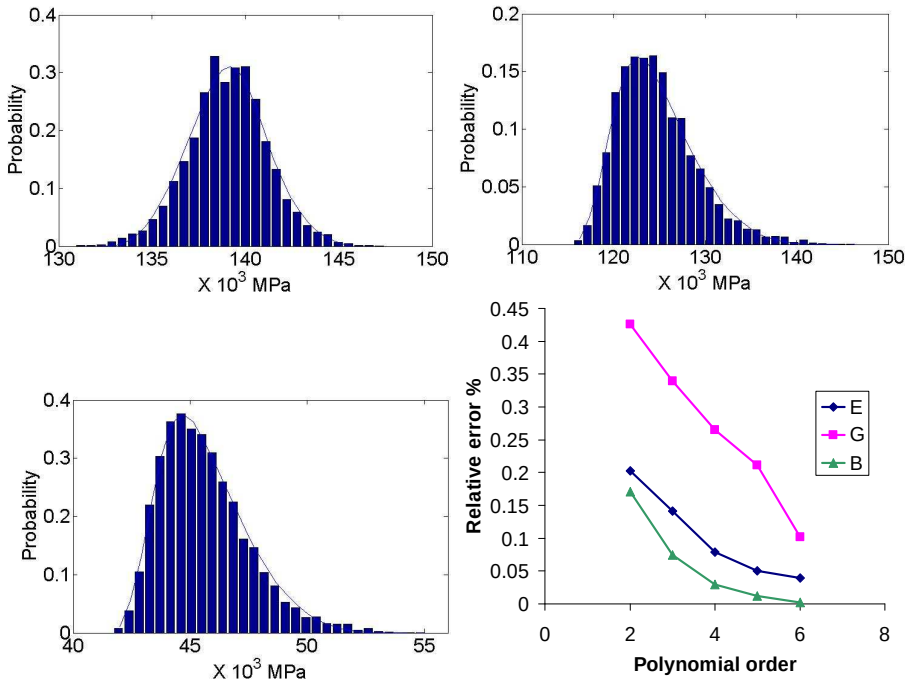

Figure 3.17: Top left: Distribution of Bulk modulus, Top right: Distribution of Young modulus, Bottom left: Distribution of Shear modulus, Bottom right: The relative error with respect to the order of polynomial chaos.(For Point 3 on macro-scale)

$$\sum_{i_1=1}^{\infty}\sum_{i_2=1}^{i_1} Y_{ii_1i_2}(x)H_2(\zeta_{i_1}(\omega),\zeta_{i_2}(\omega)) \quad + \\ \sum_{i_1=1}^{\infty}\sum_{i_2=1}^{i_1}\sum_{i_3=1}^{i_2} Y_{ii_1i_2i_3}(x)H_3(\zeta_{i_1}(\omega),\zeta_{i_2}(\omega),\zeta_{i_3}(\omega)) \quad + \quad ...$$

where $H_n(\zeta_{i_1},...,\zeta_{i_{n_d}})$ is the Hermite polynomial of order n in the Gaussian variables $(\zeta_{i_1},...,\zeta_{i_{n_d}})$ with zero mean and unit variance, i indexes the modes in Eq. 3.22 and $i_1, i_2, ...$ index the polynomial terms. The Hermite polynomials can be obtained from the following equation

$$H_n(\zeta_{i_1},...,\zeta_{i_{n_d}}) = e^{\frac{1}{2}\boldsymbol{\zeta}^T\boldsymbol{\zeta}}(-1)^n\frac{\partial^n}{\partial\zeta_{i_1}...\partial\zeta_{i_n}}e^{-\frac{1}{2}\boldsymbol{\zeta}^T\boldsymbol{\zeta}} \tag{3.35}$$

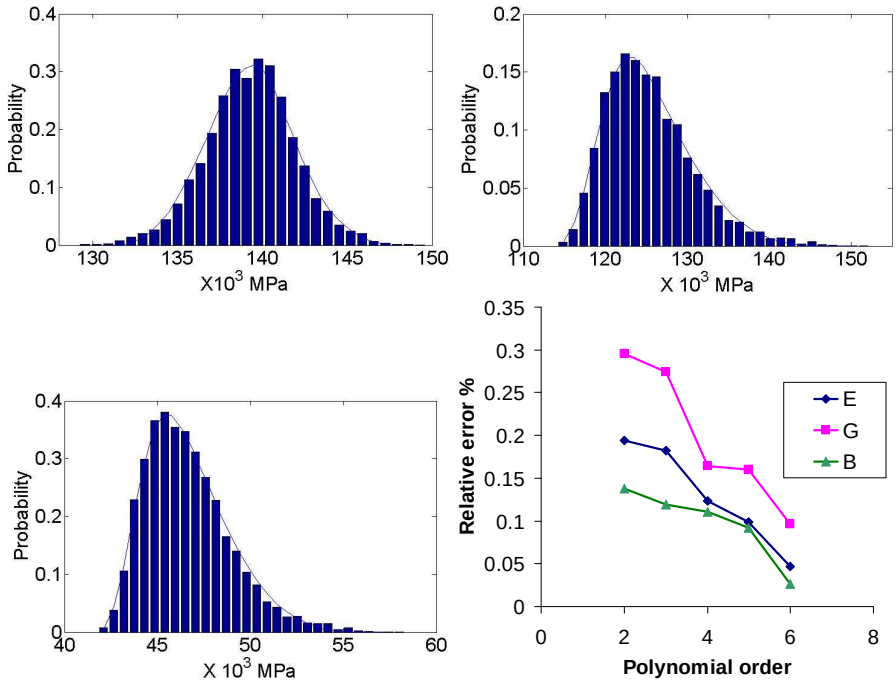

Figure 3.18: Top left: Distribution of Bulk modulus, Top right: Distribution of Young modulus, Bottom left: Distribution of Shear modulus, Bottom right: The relative error with respect to the order of polynomial chaos. (For Point 4 on macro-scale)

Eq. 3.34 can be rewritten as

$$\Phi_i(x,\omega) = \sum_{j=0}^{\infty} Y_{ij}(x)\eta_j(\boldsymbol{\zeta}) \tag{3.36}$$

where there is a one to one correspondence between functionals $H_n(\zeta_{i_1},...\zeta_{i_{n_d}})$ and $\eta_j(\zeta_{i_1},...\zeta_{i_{n_d}})$. In practice this series can be truncated with respect to the order of Hermite polynomials and the dimension of the random vector $\boldsymbol{\zeta}$.

The hermite polynomials are orthogonal with respect to the Gaussian probability measure i.e.

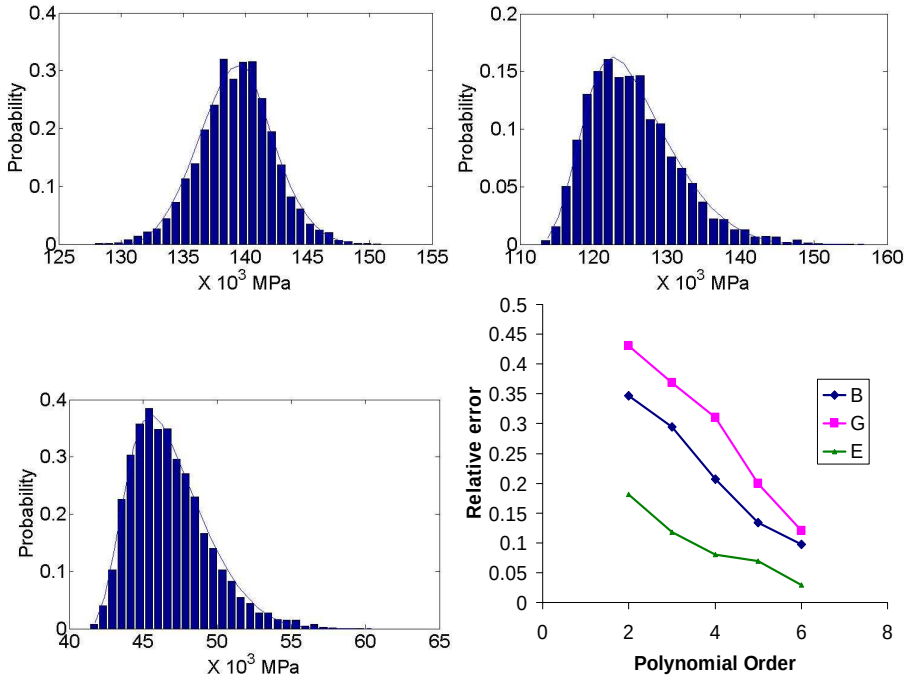

Figure 3.19: Top left: Distribution of Bulk modulus, Top right: Distribution of Young modulus, Bottom left: Distribution of Shear modulus, Bottom right: The relative error with respect to the order of polynomial chaos. (For Point 5 on macro-scale)

$$\langle \eta_i \eta_j \rangle = \langle \eta_i^2 \rangle \delta_{ij} \tag{3.37}$$

where $\langle . \rangle$ is the expectation operator

$$\begin{aligned} \langle \eta_i(\boldsymbol{\zeta}) \eta_j(\boldsymbol{\zeta}) \rangle &= \int \eta_i(\boldsymbol{\zeta}) \eta_j(\boldsymbol{\zeta}) P(\boldsymbol{\zeta}) d\zeta \\ P(\boldsymbol{\zeta}) &= \frac{1}{\sqrt{(2\pi)^{n_d}}} e^{-\frac{1}{2}\boldsymbol{\zeta}^T \boldsymbol{\zeta}} \end{aligned} \tag{3.38}$$

where $P(\boldsymbol{\zeta})$ is the n_d-dimensional independent Gaussian probability density function.

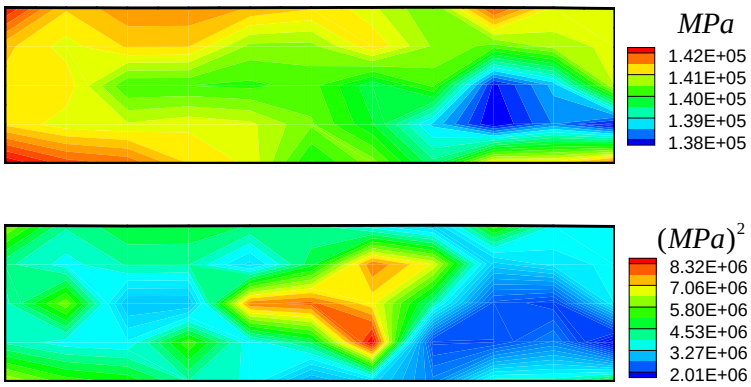

Figure 3.20: Mean and variance of the Bulk modulus obtained from the reduced order representation of texture

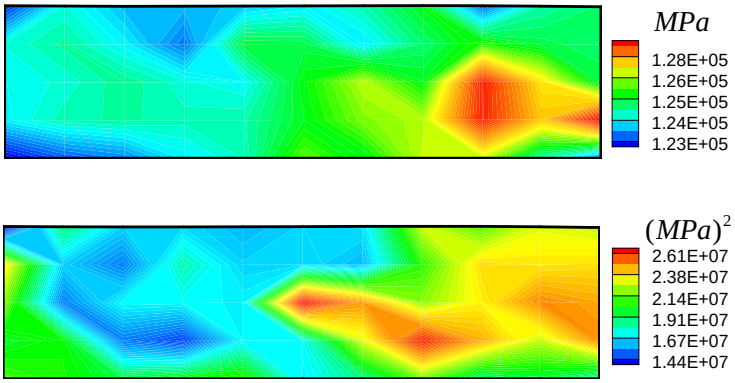

Figure 3.21: Mean and variance of the Young modulus obtained from the reduced order representation of texture

If the dimension of the random vector $\boldsymbol{\zeta}$ is n_d and the order of Hermite polynomials is p the total number of terms in polynomial chaos expansion is $P+1$

$$P+1 = \frac{(p+n_d)!}{p!n_d!} \tag{3.39}$$

The dimension of the random vector $\boldsymbol{\zeta}$ in polynomial chaos is dictated by the number of random variables driving the stochastic problem and the order of Hermite polynomials is decided from a convergence study on the proba-

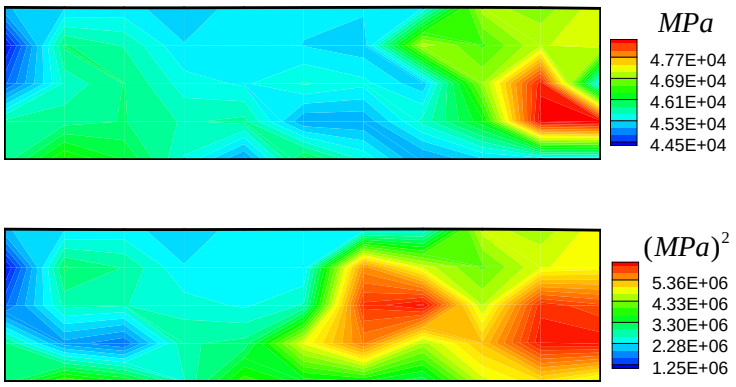

Figure 3.22: Mean and variance of the Shear modulus obtained from the reduced order representation of texture

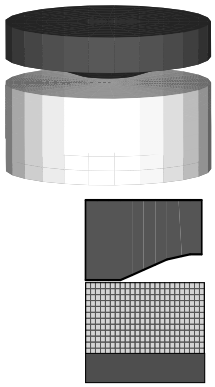

Figure 3.23: Schematic view of the work-piece and die in Example 2.

bility distribution of the random process $\Phi_i(x,\omega)$. If the dimension n_d of the random vector is known one can iterate over the order of Hermite polynomials p as follows. Construct the polynomial chaos expansions of dimension n_d and orders $m = p, p+1, ...$ and check the convergence of the reconstructed field. The number of terms in chaos expansion for each case can be written as $P(m)+1 = \frac{(m+n_d)!}{m!n_d!}$(Eq. 3.39). For example one can write the order p and order $p+1$ approximation as

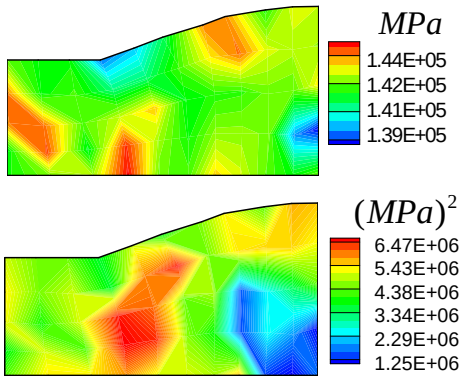

Figure 3.24: Mean and variance of the Bulk modulus obtained from the reduced order representation of texture

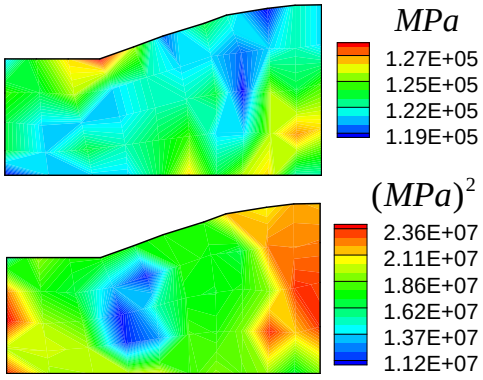

Figure 3.25: Mean and variance of the Young modulus obtained from the reduced order representation of texture

$$\Phi_i^{(p)}(x,\omega) = \sum_{j=0}^{P(p)+1} Y_{ij}(x)\eta_j(\boldsymbol{\zeta}) \tag{3.40}$$

$$\Phi_i^{(p+1)}(x,\omega) = \sum_{j=0}^{P(p+1)+1} Y_{ij}(x)\eta_j(\boldsymbol{\zeta})$$

Next, the weak-Cauchy convergence criterion can be used to insure that the L_2 norm of the difference in the two approximations is negligible, i.e.

$$E_i := \|\Phi_i^{(p+1)} - \Phi_i^{(p)}\|_{L_2(\Omega)} < \epsilon, 0 < \epsilon \ll 1 \tag{3.41}$$

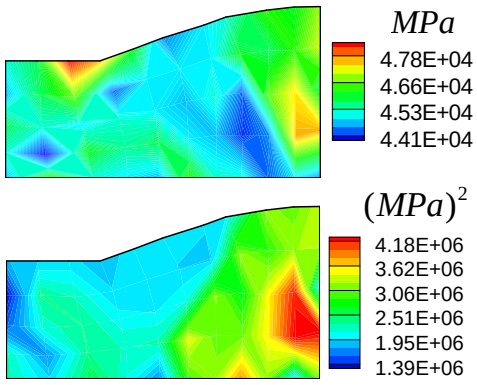

Figure 3.26: Mean and variance of the Shear modulus obtained from the reduced order representation of texture

where the error measure E is space function and the above convergence should hold on each point on macro-scale.

3.6.1 Computational aspects of polynomial chaos expansion

In order to obtain the coefficients of the polynomial chaos using Eq. 3.33 one can use the sampling method in which the sample values of $\boldsymbol{\zeta} = (\zeta_1, \zeta_2, ..., \zeta_{n_d})$ are drawn from the distribution of the $\boldsymbol{\zeta}$ which in this case is the n_d-dimensional independent Gaussian distribution.

For each sampling point, $\eta_i(\boldsymbol{\zeta})$ and $\Phi_i(x, \boldsymbol{\zeta})$ are evaluated. Using all the samples one can evaluate the expectation in the nominator of the Eq. 3.33. If the dimension of the stochastic space is large the best strategy for sampling are Monte Carlo or Latin Hypercube methods. The expectation in the denominator of Eq. 3.33 can be calculated and tabulated offline. For examples on the first few of the latter expectations one can refer to [24]. A more elegant and efficient way of calculating the expectations of the form $\langle \Phi(x, \boldsymbol{\zeta}) \eta(\boldsymbol{\zeta}) \rangle$ is to re-

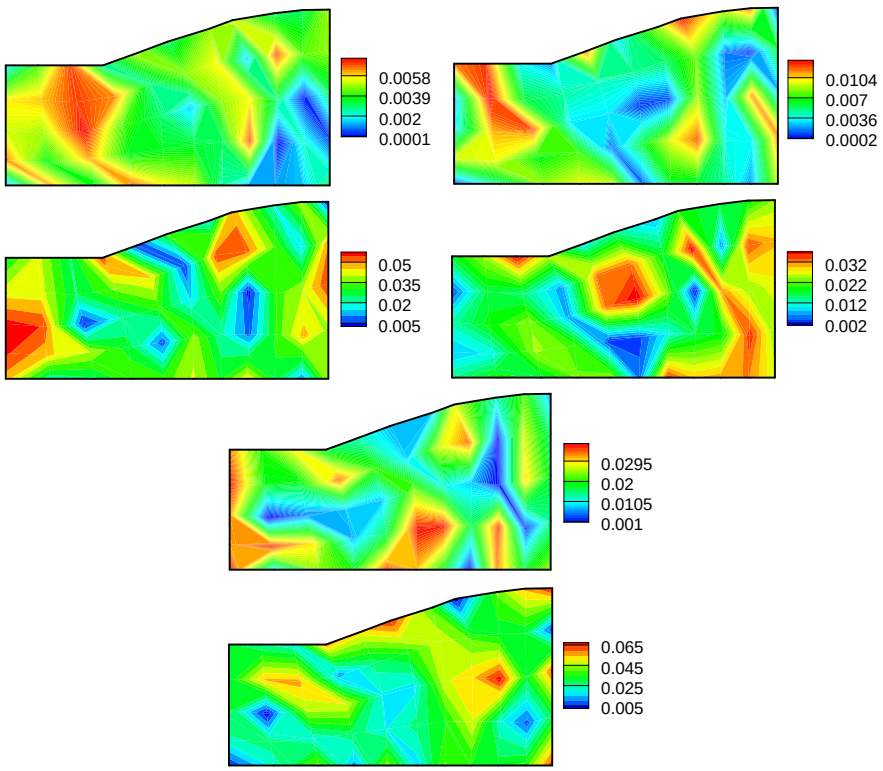

Figure 3.27: Comparison of Mean and variance of the macro-scale properties with MC, Top left: Bulk modulus, Top right: Young modulus, Bottom: Shear modulus

sort to Gauss-Hermite quadrature methods. This method is efficient for small dimensions of the stochastic space. In this method the expectation operator $\langle f \rangle$ is approximated as $\sum_i w_i f_i$ where w_i are the weights in the Gauss-Hermite quadrature method. If polynomial chaos expansion of order p is sufficient to represent the random process under study, then $p+1$ sample points on each stochastic domain are needed for calculation of the $\langle f \rangle$. The sample points for the multidimensional stochastic space are constructed from the sample points on each stochastic dimension using tensor product. The sample points on each stochastic dimension are the roots of the Hermite polynomial H_{p+1}

For a one dimensional case, one can write

$$\begin{aligned}\langle f\rangle &= \int_{-\infty}^{+\infty}\frac{1}{\sqrt{2\pi}}e^{-\frac{\zeta^2}{2}}f(\zeta)d\zeta \\ &= \frac{1}{\sqrt{2\pi}}\int_{-\infty}^{+\infty}e^{-\zeta^2}e^{\frac{\zeta^2}{2}}f(\zeta)d\zeta \sim \sum_{i=1}^{p+1}w_i f(\acute{x}_i)\end{aligned} \tag{3.42}$$

where $\acute{x}_i$ are roots of the Hermite polynomial H_{p+1} and the associated weights are given by

$$w_i = \frac{2^p(p+1)!\sqrt{\pi}}{(p+1)^2[H_p(\acute{x}_i)]^2}\times\frac{1}{\sqrt{2\pi}}e^{\frac{\acute{x}_i^2}{2}} \tag{3.43}$$

For the multi-dimensional stochastic space with dimension n_d these weights can be calculated using the multiplication of $w_1, ..., w_{n_d}$ calculated for each dimension at the corresponding coordinate of the sampling point.

3.6.2 Summary of the algorithm

First, let us look at the method used in [70]. Assume the information on the texture is given through realizations of the texture for each integration point on the macro-scale. There for each integration point one can write

$$\begin{aligned}\check{a}_1(s,\omega) &= \bar{a}_1(s) + \sum_{i_1=1}^{\infty}\sqrt{\rho_{i_1}}\ \ {}_{i_1}(s)\check{\alpha}_{i_1}(\omega) \\ \check{a}_2(s,\omega) &= \bar{a}_2(s) + \sum_{i_2=1}^{\infty}\sqrt{\rho_{i_2}}\ \ {}_{i_2}(s)\check{\alpha}_{i_2}(\omega) \\ &\vdots\end{aligned} \tag{3.44}$$

$$\begin{aligned} \check{a}_j(s,\omega) &= \bar{a}_j(s) + \sum_{i_j=1}^{\infty} \sqrt{\rho_{i_j}} \ {}_{i_j}(s)\check{\alpha}_{i_j}(\omega) \\ &\vdots \end{aligned}$$

where $\check{a}_j(s,\omega)$ is the value of random field corresponding to the integration point j, $\bar{a}_j$ is the expectation of the random field at integration point j, ρ_{i_j} and ${}_{i_j}(s)$ are the eigenvalues and eigenfunctions in Rodrigues space and $\check{\alpha}_{i_j}(\omega)$ are the set of uncorrelated but not necessarily independent random variables at integration point j. In this framework the realizations of the random variables at each integration point is obtained using

$$\check{\alpha}_{i_j}(\omega) = \frac{1}{\sqrt{\rho_{i_j}}} \int_{\mathcal{R}} \check{a}_j(s,\omega) \ {}_{i_j}(s) ds \tag{3.45}$$

Using these realizations one can use methods like the one presented in [69] to construct the probability distributions of these random variables at each integration point j. Now if the random variables at different integration points are correlated to each other then the aforementioned methodology has no means of figuring that out in another words it can not see the correlation between the set of random variables from different integration points. So, the number of random variables one would end up with would be the number of random variables needed for each integration point multiplied by the number of integration points. But if in a problem we know that the number of random variables driving the problem is much less than the aforementioned value then one should think of alternative methods. To address this problem one can use the method presented in the previous pages. A summary of the proposed algorithm is given in here:

The random field can be approximated as:

$$\hat{a}(x,s,\omega) = \sum_{i=1}^{\infty} \sqrt{\rho_i} \;\; {}_i(s)\Phi_i(x,\omega) \tag{3.46}$$

where ρ_i, ${}_i(s)$ are the eigenvalues and eigenfunctions (modes in Rodrigues space) of the covariance C. After constructing the covariance matrix and obtaining its eigenvalues and eigenfunctions the random spatial modes $\Phi_i(x,\omega)$ corresponding to each mode in Rodrigues space can be obtained by the following projection

$$\Phi_i(x,\omega) = \frac{1}{\sqrt{\rho_i}} \int_{\mathcal{R}} \hat{a}(x,s,\omega) \;\; {}_i(s) ds \tag{3.47}$$

Once the random spatial modes have been obtained they are decomposed to spatial and random space using polynomial chaos decomposition

$$\Phi_i(x,\omega) = \sum_j \phi_{ij}(x)\eta_j(\omega) \tag{3.48}$$

where $\eta_j(\omega)$ are Hermite polynomials in Gaussian variables with the dimension equal to the number of random variables driving the stochastic problem and the order obtained from a study on convergence of the decomposition and $\phi_{ij}(x)$ are coefficients of the decomposition which vary from one integration point to another and can be calculated using

$$\phi_{ij}(x) = \frac{\langle \Phi_i(x,\boldsymbol{\zeta})\eta_j \rangle}{\langle \eta_j^2 \rangle} \tag{3.49}$$

Now that all the components of the Eq. 3.46 are known it can be used to reconstruct the random field. Notice that the realizations of the random field were used to construct the covariance matrix. Hence, Eq. 3.46 represents the underlying random field and its realizations can be reconstructed as many times as needed using the realizations of the random variables in the Hermite polynomials.

3.7 Numerical examples

3.7.1 Example 1

In this example the effect of uncertainty in the geometry of the initial work-piece on the macro-scale properties of the product of deformation process is investigated. It is assumed that the surface of the initial work-piece $R_\beta(\alpha, \omega)$ can be represented by a degree 6 Bézier curve (Eq. 3.10).

In this problem the Bézier coefficients $\beta_1, \beta_4, \beta_5, \beta_6$ are assumed to be deterministic ($\beta_i = 0.05; i = \{1, 4, 5, 6\}$) and β_2, β_3 are considered as two independent random variables following $N(1, 0.1)$ distribution. Figure 3.8 shows few examples of workpieces constructed using realizations of β_2 and β_3. If all the Bézier coefficients are equal to 0.05 the resulting cylinder will have radius 5.5 cm.

The work-piece is subjected to a forging process with forging velocity specified as 0.01 cm/sec and when forged using a closed forming die depicted in Figure 3.7 the final product will be a cylinder of radius 4.0 cm.

The material considered here is FCC copper with the following material

properties

$$c_{11} = 170.0GPa,\ c_{12} = 124.0GPa,\ c_{44} = 75.0GPa, \tag{3.50}$$

For all points on macro-scale the underlying initial texture is assumed to be constant ($A_0(x, s) = 2.435$). This correspond to a texture having the same volume fraction for all possible orientations. Although the initial texture is assumed to be deterministic in this problem, the evolved texture at the end of the deformation process will be random due to the random initial geometry for the workpiece and the propagation of uncertainty through the deformation process.

A level 8 interpolating adaptive sparse grid corresponding to 1368 points for this particular stochastic problem has been used. The coordinates of the collocation points are shown in Figure 3.9. The coordinates of each collocation point correspond to the variables ξ_1 and ξ_2 which are independent uniformly distributed random variables between 0 and 1. These two random variables are mapped to β_2 and β_3 using Rosenblatt transform (Eq. 3.14). An approximation is made in this step in which the tails of the normal probability distribution are cut at values equal to the ($mean \pm 6 \times std$) where std is the standard deviation. This approximation is to avoid the infinite values for β corresponding to $\xi_1, \xi_2 = 0$ or 1. Cutting the tails of the probability distribution will have negligent effect on the properties under study (mean and variance of the macro-scale properties). The mean and variance of the Bulk, Young and Shear modulus are shown in Figures 3.10, 3.11 and 3.12. The same problem has been solved using Monte-Carlo (MC) method with 4000 runs. The relative error between mean and variance obtained from these two methods are shown in Figure 3.13. The relative error used in these figures can be written as $E_r = |\frac{X - X_{MC}}{X_{MC}}|$ where X is the macro-scale

property calculated using the samples of texture obtained from the interpolants resulting from the sparse grid collocation method and X_{MC} is the corresponding macro-scale property obtained from Monte-Carlo. The distribution of Bulk, Young and Shear modulus for few points on macro-scale (refer to Figure 3.7 for the position of these points) are shown in Figures 3.15, 3.16, 3.17, 3.18 and 3.19.

Next, a reduced order representation of texture is constructed using Eq. 3.22. First the covariance matrix C is calculated using Eq. 3.30. The first few eigenvalues and eigenvectors of this matrix are shown in Figure 3.14.

Using the first six significant modes obtained from the previous step, the spatial modes $\Phi_i(x, \omega)$ are calculated using Eq. 3.27. Next, Eq. 3.33 is used to obtain the polynomial chaos approximation of $\Phi_i(x, \omega)$. Having the reduced order representation, using Eqs. 3.22 and 3.31, 50000 sample textures are constructed for the macro-scale points in Figures 3.15, 3.16, 3.17, 3.18 and 3.19. The Bulk, Young and Shear modulus for these reconstructed textures are calculated and compared to that of the full order texture in Figures 3.15, 3.16, 3.17, 3.18 and 3.19. These figures correspond to macro-scale points 1-5 shown in Figure 3.7 respectively. In these figures the top left figure represent the distribution of Bulk modulus while the top right and bottom left show the distribution of Young and Shear modulus respectively. Also, the bars represent the distribution of the corresponding macro-scale property calculated from samples of the texture obtained from the interpolant constructed by sparse grid collocation (Eq. 3.15). The solid line shows the distribution of the same property calculated from the samples obtained from the reduced representation of the texture. The percentage of the relative error defined as $\tilde{E} := \|(X^{p+1} - X^p)/X^{p+1}\|_{L_2(\Omega)}$ is also shown vs. polynomial order in the aforementioned figures.

Figures 3.20, 3.21 and 3.22 show the of mean and variance for the Bulk, Young and Shear modulus on macro-scale using samples of textures reconstructed from the reduced order modeling. Reasonable match has been achieved in comparison to Figures 3.10, 3.11 and 3.12.

3.7.2 Example 2

The final texture of Example 1 is used as the initial texture in this example. As described in previous example, Eq. 3.22 is used to construct a reduced order representation of the random process $A_0(x, s, \omega)$. In this case the first 6 eigenmodes of the covariance matrix C (Eq. 3.30) were used and for each of these eigenmodes Eq. 3.27 is used to construct the spatial eigenmodes. An order 6 polynomial chaos expansion is used to approximate these spatial eigenmodes and the dimention of the random vector $\boldsymbol{\zeta}$ is the same as the dimension of the random vector driving the first example (i.e. $dim(\boldsymbol{\zeta}) = 2$). Hence using Eq. 3.39 it is obvious that for each point on macro-scale and for each eigenmode in Rodrigues space a set of 28 polynomial coefficients are used. These coefficients along the eigenmodes and eigenvectors of covariance C (Eq. 3.30) are used to reconstruct the random process $A_0(x, s, \omega)$ representing the initial texture of Example 2.

It should be noticed that except using the knowledge from the first example on having a stochastic space with rank 2 there is no connection between these two examples. So, this example is not a second stage of a multistage deformation process with its first stage being Example 1. The previous example is only used to construct a distribution of random initial texture for this example. In

order to consider a multistage problem one also needs to transfer other quantities quantifying the material state at the end of the first stage (e.g. deformation gradient, state of residual stress and strain rate , etc.). Also, an unloading stage should be considered immediately at the end of first stage (after removing the die) and before the beginning of the second stage. But this realistic scenario is avoided here in favor of simplicity and Example 2 deals with one stage of deformation process with random initial texture. The reader is reminded that using the method in [70] for the same amount of knowledge (realizations of the texture at each integration point on the macro-scale and knowledge of the rank of the stochastic space) one will end up with random variables for each integration point without exploiting the correlation between them.

The work-piece and the die are as depicted in Figure 3.23 and the forging velocity is considered to be 0.01 cm/sec. When solving this problem using sparse grid collocation the coordinates of each point on the sparse grid correspond to ξ_1 and ξ_2 which are two independent uniformly distributed random variables. Rosenblatt transform (Eq. 3.14) is used to transform these to ζ_1 and ζ_2 which follow an $N(0,1)$ distribution. ζ_1 and ζ_2 are in turn used to construct samples of $\Phi(x,\omega)$ using Eq. 3.32 and finally Eqs. 3.22 and 3.31 were used to construct the corresponding realization of $A_0(x,s,\omega)$ that would be used as the initial texture of the work-piece.

Figures (3.24, 3.25 and 3.26) show the mean and variance of the Bulk, Young and Shear modulus obtained from a sparse grid collocation of level 7 with 1274 sample points. These results were compared to that of Monte Carlo using 6000 samples in Figure 3.27.

3.8 Conclusions

The effect of uncertain initial geometry and texture on final macro-scale properties of the product of a multi-scale deformation process is investigated through examples. A reduced order representation of the random field representing texture is obtained using Karhunen-Loève expansion. This reduced order model provides a framework that makes the otherwise intractable task of quantifying the effect of random initial texture in a multiscale problem feasible.

3.9 Suggestions for the future work

As mentioned in this chapter, in order to quantify the effect of uncertainty propagation in a multi-scale deformation problem the stochastic space is collocated. Each collocation point corresponds to a realization of the random variables driving the stochastic problem. So, at each collocation point one deterministic multi-scale deformation problem needs to be solved. Since many deterministic problems should be solved any reduction in the computational cost necessary for solving the deterministic problem is extremely valuable. Hence, in order to be able to quantify the effect of uncertainty for a problem with many random variables, some model reduction strategies on the deterministic multi-scale deformation problem is needed for the future developments.

APPENDIX A

CHAPTER 1 OF APPENDIX

In this appendix the Rosenblatt transformation is explained in more details though an example. The necessity of this transformation is explained in chapters 2 and 3 where it is used to transform a set of independent identically distributed uniform random variables ξ_i to a set of random variables Y_i with desired probability distribution.

The transformation can be written as

$$\begin{aligned} Y_1 &= {P_1}^{-1}(P_{\xi_1}(\xi_1)), \\ Y_2 &= {P_{2|1}}^{-1}(P_{\xi_2}(\xi_2)), \\ &\vdots \\ Y_i &= {P_{i|1:(i-1)}}^{-1}(P_{\xi_i}(\xi_i)) \end{aligned} \tag{A.1}$$

where $P_{i|1:(i-1)}, i = 1, \ldots, n_d$, is the distribution function of Y_i conditioned on $\boldsymbol{Y}_1 = Y_1, \boldsymbol{Y}_2 = Y_2, \ldots, \boldsymbol{Y}_{i-1} = Y_{i-1}$.

This method is explained with more details through the following example. Assume a set of four random variables, Y_1, Y_2, Y_3 and Y_4, with the following joint probability distribution function

$$\begin{aligned} p = c_1 \exp(0.3Y_1 - Y_1^2 &+ 0.2Y_2 - 0.5Y_2^2 + 0.4Y_3 - 0.8Y_3^2 \\ &+ 0.3Y_4 - 0.5Y_4^2 + 0.2Y_1Y_2 + 0.6Y_1Y_3 + 0.2Y_3Y_4) \end{aligned} \tag{A.2}$$

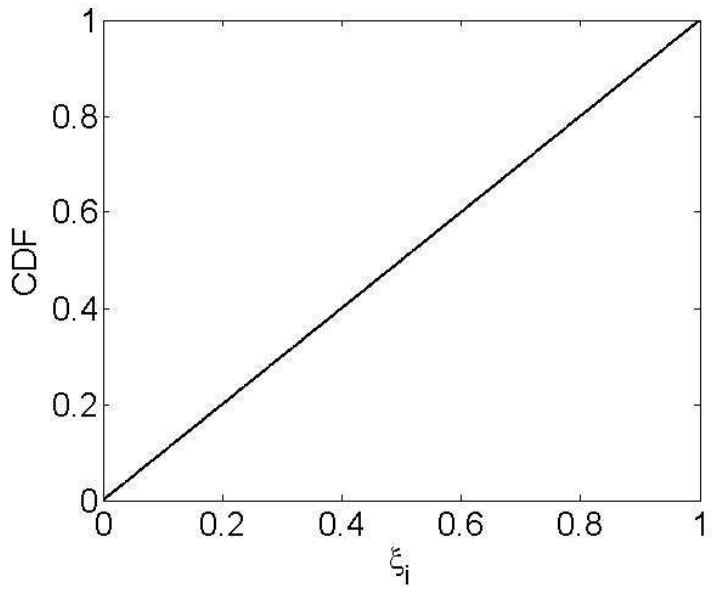

Figure A.1: The distribution function of independent uniformly distributed random variables ξ_1, ξ_2, ξ_3 and ξ_4

where c_1 is the normalization constant. The main idea is to use Eq. A.1 to transform the realizations of the random variables ξ_1, ξ_2, ξ_3 and ξ_4 sampled on the hypercube $[0, 1]^4$ to realizations of the Y_1, Y_2, Y_3 and Y_4 following the desired probability distribution. The distribution function of independent uniformly distributed random variables ξ_1, ξ_2, ξ_3 and ξ_4 is shown in the figure A.1. In order to verify the transformation, the marginal probability distribution of random variables Y_1, Y_2, Y_3 and Y_4 obtained from the joint probability distribution through integration in random space is shown in Figure A.3. It should be noticed that the transformation in Eq. A.1 is conducted step by step. In other words the transformation is conducted on the random variable ξ_i having the information on the prior transformed random variables $Y_1, ..., Y_{i-1}$. In this example, in order to check the algorithm first a set of realizations of the uniformly distributed random variable $\xi_1 \in [0, 1]$ are transformed to Y_1. Then assuming a fixed value for Y_1, e.g. $Y_1 = 0.5$, the corresponding conditional distribution function for Y_2 is obtained $P(Y_2|Y_1)$ from Eq. A.2. This is used in Eq. A.1 to conduct

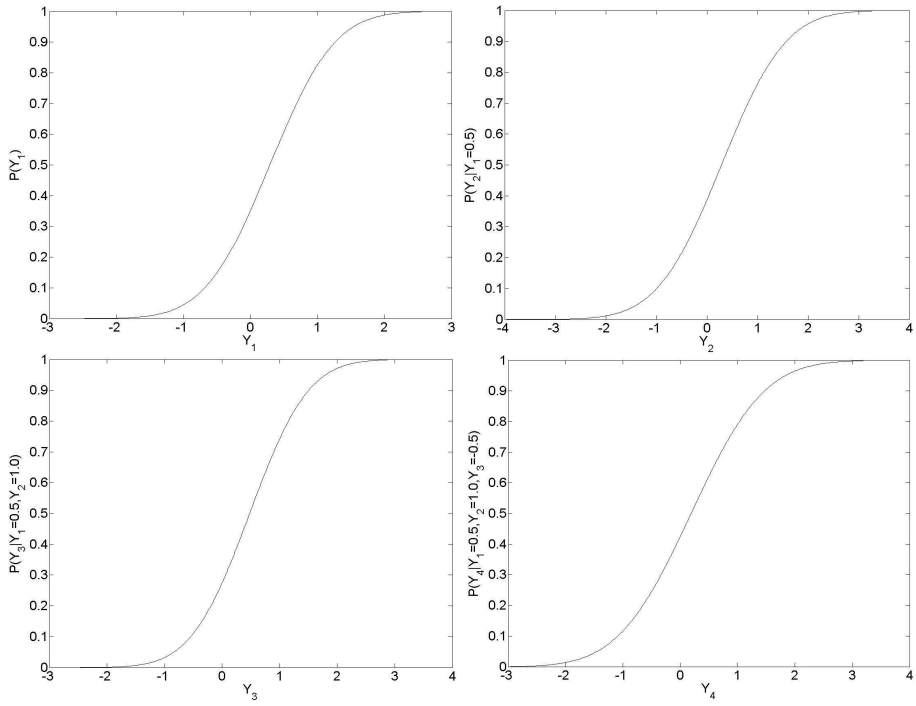

Figure A.2: (Cumulative) distribution function for Y_1, Y_2, Y_3 and Y_4

the second step of transformation where the random variable ξ_2 is transformed to Y_2 having the knowledge on the value of Y_1. The same procedure has been done for random variables Y_3 and Y_4 where for example for transforming ξ_4 to Y_4 the information on the value of Y_1, Y_2 and Y_3 is needed. In order to obtain each of the marginal probability distribution of Y_1, Y_2, Y_3 and Y_4 from the Eq. A.2 the integration in the random space is carried on using 1000000 points. After obtaining the marginal probability distribution the (cumulative) distribution function can be obtained through an integration in random space. Figure A.2 shows the distribution functions used in the transformation. Also, for comparison the distribution of realizations of Y_1, Y_2, Y_3 and Y_4 obtained through transforming realizations of independent uniformly distributed random variables ξ_1, ξ_2, ξ_3 and ξ_4 on the hypercube $[0, 1]^4$ is shown in Figure A.4 .

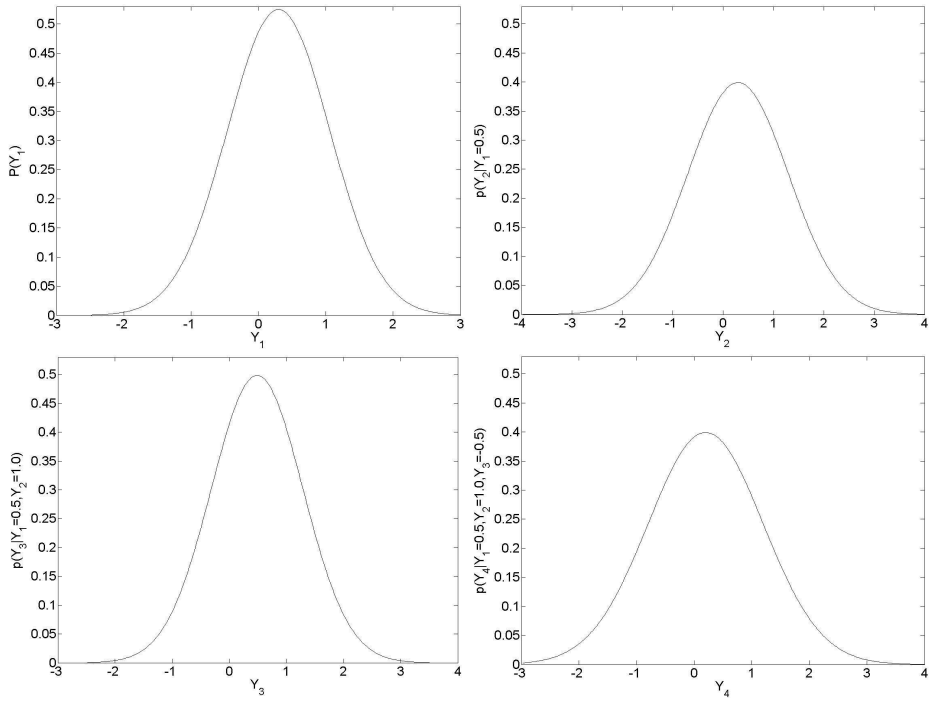

Figure A.3: The probability distribution of Y_1 and conditional probability distribution of Y_2, Y_3 and Y_4 obtained from joint probability distribution through integration in random space

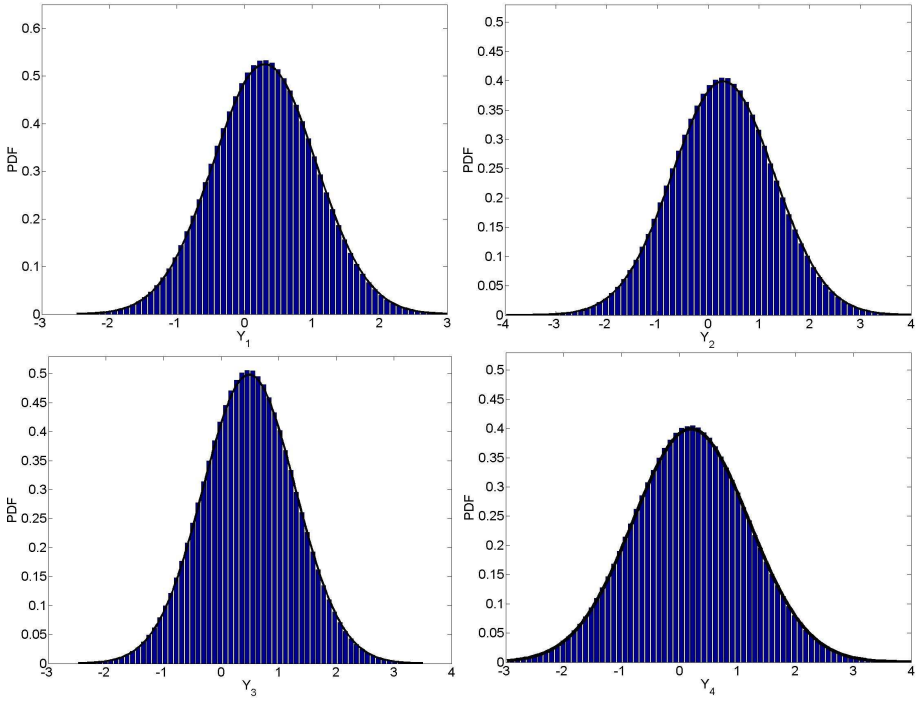

Figure A.4: Comparison between the probability distribution of Y_1, Y_2, Y_3 and Y_4 obtained from joint probability distribution through integration in random space (solid line) and from transforming a set of independent uniformly distributed random variables in $[0, 1]^4$ using the Rosenblatt transformation (bars)

BIBLIOGRAPHY

[1] Mathur K K and Dawson P R, *On modeling the development of crystallographic texture in bulk forming processes*, Int. J. Plast. 5 (1989) 67-94.

[2] Beaudoin A, Mathur K K, Dawson P R and Johnson G C, Three dimensional deformation process simulation with explicit use of polycrystalline plasticity models, Int. J. Plast. 9 (1993) 833-860.

[3] Bronkhorst C A, Kalidindi S R and Anand L, Evolution of crystallographic texture during the deformation of FCC metals, in: T.C. Lowe et al., eds., Modeling the deformation of crystalline solids (The minerals, metals and materials society, Warrendale), 1991.

[4] Ganapathysubramanian S, Zabaras N, Design across length scales: A reduced-order model of polycrystal plasticity for the control of microstructure-sensitive material properties, Comput Meth Appl Mech Engng. 193(2004)5017-5034.

[5] Ganapathysubramanian S, Zabaras N, Modeling the thermoelastic-viscoplastic response of polycrystals using a continuum representation over the orientation space, Int J Plasticity 21(2005)119-144.

[6] Myagchilov S, Dawson P R, Evolution of texture in aggregates of crystals exhibiting both slip and twinning, Modell Simul. Mater. Sci. Eng. 7(1999)975-1003.

[7] Staroselsky A, Anand L, A constitutive model for hcp materials deforming by slip and twinning: application to magnesium alloy AZ31B, Int. J. Plasticity 19(2003)1843-1864.

[8] Staroselsky A, Anand L, Inelastic deformation of polycrystalline face centered cubic materials by slip and twinning, J Mech. Physics. Solids 46(1998) 671-696.

[9] Kalidindi K R, Incorporation of deformation twinning in crystal plasticity models, J Mech. Physics. Solids 46(1998) 267-271.

[10] Tome C, Lebenson R A, Kocks U F, A model for texture development dominated by deformation twinning: Application to zirconium alloys, Acta Metall. Mater. 39(1991) 2667-2680.

[11] Van Houtte P, Simulation of the rolling and shear texture of brass by the Taylor theory adapted for mechanical twinning, Acta Metall. 26(1978) 591-604.

[12] Kumar A, Dawson P R, Modeling crystallographic texture evolution with finite elements over neo-Eulerian orientation spaces, Comput Meth Appl Mech Engng. 153(1998) 259-302.

[13] Ganapathysubramanian S, Design of deformation processes: Extending phenomenological and polycrystalline plasticity models towards the control of microstructure-sensitive properties, 2004; Ph.D. Thesis, Sibley School of Mechanical and Aerospace Engineering, Cornell University.

[14] Clement A, Prediction of deformation texture using a physical principle of conservation, Mater. Sci. Engrg. 55(1982), 203-210.

[15] Myagchilov S, ODF evolution modeling for polycrystals experiencing multiple slip and twinning with finite elements over orientation space; Ph.D. thesis; Cornell Univeristy; 1998.

[16] Philippe M, Serghat M, Modelling of texture evolution for materials of hexagonal symmetry-ii. application to zirconium and titanium, P. Van Houtte, C. Esling. Acta Metall. Mater. 43(1995)1619-1630.

[17] Asgari S, Danaf E E, Kalidindi S R,Doherty R, Strain hardening regimes and microstructural evolution during large strain compression of low stacking fault energy fcc alloys that form deformation twins, Metall. Mater. Trans. A. 28(1997) 1781-1795.

[18] Hosford W F, The mechanics of crystals and textured polycrystals, Oxford University Press, New York; 1993.

[19] Wu X, Kalidindi S R, Necker C and Salem A A, Prediction of crystallographic texture evolution and anisotropic stress-strain curves during large plastic strains in high purity α-titanium using a Taylor-type crystal plasticity model, Acta Materialia. 55(2007)423-432.

[20] Simmons G, Wang H, Single crystal elstic constants and calculated aggregate properties, The M.I.T. Press, Cambridge; 1971.

[21] Acharjee S, Zabaras N, The continuum sensitivity method for the compu-

tational design of three-dimensional deformation processes. Comput Meth Appl Mech Engng. 195(2006),6822-6842.

[22] Adams B L, Lyon M and Henrie B. Microstructures by design: linear problems in elasticplastic design, Int. J. Plasticity, 2004; 20(8-9):$1577-1602$.

[23] Sundararaghavan V, Zabaras N. Linear analysis of texture-property relationships using process-based representations of Rodrigues space, Acta Materialia,2007;$55(5):1573-1587$.

[24] Ghanem R G, Spanos P D, Stochastic Finite Elements: A Spectral Approach, Dover publications, 1991.

[25] Ghanem R G, Probabilistic characterization of transport in heterogeneous porous media, Comput. Methods Appl. Mech. Engrg. ,$1998; 158:199-220$.

[26] Wan X, Karniadakis G E, An adaptive multi-element generalized polynomial chaos method for stochastic differential equations, J. Comput. Phys. ,$2005; 209:617\ 642$.

[27] Xiu D, Karniadakis G E, The Wiener-Askey Polynomial Chaos for Stochastic Differential Equations, SIAM J. Sci. Computing, $2002; 24:619\ 644$.

[28] Foo J, Yosibash Z, Karniadakis G E, Stochastic simulation of riser-sections with uncertain measured pressure loads and/or uncertain material properties, Comput. Methods Appl. Mech. Engrg. ,$2007; 196:4250\ 4271$.

[29] Xiu D, Hesthaven J S, High-order collocation methods for the differential equation with random inputs, SIAM J. Sci. Comput. $2005; 27:1118\ 1139$.

[30] Xiu D, Efficient collocational approach for parametric uncertainty analysis, Comm. Computational Physics.$2007; 2:293\ 309$.

[31] Ma X, Zabaras N, An adaptive hierarchical sparse grid collocation algorithm for the solution of stochastic differential equations, Journal of Computational Physics, 2009;228:3084-3113.

[32] Ganapathysubramanian B, Zabaras N, Sparse grid collocation methods for stochastic natural convection problems, Journal of Computational Physics, $2007; 225:652-685$.

[33] Soize C, Construction of probability distributions in high dimension using the maximum entropy principle: Applications to stochastic processes,random fields and random matrices, Int. J. Numer. Meth. Engng.,2008; 76 : 1583− 1611.

[34] Das S, Ghanem R, Spall J C, Asymptotic sampling disribution for polynomial chaos representation from data: A maximum entropy and fisher information approach,2008; 30(5) : 2207− 2234.

[35] Kumar A, Dawson P R, The simulation of texture evolution with finite elements over orientation space I. Development, Comput. Methods Appt. Mech. Engrg.1996; 130 : 227− 246.

[36] Hansen J, Pospiech J, Liicke K, Tables for Texture Analysis of Cubic Crystals, Springer-Verlag, New York, 1978.

[37] Bunge H J, Texture Analysis in materials science,Butterworths, 1983.

[38] Kocks U F, Tome C N, Wenk H R, Texture and anisotropy - Preferred orientations in polycrystals and their effect on materials properties. Cambridge: Cambridge University Press, 2000.

[39] Sankaran S, Zabaras N, Computing property variability of polycrystals induced by grain size and orientation uncertainties, Acta Materialia,2007; 55 : 2279− 2290.

[40] Anand L, Kothari M, A computational procedure for rate-independent crystal plasticity, Journal of the Mechanics and Physics of Solids,1996; 44(4) : 525 558.

[41] Lee E H, Elastic-plastic deformation at finite strains. Journal of Applied Mechanics,1969; 26 : 1 6.

[42] Kumar A, Dawson P R, Polycrystal plasticity modeling of bulk forming with finite elements over orientation space, Computational mechanics.1995; 17 : 10− 25.

[43] Grigoriu M, Stochastic Calculus: Applications in Science and Engineering, Birkh$\ddot{a}$user Boston, 2002.

[44] Heinz A, Neumann P, Representation of orientation and disorientation

data for cubic, hexagonal, tetragonal and orthorhombic crystals, Acta Crystallographica, $1991; A47 : 780- 789$.

[45] Brooks A N, Hughes TJR, Streamline upwind/Petrov-Galerkin formulation for convection dominated flows with particular emphasis on the incompressible Navier-Stokes equation. Comput. Meth. APPl. Mech. Engng, $1982; 32 : 199- 259$.

[46] Zienkiewicz OC, Taylor RL., Finite element method (fluid dynamics), New YorkL: Butterworth-Heinemann, vol. 3.,2000.

[47] Kumar A, Dawson, PR, Computational modeling of FCC deformation textures over Rodrigues space, Acta Materialia,$2000; 48 : 2719\ 2736$.

[48] Loeve M, Probability Theory, Springer-Verlag: 4th Edition, Berlin, 1977.

[49] Ghanem R, Doostan A, On the construction and analysis of stochastic models: Characterization and propagation of the errors associated with limited data,Journal of Computational Physics, $2006; 217 : 63\ 81$.

[50] Phoon K K, Huang S P, Quek S T, Simulation of second-order processes using KarhunenLoeve expansion, Computers and Structures, $2002; 80 : 1049\ 1060$.

[51] Jaynes E T, Probability Theory: The Logic of Science, Cambridge University Press, 2003.

[52] Babuska I, Nobile F, Tempone R, A stochastic collocation method for elliptic partial differential equations with random input data, ICES Report,$2005; 05- 47$.

[53] Cover T M, Thomas J A, Elements of Information Theory. New York, NY: John Wiley, 1991.

[54] Ishwar P,Moulin P, On the existence and characterization of the MaxEnt distribution under general moment inequality constraints. IEEE Trans. Info. Theory 51 (2005) 3322-3333.

[55] Agmon N, Alhassid Y,Levine RD. An algorithm for finding the distribution of maximum entropy, Journal of computational physics $1979; 30 : 250- 258$.

[56] Berger A L, Della Pietra SL, Della Pietra VJ. A maximum entropy approach to natural language processing, Computational Linguistics $1996; 22 : 39-71$.

[57] Rosenblatt M, Remarks on multivariate transformation, Ann. Math. Statist.,$1952; 23 : 470- 472$.

[58] Ganapathysubramanian B,Zabaras N, A seamless approach towards stochastic modeling: Sparse grid collocation and data driven input models, Finite Elements in Analysis and Design,$2008; 44(5) : 298- 320$.

[59] Canuto C, Hussaini M Y, Quarteroni A, Zang TA, Spectral Methods: Fundamentals in Single Domains Series, Springer 2006 .

[60] Nobile F, Tempone R, Webster C, An anisotropic sparse grid collocation method for elliptic partial differential equations with random input data, MOX, Dipartimento di Matematica, Politecnico di Milano, Italy, 2007.

[61] Smolyak S, Quadrature and interpolation formulas for tensor product of certain classes of functions, Soviet Math. Dokl. $1963; 4 : 240\ 243$.

[62] Gerstner T, Griebel M, Numerical integration using sparse grids, Numerical Algorithms. $1998; 18 : 209\ 232$.

[63] Clerc D G, Ledbetter H M, Mechanical hardness: a semiempirical theory based on screened electrostatics and elastic shear. J. Phys. Chem. Solids. $1998, 59 : 1071- 1095$.

[64] Clerc D G, Mechanical hardness and elastic stiffness of alloys: semiempirical models. J. Phys. Chem. Solids. $1999, 60 : 83- 102$.

[65] Pugh S F. Relation between the elastic moduli and the plastic properties of polycrystalline pure metals. Phil. Mag. $1954, 45 : 823- 843$.

[66] Sundararaghavan V, Zabaras N, A multi-length scale sensitivity analysis for the control of texture-dependent properties in deformation processing , Int. J. of plasticity, 24 (2008), pp. 1581-1605.

[67] Sundararaghavan V, Zabaras N,Design of microstructure-sensitive properties in elasto-viscoplastic polycrystals using multi-scale homogenization, International Journal of Plasticity, 22 (2006), pp. 1799–1824.

[68] Acharjee S, Zabaras N, A non-intrusive stochastic Galerkin approach for modeling uncertainty propagation in deformation processes, Computers and Structures, 85 (2007), Issues 5-6, pp. 244–254.

[69] Kouchmeshky B, Zabaras N, The effect of multiple sources of uncertainty on the convex hull of material properties, Computational Materials Science, submitted.

[70] Ganapathysubramanian B, Zabaras N, Modeling multiscale diffusion processes in random heterogeneous media, Computer Methods in Applied Mechanics and Engineering, 197 (2008), pp. 3560–3573.

[71] Venturi D, Wan X, Karniadakis G M, Stochastic low-dimensional modeling of a random laminar wake past a circular cylinder, J. Fluid Mech. 606 (2008), pp. 339–367.

[72] Zabaras N, Srikanth A, An Object-oriented Programming Approach to the Lagrangian FEM Analysis of Large Inelastic Deformations and Metal-Forming Processes. Int. J. Numer. Meth. Engng. 45 (1999), pp. 399-445.

[73] Zabaras N, Bao Y, Srikanth A, Frazier W, A continuum Lagrngian sensitivity analysis for metal forming processes with applications to die design problems, Int. J. Numer. Meth, Engng 48(2000), pp. 679-720.

[74] Srikanth A, Zabaras N, An updated Lagrangian finite element sensitivity analysis of large deformations using quadrilateral elements. International Journal for Numerical Methods in Engineering, 52(2001), pp. 1131-1163.

[75] Cameron R, Martin W, The orthogonal development of nonlinear functionals in series of Fourier-Hermite functionals, Ann. Math., 48(1947),pp. 385–392.